TWO DIMENSIONAL BUBBLES AND DROPS IN A YIELD STRESS FLUID

by

JOHN P. SINGH

A dissertation submitted to the Graduate Faculty in Chemical Engineering in partial fulfillment of the requirements for the degree of Doctor of Philosophy, The City University of New York

2007

UMI Number: 3284396

ProQuest Information and Learning Company
300 North Zeeb Road
P.O. Box 1346
Ann Arbor, MI 48106-1346

This manuscript has been read and accepted for the Graduate Faculty in Chemical Engineering in satisfaction of the dissertation requirement for the degree of Doctor of Philosophy.

September 17, 2007	Morton M. Denn
Date	Chair of Examining Committee
September 17, 2007	Mumtaz K. Kassir
Date	Executive Officer

Charles Maldarelli

Gabriel I. Tardos

Jeffrey F. Morris

Mark D. Shattuck

Taehun Lee

Supervisory Committee

THE CITY UNIVERSITY OF NEW YORK

Abstract

TWO DIMENSIONAL BUBBLES AND DROPS IN YIELD STRESS FLUID

by

John P. Singh

Adviser: Professor Morton M. Denn

We have implemented a finite-element code for a two-phase system consisting of incompressible two-dimensional Newtonian bubbles or droplets moving in a continuous Bingham fluid. The code employs a level-set method to track the deformable interface and a continuously differentiable viscosity function for the continuous phase that approaches the discontinuous Bingham model as a regularization parameter goes to zero.

Converged solutions for the slow gravitational rising (falling) of single bubbles (droplets) through a Bingham fluid in a large container show the presence of unyielded “ears” on the equatorial axis adjacent to the bubble (droplet) surface. The container boundaries are beyond the outer yield surface, and the flow is independent of the container length scale.

Collinear bubble or droplet pairs in a gravitational field interact in a way that is qualitatively similar to the interactions in a Newtonian outer fluid. Fore-aft symmetry is broken for two collinearly rising bubbles, with the formation of a cap on the upper bubble and an inverted teardrop shape on the lower, forming a “shade tree” following coalescence. The dynamics of shape development in the Bingham material differ from those for a Newtonian continuum, however. There is an unyielded region that initially extends between the two equatorial planes, and there is a recirculating flow that causes flattening of the trailing edges of bubbles. The trailing bubble evolves to a teardrop shape from an intermediate "peanut" shape. With decreasing Bond number (ratio of gravitational to interfacial stresses) the trailing bubble or droplet develops an unusual cusped "fishtail" shape.

Bubble pairs can rise under conditions where the buoyant force on a single bubble does not exceed the integrated yield stress. A collinear configuration is the most effective in terms of overcoming yield stress and a side-by-side configuration is the least effective, with an off-center configuration intermediate. The calculations also show that the off-centered bubbles tend to align when they rise, increasing the coalescence efficiency in a bubbly fluid.

It is also observed that the evolution of three bubbles, and possibly more, can be understood by considering the interactions between each pair of bubbles.

To

Bani and Dayita

Acknowledgments

I would like to take this opportunity to thank two of the most important women in my life- my mother and my wife. No words can describe the support, encouragement and motivation they have provided me whenever I needed. My father's single minded emphasis on education, righteousness of life and devotion to work laid the foundations on which I stand. I hope that this work will make him proud. I owe in a big way to my brother whose contribution is immense- at least as immense as his punches when we used to fight!

Professor Denn has been a guiding force throughout this work. I really admire his scientific approach to problems, integrity, great work ethics and his patience, especially during my long unproductive periods. It has been a great learning experience working with him and I hope that I can walk on a path that would prove worthy of me being called “Mort‘s student”.

Working with Professor Jeff Morris has been a revelation. He has encouraged me to ask scientific questions and has shown how me to look at different aspects of a problem to gather more insight. Professor Mark Shattuck has been a great influence with his vast knowledge on various subjects and his skill of translating his expertise from one problem to a total different one. Professor Charles Maldarelli instilled in me the love for research. Without their invaluable guidance this work wouldn't have been possible.

I would also like to thank Professor Gabriel Tardos and Professor Taehun Lee for being part of my defense committee and for their suggestions and

improvements to the thesis.

The role of the Levich and Chemical Engineering faculty has been immeasurable. I would really like to thank them for providing me with the facilities and for being available whenever I needed them. A special thanks to Andy, Xu, Mary, Lisa, Junjun and Igor without their support no work would be possible.

I owe a lot to my friends and lab mates who have made my stay at the City College memorable. Thanks so much!

This work was supported by the funding from NSF CREST Center for Mesoscopic Modeling and Simulation.

Contents

List of Figures

Chapter 1

Yield-Stress fluid: a review

1.1 Introduction

Newtonian fluids follow a linear homogenous relationship between stress and strain rate. Many industrially important fluids violate this condition and are called non-Newtonian fluids. One important class of non-Newtonian fluids consists of materials that show a yield stress. These fluids, which are sometimes called viscoplastic, behave as elastic solids below a certain critical stress (called the yield stress) and as fluids above that stress. Common yield stress fluids include toothpaste, gels, paints, fermentation broths, mud suspensions, many food products and cosmetics, and colloidal nuclear waste [GTD$^+$97]. Bird [BDY70], in a review article, lists around forty industrially relevant materials that have been known to show a yield stress. In fact, Reiner [Rei60] states that the yield stress is a fundamental rheological property shown by all materials under different physical conditions. In Reiner's words, "Elasticity, plasticity, viscosity and strength are fundamental rheological properties from which most others can be derived... *every material possesses all rheological properties, although in varying degree.* " (The italics are Reiner's).

It is easiest to understand the concept of yield stress by considering the following experiment: Keep the sample between two parallel plates and apply a shear force to one of the plates, keeping the other plate stationary. For a small enough force, following an initial transient, there will be no discernible motion for a yield stress fluid. Thus, the material behaves like a solid, as, by definition, fluid flows under any (even infinitesimally small) shear force. The stress at which continuous motion is incipient is called the yield stress. Above the yield stress, the relation between stress and strain rate can be very complex, for example a power law relation called a Herschel-Bulkley fluid. In this thesis, we will concentrate only on linear behavior between the stress and strain rate above the yield stress, known as the Bingham model:

$$\begin{aligned} \tau_{xy} &= \tau_y + \eta_p \dot{\gamma}_{xy} \qquad \tau_{xy} > \tau_y \\ \dot{\gamma}_{xy} &= 0 \qquad \text{otherwise} \end{aligned} \tag{1.1}$$

Here, τ_{xy} is the shear stress, τ_y is the yield stress, $\dot{\gamma}_{xy}$ is shearing strain rate and η_p is a constant, commonly known as the "plastic viscosity". (The true viscosity of a Bingham fluid is a function of strain rate. It is infinite at the yield stress and decreases as the strain rate is increased.) Figure 1.1 shows a schematic of a stress-strain rate curve for a Bingham fluid. The slope of line OA is the viscosity of the fluid at the given strain rate, the magnitude OC is the yield stress, and the slope of line CB is η_p. This model was first proposed by E.C. Bingham ([Bin22]). Bingham measured the flowability (he called it fluidity) of suspensions as a function of increasing particle loading and found that at a critical concentration the suspension is unable to flow for a sufficiently small enough stress. He also emphasized the difference between very viscous liquids and soft solids that flow only above a certain yield stress.

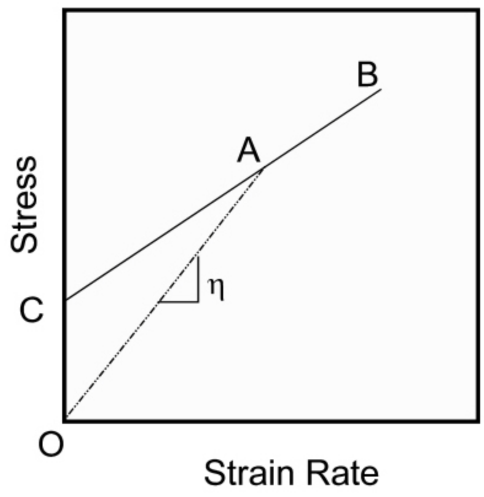

Figure 1.1: Schematic diagram of the Bingham Model

One consequence of the yield stress is that we will not observe any flow if the pressure drop in a pipe is below a critical value . This is in contrast to a viscous fluid, where flow will occur at any pressure drop. If we have a bubble or a drop of another fluid inside a matrix of a yield stress fluid, the bubble or drop might get trapped if the buoyant force is too small to overcome the yield stress because the size is smaller than a critical value. This has very important consequences in mixing.

1.2 Background

The model as given by Bingham (eq. 1.1) is valid for the class of flows where the stress tensor has only one non-zero shear component and all other components are zero. Prager[Pra61] and Oldroyd [Old47b], [Old47a] developed an invariant form of the stress law which can be applied to more general flows:

$$\begin{aligned} \tau &= (\eta_p + \frac{\tau_y}{\sqrt{(\frac{1}{2}\Pi_D)}})\mathbf{D}, & \sqrt{\frac{1}{2}\Pi_y} \geq \tau_y \\ \mathbf{D} &= 0 & \text{otherwise} \end{aligned} \tag{1.2}$$

Here, τ is the stress tensor and $\mathbf{D}$ is the strain rate tensor. $\Pi_y = \tau : \tau$ and $\Pi_D = \mathbf{D} : \mathbf{D}$ are the second invariants of stress and strain rate respectively. The yield criterion based on the second invariant is known as the von Mises criterion. Oldroyd's formulation admitted elastic behavior for stresses below the yield stress. The formulation here assumes that the elastic modulus is infinite.

There are very few analytical solutions of the flow of a Bingham body due to the discontinuous nature of the model. Solutions are known for only very simple geometries like flow in a pipe [BSL98], Couette flow([Rei60]), and an oscillating infinite plate ([AA74]). Lipscomb and Denn proved [LD84] that the lubrication approximation cannot be applied to the Bingham fluid, as the neglected terms in the lubrication analysis are of the order unity. Consequently, one has to consider both shear and elongational components of stress in any complex geometry.

The discontinuous nature of the model makes computation difficult, and models have been devised that are continuous and provide a satisfactory approximation to the Bingham model. See, for example, Wilson [Wil93] for the application of the bi-viscosity model to a lubrication problem and see the work by Frigaard and Nouar [FN05], which compares the convergence of different regularization models. In place of an infinite viscosity at zero stress, the regularization equation defines a large but finite viscosity at stress levels below the yield stress. Mathematically, it makes the Bingham model continuous and, in certain regularization models, differentiable, which can then be implemented in computational models. It has been shown that the regularization technique converges to the Bingham model under a certain limit of regularization parameter ([GLT81]). Some authors (see Barnes and Walters [BW85]and a review article by Barnes [Bar99]) believe that a "sharp" yield stress is only a mathematical artifact that does not exist in practice, although experiments using block copolymers, described by Spaans and Williams [SW95], seem to suggest the existence of a "real" yield stress.

Another technique that has been successfully used in computations to deal with the discontinuity is known as *Domain transformation*; see Beris *et al.* [BTAB85] and Smyrnaios *et al.* [ST01] for details of the technique. Computational techniques have been successfully employed to study the flow behavior of a Bingham body in squeeze flow (Gartling and Tanner [GPT84], Wilson [Wil93], O'Donovan and Tsamopoulos [OT85]), flow around a sphere or a cylinder (Beris *et al.* [BTAB85], Liu *et al.* [LMD03], Mitsoulis [Mit04], Besses *et al* [BMJ03]), and contraction/expansion flow in a pipe or a channel

(Jay *et al* [JMP02], Burgos and Alexandrou [BA99],and Alexandrou and coworkers [AMB01]).

Prager [Pra54] developed variational principles applicable to visco-plastic fluids, and Yoshioka and coworkers, [AY73], [YAI71] obtained the bounds on the drag coefficient in flow of a viscoplastic material around a cylinder and a sphere, respectively. Dubash and Frigaard [DF04] obtained bounds on the critical yield stress for incipient motion of an axi-symmetric bubble in a Herschel-Bulkley fluid. Zwick and co-workers [ZAC96] applied variational principles to squeeze flow of a yield stress material. Huilgol, in a series of papers, developed the variational framework for visco-plastic flow in the presence of slip [Hui98], for unsteady flow (with Nguyen) [HN01] and for flow including inertia [Hui02].

Varnik and coworkers ([VBB04], [VBBB03]) have recently applied molecular dynamics (MD) simulation to study the yield stress transition. They have shown that a (80 : 20) binary mixture of Lennard-Jones fluids shows a yield stress very similar to glassy materials. For the details regarding the Lennard-Jones parameters see Varnik *et al* [VBBB03] and Kob and Anderson [KA95]. Varnik and coworkers observed that below the glass transition temperature, the model exhibits shear banding under shear force. They also measured the yield stress of the model fluid as a function of the temperature below the glass transition.

Yield stress fluids are difficult to handle experimentally, as these materials show slip at the wall and shear banding (see Kalyon [Kal05] for a recent review). Also, visco-plastic materials show ageing effects that have to be accounted for while interpreting the results (see for example, Atapattu *et al* [ACU90], Hariharaputhiran *et al* [HSCC98]). Due to such difficulties, reliable experimental data for visco-plastic fluids is hard to generate.

The focus of this thesis is to study the motion of bubbles and drops in a Bingham fluid computationally. In chapter 2 a finite element-based code is developed to study the flow problem, where a level set method is implemented to track the deformation of bubbles and drops. Chapter 3 uses this computational method to study the motion of a single bubble or a drop in a Bingham fluid. Chapter 4 extends the study to two and three interacting bubbles (or drops). Chapter 5 completes the present work with some conclusions and future directions.

Chapter 2

Methodology: Finite element method and level sets

2.1 Introduction

In this chapter, a computational framework will be developed to study the motion of deformable drops or bubbles in a yield stress fluid. First, the Galerkin finite element method for Newtonian fluids will be described. Then, the framework will be extended to non-Newtonian fluids, especially the Bingham fluid. In the third section, Level Set methods will be introduced and the numerical method to solve the resulting equations will be described.

All fluids follow Cauchy‘s equations of motion, which are as follows:

$$\frac{\partial \rho}{\partial t} + \nabla \cdot \rho \mathbf{u} = 0 \tag{2.1}$$

$$\frac{\partial \rho \mathbf{u}}{\partial t} + \rho \mathbf{u}.\nabla \mathbf{u} - \nabla \cdot \mathbf{\Sigma} = \mathbf{f} \tag{2.2}$$

where $\Sigma = -P + \tau$ is the stress, which is related to gradients of velocity via a constitutive equation; $\mathbf{u}$ is the velocity vector; ρ is the density; and $\mathbf{f}$ is the body force. The first equation is the continuity equation and the second is Cauchy‘s equation of motion.

From the physical parameters involved one can define a dimensionless number called the Reynolds number,

$$Re = \frac{\rho D V}{\eta} \tag{2.3}$$

where ρ is the density, D and V are the characteristic length and velocity, respectively, and η is the viscosity of the fluid. Re is the ratio of the inertial force to the viscous force.

For low Reynolds number ($Re << 1$) flow (*creeping flow*) Cauchy‘s equation of motion can be written as

$$\begin{aligned} \nabla \cdot \mathbf{u} &= 0 \qquad (2.4) \\ \nabla \cdot \tau &= \nabla P - \mathbf{f} \qquad (2.5) \end{aligned}$$

In this thesis the inertial terms will always be neglected and only the creeping flow equations will be used.

2.2 Finite element methods

In the literature, one can find many books on the general subject of finite element methods (FEM). A nice introduction to the methods can be found in Zienkiewicz [Zie77]. For a comprehensive treatment of general procedures involved in FEM see Bathe [Bat95]. The work in this thesis is based on the direct velocity formulation as suggested by Reddy [Red84], [RG94].

The finite element method combines the classical variational approach and methods of weighted residuals. The entire domain over which we want to solve the problem is divided into small sub-domains called elements. The variational, or weak form, of the problem is posed over each element. An approximate solution in terms of appropriate functions $\{\psi_i\}$ and some unknown constants $\{c_i\}$ is then proposed. The parameters $\{c_i\}$ are determined such that the variational problem as posed is satisfied in a weighted-integral sense. As the approximate form is not the exact solution, residuals are generally non-zero. Then, the weighted integrals of the residuals are equated to zero to find the unknown constants and hence the approximate solution. In two dimensions the small elements are typically chosen to be quadrilaterals or triangles, or some combination of both. In three dimensions correspondingly the elements can be tetrahedrons, bricks, or prisms. The *Finite* part of the "Finite Element Method" refers to the fact that the differential equations are reduced to a finite number of algebraic equations. It also refers to the fact that the solution space where we look for the solution is finite dimensional.

In the following section, we further outline the finite element discretization process as applied to the creeping flow equations.

2.2.1 Finite element discretization

Penalty function formulation

Recall that the conservation of mass and momentum for an incompressible creeping flow isothermal problem can be written as

$$\begin{aligned} \nabla \cdot \mathbf{u} &= 0 \\ \nabla P - \nabla \cdot \tau &= \mathbf{f} \end{aligned}$$

where $\mathbf{u}$ is the velocity vector, P is the scalar pressure, τ is the deviatoric stress tensor, and $\mathbf{f}$ is a body force (if any). For an inelastic (generalized Newtonian) fluid, in which the extra stress is proportional to the rate of deformation and the proportionality constant (viscosity) may be rate dependent, the above equations can be written in two dimensions as

Conservation of linear momentum:

$$\begin{aligned} -\frac{\partial}{\partial x}\Big(2\eta\frac{\partial u}{\partial x}\Big) - \frac{\partial}{\partial y}\Big[\eta\Big(\frac{\partial u}{\partial y} + \frac{\partial v}{\partial x}\Big)\Big] + \frac{\partial P}{\partial x} &= f_x \\ -\frac{\partial}{\partial y}\Big(2\eta\frac{\partial v}{\partial y}\Big) - \frac{\partial}{\partial x}\Big[\eta\Big(\frac{\partial u}{\partial y} + \frac{\partial v}{\partial x}\Big)\Big] + \frac{\partial P}{\partial y} &= f_y \end{aligned} \tag{2.6}$$

Conservation of mass:

$$\frac{\partial u}{\partial x} + \frac{\partial v}{\partial y} = 0 \tag{2.7}$$

where u and v are the velocity components in the x and y directions, respectively, P is the pressure, f_x and f_y are the body forces along x and y directions, and η is the viscosity of the fluid. The boundary conditions can be written as

$$t_x \equiv 2\eta\frac{\partial u}{\partial x}n_x + \eta\Big(\frac{\partial u}{\partial y} + \frac{\partial v}{\partial x}\Big)n_y - Pn_x = t_{x0} \tag{2.8}$$

$$t_y \equiv 2\eta\frac{\partial v}{\partial y}n_y + \eta\Big(\frac{\partial u}{\partial y} + \frac{\partial v}{\partial x}\Big)n_x - Pn_y = t_{y0} \tag{2.9}$$

$$u = u_0 \qquad v = v_0 \tag{2.10}$$

where n_x and n_y denote the normal in x and y directions; t_{x0}, t_{y0}, u_0 and v_0 are known functions or constants.

In the above differential equations the solution $(\mathbf{u}, P)$ must satisfy $\mathbf{u} \in C^2$ and $P \in C^1$; i.e. $\mathbf{u}$ and all its first and second derivatives must be continuous and P and its first derivatives must also be continuous. One can obtain a more general solution by converting the equations to weak form.

Essentially, the FEM technique is used to obtain the solution to the weak (or the variational) form of the differential equation. To obtain the weak form over each element Ω^e we multiply each equation by a *test function* and integrate by parts. As there are three unknowns in the problem, $\{u, v, P\}$, three separate test functions or weight functions need to be defined, each corresponding to one variable. Then, using the Green-Gauss theorem we obtain

$$0 = \int_{\Omega^e} \Big[2\eta \frac{\partial w_1}{\partial x}\frac{\partial u}{\partial x} + \eta \frac{\partial w_1}{\partial y}\Big(\frac{\partial u}{\partial y} + \frac{\partial v}{\partial x}\Big) - \frac{\partial w_1}{\partial x} P - w_1 f_x\Big] \mathrm{d}x\mathrm{d}y - \oint_{\Gamma^e} w_1 t_{x0} \mathrm{d}s \tag{2.11}$$

$$0 = \int_{\Omega^e} \Big[2\eta \frac{\partial w_2}{\partial y}\frac{\partial v}{\partial y} + \eta \frac{\partial w_2}{\partial x}\Big(\frac{\partial u}{\partial y} + \frac{\partial v}{\partial x}\Big) - \frac{\partial w_2}{\partial y} P - w_2 f_y\Big] \mathrm{d}x\mathrm{d}y - \oint_{\Gamma^e} w_2 t_{y0} \mathrm{d}s \tag{2.12}$$

$$0 = -\int_{\Omega^e} w_3 \Big(\frac{\partial u}{\partial x} + \frac{\partial v}{\partial y}\Big) \mathrm{d}x\mathrm{d}y \tag{2.13}$$

where w_1,w_2 and w_3 are the appropriate test functions. Γ^e represents the boundary of the element. In the language of methods of variation, $\{w_1, w_2, w_3\}$ are also called variations in $\{u, v, P\}$ respectively. Note that P appears undifferentiated in the momentum equations and there are only first derivatives of u and v. Similarly, the test function w_3 can be a constant and w_1 and w_2 can be bilinear functions of x and y. Also, note that the boundary conditions t_{x0} and t_{y0} appear naturally in the weak form of equations and hence they are called *natural boundary conditions.*

The weak form can be written as

$$B((w_1, w_2, w_3), (u, v, P)) = l(w_1, w_2, w_3) \tag{2.14}$$

where,

$$\begin{aligned}
B(\cdot,\cdot) &= \int_{\Omega^e} \Big[2\eta\Big(\frac{\partial w_1}{\partial x}\frac{\partial u}{\partial x} + \frac{\partial w_2}{\partial x}\frac{\partial v}{\partial x}\Big) + \\
&\quad \eta\Big(\frac{\partial w_1}{\partial y} + \frac{\partial w_2}{\partial x}\Big)\Big(\frac{\partial u}{\partial y} + \frac{\partial v}{\partial x}\Big) + \\
&\quad \Big(\frac{\partial w_1}{\partial x} + \frac{\partial w_2}{\partial y}\Big)P + (\frac{\partial u}{\partial x} + \frac{\partial v}{\partial y})w_3\Big]\mathrm{d}x\mathrm{d}y \qquad (2.15) \\
l(\cdot) &= \int_{\Omega^e}(w_1 f_x + w_2 f_y)\mathrm{d}x\mathrm{d}y - \oint_{\Gamma^e}(w_1 t_{x0} + w_2 t_{y0})\mathrm{d}s \qquad (2.16)
\end{aligned}$$

If we assume that the velocities satisfy the continuity equation identically, then the weight functions w_1 and w_2 are also required to satisfy it. Thus the terms containing P and w_3 drop out of the equation. This makes $B(\mathbf{w},\mathbf{u})$, where $\mathbf{w} = (w_1, w_2)$ and $\mathbf{u} = (u, v)$, a bilinear function and $l(\mathbf{w})$ a linear function. Also, $B(\mathbf{w},\mathbf{u})$ is a symmetric function in terms of $\mathbf{u}$ and $\mathbf{w}$. It is known that whenever the bilinear form is symmetric, the quadratic form associated with the variational problem is obtained in the form (see [Red84] section 2.2)

$$I_0(\mathbf{u}) = \frac{1}{2}B(\mathbf{u},\mathbf{u}) - l(\mathbf{u}) \qquad (2.17)$$

The penalty function method allows us to incorporate the constraint of conservation of mass back into the equation in a least squares sense. Under this approach we view the problem as one of minimizing the functional $I_0(u,v)$ with the constraint of mass conservation,

$$I_p(u,v) = I_0(u,v) + \frac{\lambda_p}{2}\int_{\Omega_e}\Big((\frac{\partial u}{\partial x} + \frac{\partial v}{\partial y})^2\Big)\mathrm{d}x\mathrm{d}y \qquad (2.18)$$

where λ_p is the penalty parameter. The higher the value of penalty parameter, the more strictly the constraint is observed in the solution. The upper bound on λ_p is placed by computational constraints; too high a value will lead to a very large penalty term compared to other terms in the equation, causing a trivial numerical solution. The value of the penalty parameter is recommended to be [Red84]

$$\lambda_p = \eta \times 10^6 \leq 10^{13} \tag{2.19}$$

In this work $\lambda_p = 10^7$, which is within the limit prescribed.

In the current form, our problem (2.18) does not contain the pressure P. Pressure is calculated by the following equation

$$-P = \lambda_p(\frac{\partial u}{\partial x} + \frac{\partial v}{\partial y}) \tag{2.20}$$

where (u, v) is the solution to the minimization problem.

The minimization problem (2.18) is denoted as

$$\delta I_p = 0 \tag{2.21}$$

which gives

$$\begin{aligned} 0 = \int_{\Omega^e} \Big[2\eta \frac{\partial \delta u}{\partial x}\frac{\partial u}{\partial x} + \eta \frac{\partial \delta u}{\partial y}\Big(\frac{\partial u}{\partial y} + \frac{\partial v}{\partial x}\Big) - \delta u f_x\Big]\mathrm{d}x\mathrm{d}y - \oint_{\Gamma^e} \delta u t_{x0} \mathrm{d}s \\ + \int_{\Omega^e} \lambda_p \frac{\partial \delta u}{\partial x}\Big(\frac{\partial u}{\partial x} + \frac{\partial v}{\partial y}\Big)\mathrm{d}x\mathrm{d}y \end{aligned} \tag{2.22}$$

and,

$$\begin{aligned} 0 = \int_{\Omega^e} \Big[2\eta \frac{\partial \delta v}{\partial y}\frac{\partial v}{\partial y} + \eta \frac{\partial \delta v}{\partial x}\Big(\frac{\partial u}{\partial y} + \frac{\partial v}{\partial x}\Big) - \delta v f_y\Big]\mathrm{d}x\mathrm{d}y - \oint_{\Gamma^e} \delta v t_{y0} \mathrm{d}s \\ + \int_{\Omega^e} \lambda_p \frac{\partial \delta v}{\partial y}\Big(\frac{\partial u}{\partial x} + \frac{\partial v}{\partial y}\Big)\mathrm{d}x\mathrm{d}y \end{aligned} \tag{2.23}$$

To obtain the above form the viscosity has been assumed to be a constant. This is the weak form of the variational problem with $\delta u = w_1$ and $\delta v = w_2$. This pair of equations is solved over each element in the space to get the velocities, and then the pressure via Equation 2.20.

Implementation Issues

Generally, elements of different shapes and sizes are distributed throughout the computational domain. In this work, only quadrilaterals are used. It is convenient to define the problem in terms of a *"master element"* which has the origin at its centroid and its natural coordinates $(\hat{\xi}, \hat{\eta})$ satisfy $\hat{\xi} \in [-1, 1]$ and $\hat{\eta} \in [-1, 1]$ (Figure 2.1). We can transform the coordinates from the global coordinate system (x, y) to the natural coordinates of the element $(\hat{\xi}, \hat{\eta})$ via

$$x = \sum_{i=1}^{n} x_i \psi_i(\hat{\xi}, \hat{\eta}); \qquad y = \sum_{i=1}^{n} y_i \psi_i(\hat{\xi}, \hat{\eta}) \tag{2.24}$$

where $n = 9$ for the nine-node element. (x_i, y_i) are the coordinates of the nodes in the element (see Figure 2.2). In this work we chose nine-node isoparametric quadrilateral elements for the velocities u, v and four node quadrilaterals for the penalty term (Figure 2.1). The term *isoparametric element* means that the order of interpolation or approximation to the primary variables is the same as the coordinates, i.e.

$$u = \sum_{i=1}^{n} u_i \psi_i; \qquad v = \sum_{i=1}^{n} v_i \psi_i \tag{2.25}$$

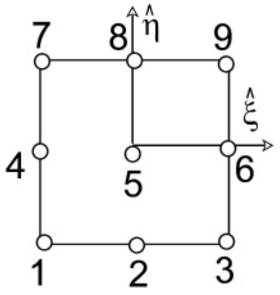

Figure 2.1: Local coordinate system of a master element

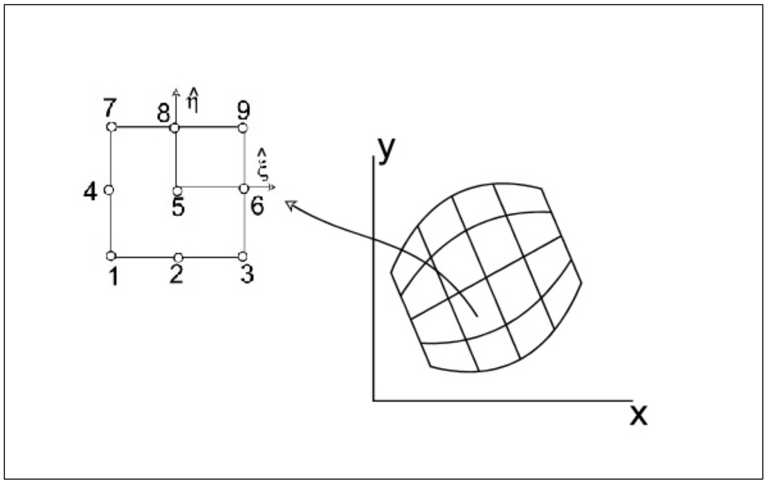

Figure 2.2: Transformation from global coordinates to local coordinates.

Substituting (2.25) in (2.23), we obtain the following matrix equation:

$$\begin{bmatrix} [\bar{K^{11}}] & [\bar{K^{12}}] \\ \left[\bar{K^{12}}\right]^T & [\bar{K^{22}}] \end{bmatrix} \begin{Bmatrix} \{u\} \\ \{v\} \end{Bmatrix} = \begin{Bmatrix} \{F^1\} \\ \{F^2\} \end{Bmatrix} \tag{2.26}$$

where

$$[\bar{K^{ij}}] = [K^{ij}] + \lambda_p [S^{ij}] \tag{2.27}$$

K^{ij} and S^{ij} are the element matrices, defined as

$$\begin{aligned} [K^{11}] &= 2\eta[S^{11}] + \eta[S^{22}] \\ \left[K^{12}\right] &= \eta[S^{12}]^T \\ \left[K^{22}\right] &= \eta[S^{11}] + 2\eta[S^{22}] \\ S^{11}_{ij} &= \int_{\Omega^e} \frac{\partial\psi_i}{\partial x}\frac{\partial\psi_j}{\partial x}\mathrm{d}x\mathrm{d}y \\ S^{12}_{ij} &= \int_{\Omega^e} \frac{\partial\psi_i}{\partial x}\frac{\partial\psi_j}{\partial y}\mathrm{d}x\mathrm{d}y \\ S^{22}_{ij} &= \int_{\Omega^e} \frac{\partial\psi_i}{\partial y}\frac{\partial\psi_j}{\partial y}\mathrm{d}x\mathrm{d}y \\ F^1_i &= \int_{\Omega^e} f_x\psi_i\mathrm{d}x\mathrm{d}y + \oint_{\Omega^e} t_x\psi_i\mathrm{d}s \\ F^2_i &= \int_{\Omega^e} f_y\psi_i\mathrm{d}x\mathrm{d}y + \oint_{\Omega^e} t_y\psi_i\mathrm{d}s \end{aligned} \tag{2.28}$$

These integrals can be transformed to integrals over each element in its natural coordinates using the transformation 2.24. All the resulting integrals have limits $(\hat{\xi}, \hat{\eta}) \rightarrow ([-1,1],[-1,1])$ and are easily handled using Newton-Cotes or Gauss-Legendre quadrature formulas [Poz98]. We used four-sided isoparametric elements with nine nodes and the corresponding Gauss-Legendre quadratures. The details of implementation of the quadrature on the four-sided nine-node elements can be found in any book on numerical methods (eg. see Reddy [Red84], Bathe [Bat95] or Pozrikidis [Poz98]). Here we just list the Gauss sampling points and quadrature weights for rectangular elements in Table 2.1 and the interpolation functions 2.29 for the nine point element.

The resulting linear equation 2.26 for each element can be combined to form an overall linear equation for the entire computational domain. The resulting matrix equation can be solved using standard linear algebra techniques such as Gauss Elimination or the Conjugate Gradient method, among others. In this work, an open source code called MUMPS was used to solve the linear matrix equation. MUMPS is a linear equation solver in a parallel environment; more information regarding the package can be found in the user guide [mum].

$$
\begin{aligned}
\hat{\phi}_1 &= 1/4(1-\hat{\xi})(1-\hat{\eta})\hat{\xi}\hat{\eta} \\
\hat{\phi}_2 &= -1/2(1-\hat{\xi}^2)(1-\hat{\eta}^2)\hat{\eta} \\
\hat{\phi}_3 &= -1/4(1+\hat{\xi})(1-\hat{\eta})\hat{\xi}\hat{\eta} \\
\hat{\phi}_4 &= -1/2(1-\hat{\xi})(1-\hat{\eta}^2)\hat{\xi} \\
\hat{\phi}_5 &= (1-\hat{\xi}^2)(1-\hat{\eta}^2) \qquad (2.29) \\
\hat{\phi}_6 &= 1/2(1+\hat{\xi})(1-\hat{\eta}^2)\hat{\xi} \\
\hat{\phi}_7 &= -1/4(1-\hat{\xi})(1+\hat{\eta})\hat{\xi}\hat{\eta} \\
\hat{\phi}_8 &= 1/2(1-\hat{\xi}^2)(1+\hat{\eta})\hat{\eta} \\
\hat{\phi}_9 &= 1/4(1+\hat{\xi})(1+\hat{\eta})\hat{\xi}\hat{\eta}
\end{aligned}
$$

$\hat{\xi}$	$\hat{\eta}$	weight$_i$	weight$_j$
-0.774	0.774	0.5555	0.5555
-0.774	0.0	0.5555	0.8889
-0.774	-0.774	0.5555	0.5555
0.0	0.774	0.8889	0.5555
0.0	0.0	0.8889	0.8889
0.0	-0.774	0.8889	0.5555
0.774	0.774	0.5555	0.5555
0.774	0.0	0.5555	0.8889
0.774	-0.774	0.5555	0.5555

Table 2.1: The weights at various Gauss sample points.

2.2.2 Finite Element for Non-Newtonian constitutive law

Very little changes in the above formulation for non-Newtonian fluids. The only difference is that the stiffness matrix is now a function of local viscosity. The stiffness matrix of each element is formed using a local viscosity and then the elements are assembled in the usual way to form the global stiffness matrix. The rest of the formulation remains the same.

2.3 Free surface boundary conditions

Problems involving free surfaces are very interesting as well as challenging. The interest comes from the fact that the problems are generally very important in industrial applications and also are very rich in the physical behavior they exhibit. The challenging part refers to the fact that the free surface is deformable and its shape is a part of the solution. At the free surface we need to satisfy the following boundary conditions:

$$\mathbf{u} = \hat{\mathbf{u}} \tag{2.30}$$

$$\tau_s = \hat{\tau}_s \tag{2.31}$$

$$\hat{P} - P + (\tau_n - \hat{\tau}_n) \cdot n = \sigma \nabla \cdot \mathbf{n} \tag{2.32}$$

The first equation states that velocities need to be continuous across the interface. The second one refers to the fact that the shear stress is continuous across the interface; i.e. the interface itself cannot sustain any shear stress. The third equation says that there is a jump in the normal stress when going from one phase to the other that is determined by the surface tension (σ) and the curvature of the interface. This equation assumes that the surface tension is constant along the interface and that there are no Marangoni stresses. For a nice review of these equations see Leal [Lea92].

2.3.1 Level set method

The essential problem in following bubble dynamics in any suspending fluid is to compute the shape of the interface, which is unknown *a priori*. A variety of interface tracking schemes have been developed (see, for example, the review by Scardovelli and Zaleski [SZ99]). A finite-element formalism and higher-order iterative methods for locating the free surface are discussed in the tutorial chapter by Kistler and Scriven [KS83]. In this work, we implement Level-Set methods introduced by Osher and Sethian [OS88]. Level set methods have been successfully used by a number of authors to study both compressible [MOS92] and incompressible flow problems [SSO94]. Pillaipakkam and Singh [PS01] successfully implemented the method to study the bubble dynamics in a viscoelastic fluid. For a review of the method see the book by Sethian [Set96] or the review papers by Osher [OF63] and Sethian [SS03]. These reviews also describe the application of the level-set methods to areas as diverse as semiconductor processing, imaging of geophysical data, kinetic crystal growth computer vision and image processing.

A level set is typically a smooth, Lipschitz continuous function, denoted by ϕ, which evolves as the interface changes. One particular value of ϕ, say $\phi(\mathbf{x}, t) = 0$, represents the interface at all times. The level set method is an Eulerian approach with no explicit tracking of the interface involved, making it easier to implement and extend to higher dimensions.

Suppose we have a surface $\Gamma(t = 0)$, propagating along its normal with speed that depends on curvature and other parameters. Define a level set function $\phi(x, t = 0) = \pm d$, where d is the normal distance of a point x from the surface Γ. ϕ is taken to be positive in one phase and negative in the other, with a zero value denoting the interface. If $\phi(\mathbf{x}, t) = 0 = \Gamma(t)$, then by differentiating we obtain

$$\phi_t + \nabla\phi \cdot \frac{\partial \mathbf{x}}{\partial t} = 0 \tag{2.33}$$

If **u** is the velocity of the front then we have

$$\phi_t + \mathbf{u}.\nabla\phi = 0 \tag{2.34}$$

which is the required level set equation.

Geometric properties of the interface can also be determined using the level set function, ϕ. For example, the normal vector to the surface is

$$\mathbf{n} = \frac{\nabla\phi}{|\nabla\phi|} \tag{2.35}$$

and curvature is given by

$$\kappa = \nabla \cdot \frac{\nabla\phi}{|\nabla\phi|} = \frac{\phi_{xx}\phi_y^2 - 2\phi_x\phi_y\phi_{xy} + \phi_{yy}\phi_x^2}{(\phi_x^2 + \phi y^2)^{3/2}} \tag{2.36}$$

Implementation

Tabata and Fujima [TF91] developed a third order upwind method to solve the hyperbolic convection equation on a finite element grid. Their method has been successfully implemented by Pillaipakkam and Singh [PS01] to track a deformable bubble in a viscoelastic fluid.

A summary of this method can be found in Glowinski and Pironneau [GP67]. The equation we are interested in solving is

$$\phi_t + \mathbf{u} \cdot \nabla\phi = 0 \tag{2.37}$$

The method is based on the fact that the term $\mathbf{u} \cdot \nabla\phi(x)$ at a given node $\mathbf{O}$ is just the projection of the gradient of ϕ on to the velocity vector $\mathbf{u}(\mathbf{O})$. Denoting the unit vector $\mathbf{u}(\mathbf{O})/|\mathbf{u}(\mathbf{O})|$ by ξ, we can write

$$\mathbf{u} \cdot \nabla\phi(x)(\mathbf{O}) = |\mathbf{u}(\mathbf{O})|\partial\phi/\partial\xi(\mathbf{O}) \tag{2.38}$$

Now, choose two points $\{\mathbf{B}, \mathbf{D}\}$ downstream of $\mathbf{O}$ and two points $\{\mathbf{W}, \mathbf{U}\}$ upstream of $\mathbf{O}$ on the ξ-axis, where U and D are the points nearest to O (see Figure 2.3). Denote by $\mathbf{P}$ the set $\{\mathbf{W}, \mathbf{U}, \mathbf{O}, \mathbf{D}, \mathbf{B}\}$ Take $h = \mathit{length}(\mathbf{O}, \mathbf{U})$ as the characteristic element length around $\mathbf{O}$. Define $\xi'_P = \xi_P/h$ as the ξ-coordinates of $\mathbf{P}$. This gives $\xi'_O = 0, \xi'_U = -1$. The approximation to the convection term can then be written as

$$(\mathbf{u}.\nabla\phi)(\mathbf{O}) = |\mathbf{u}(\mathbf{O})| \sum_{P \in \{\mathbf{W},\mathbf{U},\mathbf{O},\mathbf{D},\mathbf{B}\}} \gamma_{\mathrm{P}}\phi(P)/h \tag{2.39}$$

where

$$\begin{aligned} \gamma_{\mathrm{P}} &= \frac{\left(\prod_{Q \notin P,O}(\xi'_O - \xi'_Q) + \beta\right)}{\prod_{Q \notin P}(\xi'_p - \xi'_Q)}, \qquad \mathbf{P} \neq \mathbf{O} & (2.40) \\ \gamma_{\mathrm{O}} &= -\sum_{Q \notin O} \gamma_{\mathrm{Q}} & (2.41) \end{aligned}$$

and β is a non-negative parameter, which usually takes values between 3 and 6. Tabata and Fujima have shown that when $\beta = 0$, equation 2.39 is the fourth-order central approximation; if $\beta > 0$ then the approximation is upwinded. Figure 2.3 shows the typical choice of the upstream and downstream points in a triangular mesh.

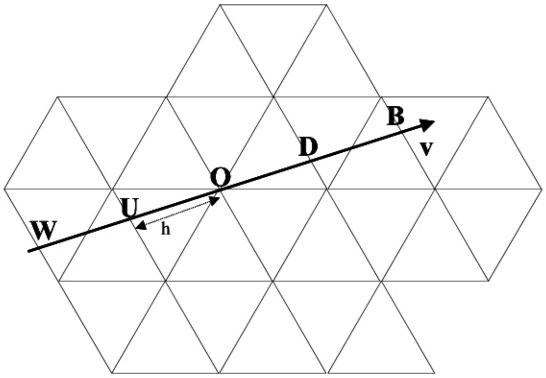

Figure 2.3: Schematic illustrating the third order upwinded method. Based on the work of Tabata and Fujima (1992).

Re-initialization

We initialize the level set function to be a signed distance function from the interface. When it is convected, it may no longer remain a signed distance function. This is highly undesirable as it can lead to loss of mass [SSO94]. This loss is attributed to steep gradients of ϕ near the interface causing inaccurate calculation of curvature. Thus, it is highly desirable to maintain $|\nabla\phi| = 1$. Also, a gradient of magnitude unity is required to provide a fixed width to the interface with time.

Sussman and his coworkers [SSO94] have devised a solution to this problem. They consider a given function $\phi_0(\mathbf{x})$, which might not be a distance function. Then they construct an equation which on solving to steady state gives a function $\phi(\mathbf{x})$ that will have the same zero level set as $\phi_0(\mathbf{x})$ and also have $|\nabla\phi| = 1$. This they achieve by solving the equation

$$\phi_t = S(\phi_0)(1 - \sqrt{\phi_x^2 + \phi_y^2}), \qquad \phi(\mathbf{x}, 0) = \phi_0(\mathbf{x}) \tag{2.42}$$

where S is the Signum function i.e. S equals 1 when ϕ_0 is positive and -1 for negative ϕ_0. For the purpose of numerical calculations the Signum function was approximated as

$$S(\phi_0) = \frac{\phi_0}{\sqrt{\phi_0^2 + \alpha^2}} \tag{2.43}$$

where α is a small parameter taken to be 1.5 times the size of mesh around the interface.

Thus, we solve the re-initialization equation 2.42 after each time step to make $|\nabla\phi| = 1$. Only one iteration per time step was required to get a converged solution in our calculations.

2.4 Summary

In this chapter we have developed a computational framework to study the motion of deformable bubbles in a non-Newtonian fluid. This framework involves solving the creeping flow equations (2.6) using the Bingham model for the stress, along with level set equations (2.34,2.42). Figure 2.4 depicts a simplified algorithm for the numerical technique developed.

In the remaining chapters we will apply the method developed to study the motion of a single bubble or a drop in a yield stress fluid (chapter 3) and then extend the study to interacting bubbles (or drops) in chapter 4.

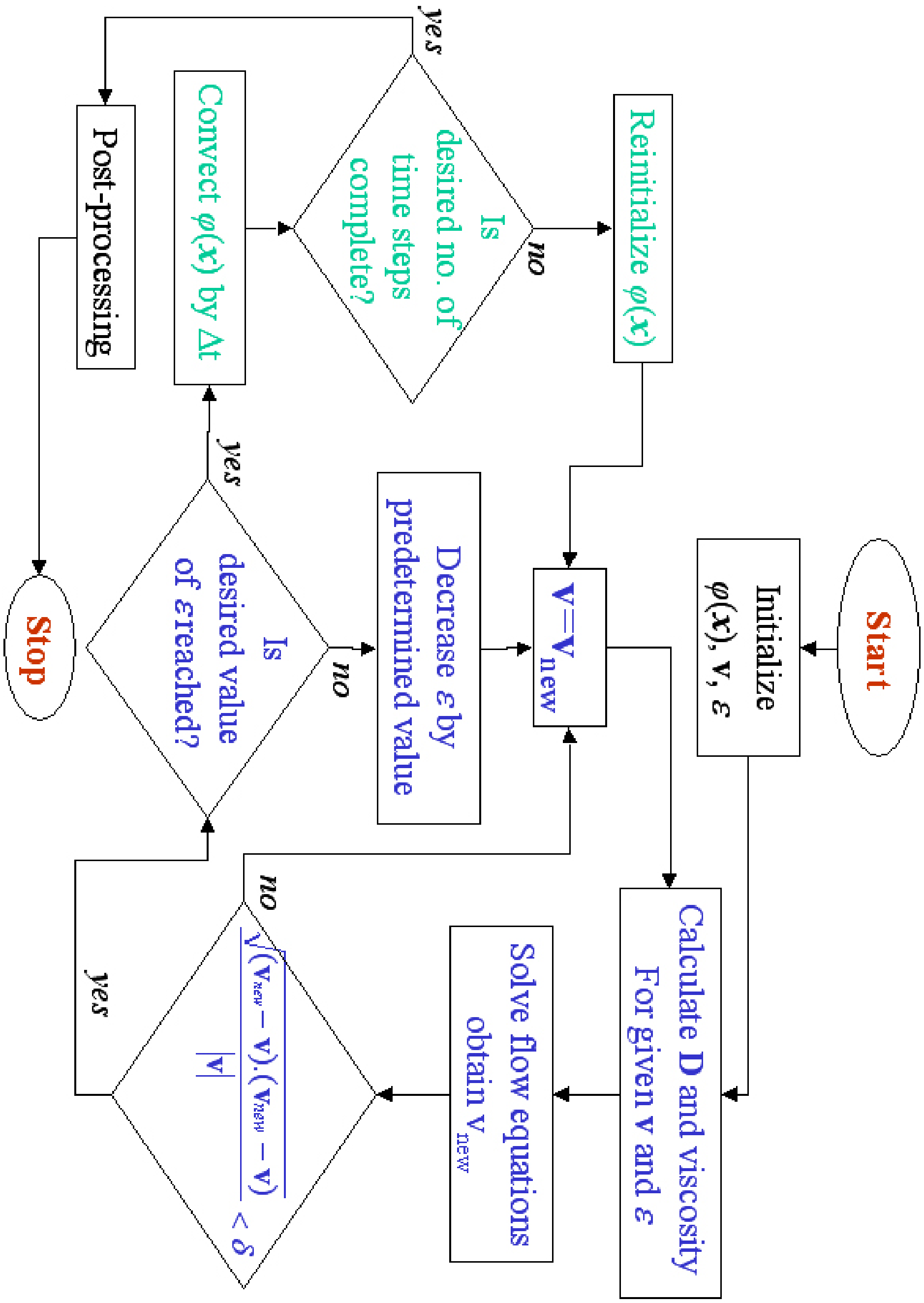

Figure 2.4: Simplified algorithm for the computational technique implemented.

Chapter 3

Single bubble or drop

3.1 Introduction

Many liquid-like materials exhibit a yield stress. Above a critical stress these materials flow, but below this stress they only deform as elastic bodies. Yield-stress materials, also called visco-plastic materials, are often colloidal suspensions. Some of the commonly experienced viscoplastic materials in consumer products are paints, mayonnaise, toothpaste, ketchup, etc. The waste sludge tanks at the U.S Department of Energy's Hanford site contain radioactive colloidal suspensions that exhibit a yield stress [GTD$^+$97]; the motion of flammable bubbles in these materials is a matter of particular concern. For a review of materials which show yield behavior, see Bird [BDY70]. Another comprehensive review of such materials is due to Barnes [Bar99].

The solution of complex flow problems for yield-stress materials is challenging because of the possible existence of yielded regions in which flow can occur and unyielded regions in which only elastic deformation is possible. The interface between these regions, called the yield surface, is not known *a priori* and its location is part of the solution.

The rise (or fall) of a single bubble (or a drop) is the topic of study in this chapter. The computational tools developed in the preceding chapter will be implemented to study the problem. The next section reviews the previous work on flow of viscoplastic fluid around an object. Then the problem of a rising bubble (or falling droplet) is formulated, followed by results and some conclusions.

3.2 Previous work on flow of a viscoplastic fluid around an object

Flow of a yield stress fluid around a solid sphere or a cylinder has been studied by various authors. Ansley and Smith [AS67] are among the earliest known to study the problem of a solid sphere falling through a yield stress fluid. They conducted experiments by dropping solid balls in tomato sauce under conditions of relatively high Reynolds number ($2 - 130$). They also conducted a “stress analysis” to obtain the non-dimensional parameter describing the settling laminar regime. Their work has been followed by a number of experiments by different groups. For an extensive review see the book by Chhabra [Chh93]. Tabuteau *et al* [TCdB07] and Merkaka *et al* [MJM06] describe some recent experimental results and contain a brief review of the subject. Hariharapurithan *et al* [HSCC98], Horsley *at al* [HHWJ04] and Atapattu *et al* [ACU95] also report the effect on drag with shear history of the fluid. In particular, they show that the drag coefficient on a falling sphere depends on the number of spheres dropped. Atapattu and coworkers [ACU90] quantified the wall effects on the fall velocity of a solid sphere. Jossic and Magnin [JM01] report drag on various shaped objects in a yield stress fluid. They also report a difference in drag experienced by a smooth and a rough object, suggesting possible slip on the smooth objects.

In addition to experiments, there have been a number of studies using computational and theoretical tools. Yoshioka and coworkers found the bounds on the drag coefficient using variational principles for flow around a sphere [YAI71]. Adachi and Yoshioka [AY73] then extended the work to find the bounds on flow around a cylinder. Beris *et al* [BTAB85] calculated the shape of the yield surface and the relation between drag coefficient and Bingham number using a finite element code. Liu *et al* [LMD02], [LMD03] studied the effect of the regularization parameter on the yield surface for the case of single and two interacting spheres. Besses *et al* [BMJ03] and Mitsoulis [Mit04] calculated the flow field around an infinite cylinder. Mitsoulis [Mit04] also compared the solution for a solid cylinder to the corresponding solution of flow around a solid cylinder with complete slip on the cylinder surface, as might be the case for smooth objects [Refer to the experimental evidence of slip in [MJM06], [JM01], and [Kal05]] . Zisis and Mistoulis [ZM02] have reported the numerical solution of pressure driven flow around a solid cylinder. Beaulne and Mitsoulis [BM97a] reported the solution of flow around a sphere in tubes filled with a Herschel-Bulkley fluid. Blackery and Mitsoulis [BM97b] also reported the solution of flow around a sphere in a Bingham fluid.

There have been fewer studies of flow of viscoplastic fluid around deformable surfaces. The problem is complicated by the presence of the deformable interface of the drops, which needs to be tracked and is part of the solution. One of the earliest attempts to address the problem was by Bhavaraju and coworkers [BMB78], who did a perturbation analysis of the Hadamard solution for Stokes flow around a bubble under the assumption of small Bingham numbers. Stein and Buggisch [SB00] studied the rise of bubbles under oscillating external pressure experimentally and theoretically. They considered the case when the bubble motion was due to the external pressure. Li and Renardy [LR00] used a Volume of Fluid method to track the shape and break-up of a Newtonian bubble in shear flow of a Bingham fluid under conditions where the Bingham fluid is completely yielded. Potapov and coworkers [PSLN06] studied the motion of single liquid drops and pairs of drops in a Bingham fluid using the Volume of Fluid method in the commercial FLUENT 6.1 code. Dubash and Frigaard [DF04] used variational principles to estimate the conditions under which a bubble will rise.

A systematic study of the problem of a rising bubble in a yield stress fluid has been lacking. This chapter aims to fill in this gap in the literature using the computational tools developed in the preceding chapter.

3.2.1 Two-dimensional flow around objects and the Stokes paradox

It is well known that a solution that satisfies all the boundary conditions for Stokes flow of a Newtonian fluid around a cylinder in an infinite domain does not exist [Bat67], [Lea92]. The paradox can be explained by noting that the velocity field as obtained from the flow equations in two-dimensions behaves as $\ln(r) + 1/r^2$; thus the Reynolds number, $R_e = \frac{\rho U R}{\eta}$, increases with r and becomes of order unity at some large but finite distance from the center of the cylinder. This is true for a cylinder of any cross-sectional shape [LL86] or for more than one interacting cylinders ([Jef22]). In the case of a Bingham fluid, it is expected that the yielded region will be finite and no such paradox should be observed. In fact, Tanner [Tan93] has shown analytically that the Stokes solution for a shear thinning power-law fluid exists for flow around a cylinder in an infinite domain, and this result will extend to a Bingham fluid.

3.3 Problem Formulation

A finite element code was developed to study the problem of flow of a Bingham fluid around a drop or a bubble. To track the shape of the bubble with time the level set method was implemented. For details of the method see chapter 2. Here only a summary is presented.

Following Sussman *et al* [SSO94] and Chang *et al* [CHMO96] the flow equations can be written as

$$\begin{aligned}
\nabla \cdot \mathbf{u} &= 0 && (3.1)\\
\nabla \cdot \tau(\phi) &= \nabla P + \mathbf{F}(\mathbf{x}) + \sigma\kappa(\delta(\phi))\mathbf{n} && (3.2)\\
\frac{\partial \phi}{\partial t} &= -(\mathbf{u} \cdot \nabla)\phi && (3.3)\\
\phi_t &= S(\phi_0)(1 - \sqrt{(\phi_x)^2 + (\phi_y)^2} && (3.4)
\end{aligned}$$

Here $\mathbf{u}$ is the fluid velocity, $\rho(\mathbf{x})$ is the density, $\mathbf{F}$ is the body force and σ is the interfacial tension. δ is the dirac delta function, and $\phi(\mathbf{x})$ denotes the normal distance of a point $\mathbf{x}$ from the interface; $\phi(\mathbf{x})$ equals zero on the interface, is negative inside the bubble or drop and positive outside. $\mathbf{n}$ is the outward normal of the interface. κ denotes the curvature and is given by

$$\kappa(\phi) = \nabla \cdot \frac{\nabla\phi}{|\phi|} \qquad (3.5)$$

Equation 3.1 is the continuity equation and 3.2 is the equation of motion. The level set equation 3.3 is solved coupled with the equation of motion and is used to track the deformable bubble. The fourth equation 3.4 re-normalizes the level set function after each time step. Note that the time t in equation 3.4 is only a pseudo time and the “real time” only appears in equation 3.3. The equations have been modified to include the surface tension rather than treating surface tension via a boundary condition. Chang and coworkers [CHMO96] show that this formulation is equivalent to the formulation when surface tension is considered via a stress balance on the interface.

Among other applications, such a scheme has been successfully used to simulate two phase flow [SSO94], interaction between two bubbles of different densities[CHMO96], and flow of a viscoelastic fluid around a bubble [PS01].

The usual computational approach is to employ a regularized Bingham model as the constitutive equation for τ in the bulk fluid (eq. 3.6). The model approaches the exact Bingham model in the limit as the regularization parameter goes to zero. The regularization approach is discussed in detail by Frigaard and Nouar [FN05]. The fluid inside the bubble or drop is taken to be Newtonian ($\tau = \eta_b \mathbf{D}$, where η_b is a constant viscosity):

$$\tau = \begin{cases} \{\eta_p + \frac{\tau_y}{\sqrt{(\dot{\gamma}^2+\epsilon^2)}}\}\mathbf{D} & \text{if } \phi < 0 \\ \eta_b \mathbf{D} & \text{if } \phi > 0 \end{cases} \tag{3.6}$$

Here τ_y is the yield stress, η_p is the plastic viscosity, $\mathbf{D}$ is rate of strain tensor, and ϵ is the regularization parameter. As $\epsilon \rightarrow 0$ the model approaches the exact Bingham model.

A Galerkin weighted residual integral method was used as the numerical approximation in the coordinate system fixed in the laboratory frame of reference. The whole domain is discretized using nine-node quadrilateral elements. The components of velocities are approximated using Lagrangian biquadratic polynomials. Pressure is approximated as $P = -\lambda \nabla \cdot \mathbf{u}$ [Refer [Red84], [BE80],[BTAB85] for details on the method and the issue of dealing with non-Newtonian behavior].

The resulting integrals in the Galerkin formulation are evaluated using 9-point Gaussian quadrature, except the term containing λ, which was integrated using 4-point quadrature.

The level set equation 3.3 is a convection equation, which is used to convect the interface with the local velocities. The discretization of the convective term in Equation 3.3 is a third order up-winding scheme, as suggested by Tabata and Fujima [TF91]. A summary of this method can be found in Glowinski and Pironneau [GP67]. It is based on the fact that the term $\mathbf{u} \cdot \nabla\phi(x)$ at a given node $\mathbf{O}$ is just the projection of the gradient on to the velocity vector $\mathbf{u}(\mathbf{O})$.

As we convect the level set function with the local velocity, it no longer remains a signed distance function from the interface. Thus, after each time step the level set is re-initialized to be a distance function. The thickness of the interface is defined by the $\phi(\mathbf{x})$ and the uniformity of this thickness is ensured by re-initializing it after each time step using Equation 3.4.

For the purpose of simulations the Signum function ($S(\phi_0)$)is smoothed as follows

$$S(\phi_0) = \frac{\phi_0}{\sqrt{({\phi_0}^2 + \alpha^2)}} \tag{3.7}$$

where α is a small number of the order of the mesh size around the interface. In our calculations α was chosen to be $1.5 \times h$, where h is the mesh size. A few iterations of the re-initialization equation (Eq. 3.4) at each time step suffice to achieve convergence.

The physical properties ($\eta(\mathbf{x})$ and $\rho(\mathbf{x})$) are discontinuous at the interface of the two fluids. This discontinuity is removed by smoothening the physical properties.

$$\eta(\phi) = \begin{cases} \eta_d & \text{if } \phi < -\alpha \\ \eta_b & \text{if } \phi > \alpha \\ \eta_d + (\eta_b - \eta_d)\frac{\phi+\alpha}{2\alpha} & \text{if -}\alpha < \phi < \alpha \end{cases} \tag{3.8}$$

$$\rho(\phi) = \begin{cases} \rho_d & \text{if } \phi < -\alpha \\ \rho_b & \text{if } \phi > \alpha \\ (1/2)\rho_d\{(1 + \frac{\rho_b}{\rho_d}) + (1 - \frac{\rho_b}{\rho_d})\sin(\pi\phi/(2\alpha))\} & \text{if } -\alpha \leq \phi \leq \alpha \end{cases} \tag{3.9}$$

where the subscript d denotes the property in a drop or a bubble and subscript b denotes the property in the bulk fluid, which is Bingham in nature; α is the same as in Eq. 3.7.

The algorithm can be summarized as follows:

Step 1 Pick a value of the regularization parameter ϵ. Initialize the level set function $\phi(\mathbf{x})$ and velocity field $\mathbf{V}$.

Step 2 Calculate the strain rate ($\mathbf{D}$), viscosity (η) and stress field (τ) based on the velocity.

Step 3 For the given ϕ and τ field, solve the equation of motion along with the continuity equation to get the new velocity field.

Step 4 Check the convergence of the velocity field. If the convergence criterion for velocity was not met then go to step 2 with the newly obtained velocity field. If divergence is observed then increase ϵ.

Step 5 If the desired value of the regularization parameter ϵ is not reached then decrease it by a predetermined factor and go to step 2.

Step 6 Once the converged solution is obtained, then convect the ϕ field according to the level set equation.

Step 7 Re-initialize the level set function.

Step 8 Go to step 2 until the desired time steps have been executed.

The input parameters are the viscosity ratio $\eta_r = \eta_p/\eta_b$, the density ratio $\rho_r = \rho_d/\rho_b$, the surface tension σ, and the yield stress of the Bingham fluid τ_y. The plastic viscosity was taken to be $\eta_p = 1$ and the density of the bulk fluid was also taken to be $\rho_d = 1$. The solution of the equations above give the rising (or falling) velocity ($\mathbf{V}$) of the bubble (or drop), with which we can calculate the Bingham number, $Bn = \tau_y R/(\eta_p \mathbf{V})$. We can also define a dimensionless yield stress $Y_g = \frac{\tau_y}{(\Delta\rho g)R}$, a drag coefficient $C_s = \pi\frac{(\Delta\rho g)R}{\eta_p V/R}$ and a Bond number $Bo = \frac{\Delta\rho g R^2}{\sigma}$ or Capillary number $Ca = \frac{\eta_p V}{\sigma}$. The Reynolds number $Re = \frac{\rho R V}{\eta_p}$ is assumed to be very small ($\lll 1$). For $Bn = 1$ and $Y_g = 0.1$, the Reynolds number is computed to be around 10^{-4}.

3.4 Results

An initially un-deformed bubble (or a drop) is kept in the center of a closed, square box (Figure 3.1) and its resulting motion under the influence of gravity is calculated.

The size of the box was taken to be $H = 2$ and the radius of the drop was $R = 0.1$ and $R = 0.05$. A no slip boundary condition was imposed at the walls of the box. At the start of the calculations the regularization parameter

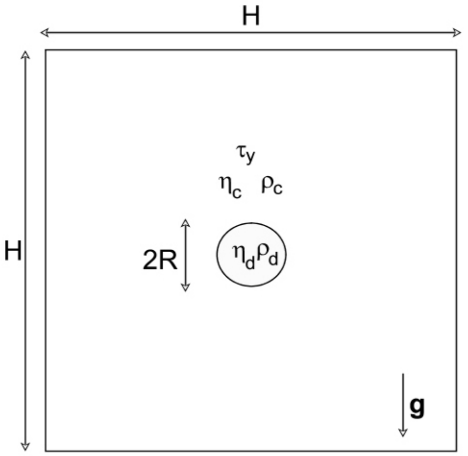

Figure 3.1: Schematic diagram with physical parameters for the case of a drop or a bubble in a Bingham fluid.

(ϵ) is taken to be large enough to give a converged solution. The value of ϵ is decreased slowly, obtaining a converged solution after each reduction in value. The time stepping of the solution is started only when the converged solution is obtained at the required value of ϵ. Based on the results of motion of Bingham fluid around a solid cylinder [BMJ03], it is expected that the region of influence of the bubble will be finite. In other words, the yielded domain will be a finite region around the bubble and regions far enough away will remain un-yielded.

We can categorize all the results in three parts based on the viscosity ratio : bubbles ($\eta_r << 1$), drops ($\eta_r \sim 1$), and very viscous drops ($\eta_r >> 1$).

Figure 3.2 shows the stress contours for a rising bubble. In this figure the ratio of inner to outer fluid density is 0.01, the density difference is 1, and the ratio of inner fluid viscosity to η_p is 0.01. $Bn = \frac{\tau_y R}{\eta_p V} = 1.38$ and $Ca = \frac{\eta_p V}{\sigma} = \infty$. The stress has been normalized by the yield stress, hence the contour level of unity denotes the yield surface. The highest stress levels are present on the poles of the bubbles, and the stress decreases as we move away from the bubble surface on the y-axis until we reach the outer unyielded region. The stress levels are below the yield stress around the equator. As we move away from the bubble along the equator, the stresses increase and then decrease, reaching the yield stress in the far field. The surface plot of the stress field (Figure 3.3) corroborates these conclusions.

The y- and x-directional velocity contours are shown in Figures 3.4 and 3.5 respectively. The surface plot of the magnitude of the velocity is shown in Figure 3.6. The bubble is rising in the y-direction. The velocity is maximum on the poles and monotonically decreases to zero in the far field. On the equator, the velocity is non-monotonic and, almost everywhere, in the negative y-direction. This is a direct consequence of the finite yielded region around the bubble.

Before the results for bubble, drop and very viscous drop are discussed further, it is imperative to check for the convergence of the results. After convergence is established, the effect of physical parameters like interfacial tension, viscosity ratio and yield stress will be explored.

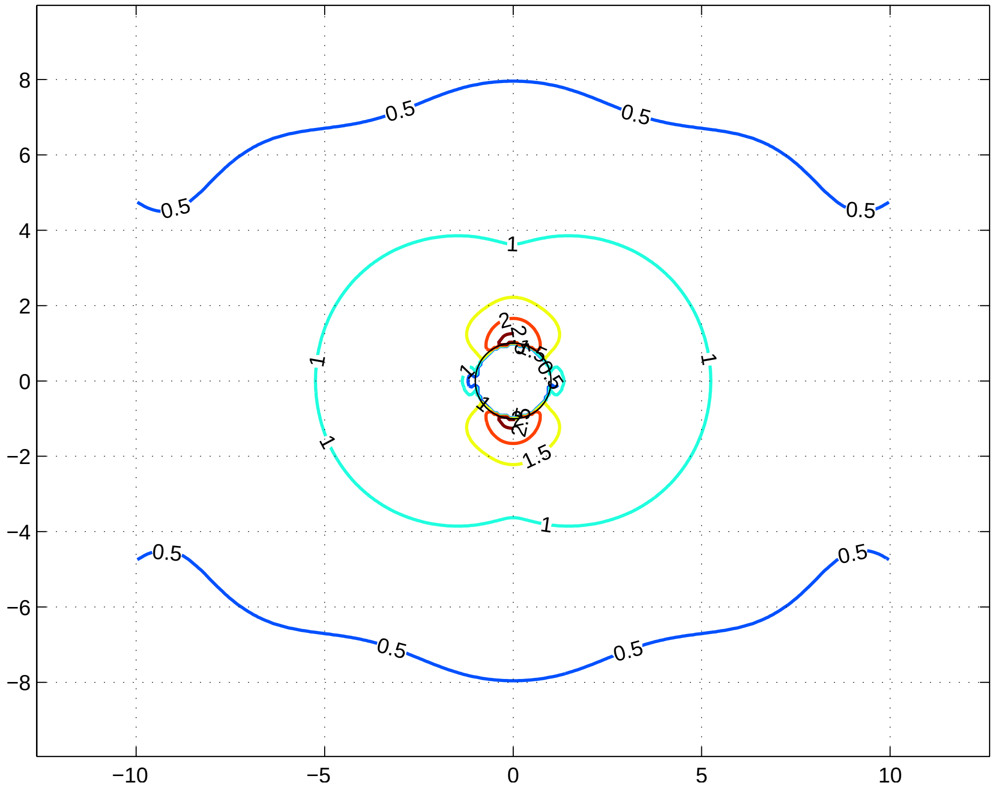

Figure 3.2: Contours of stress invariant for the case of a rising bubble. $Y_g = 0.1$, $Bo = \infty$, $Bn = 1.38$

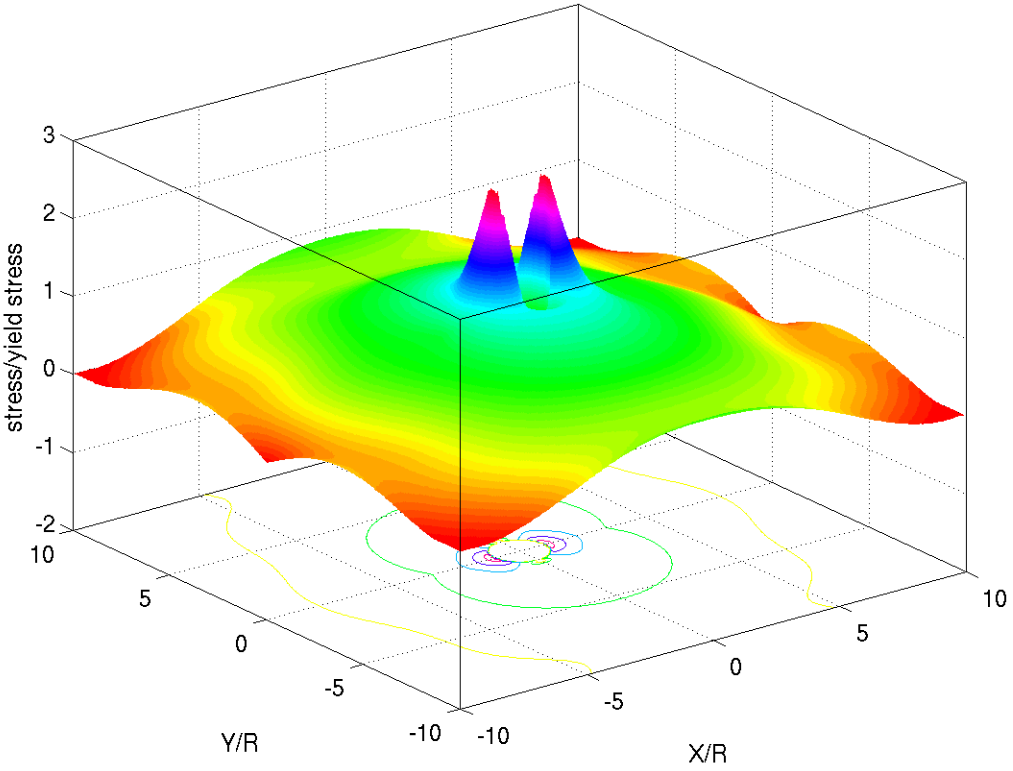

Figure 3.3: The surface plot of the normalized stress. The stress contours are shown on the "floor" of the plot. The transition from yielded to un-yielded is marked by the "green plateau". $\tau_y = 0.01$, $\sigma = 0$, $\rho_r = 0.01$, $\eta_r = 0.01$.

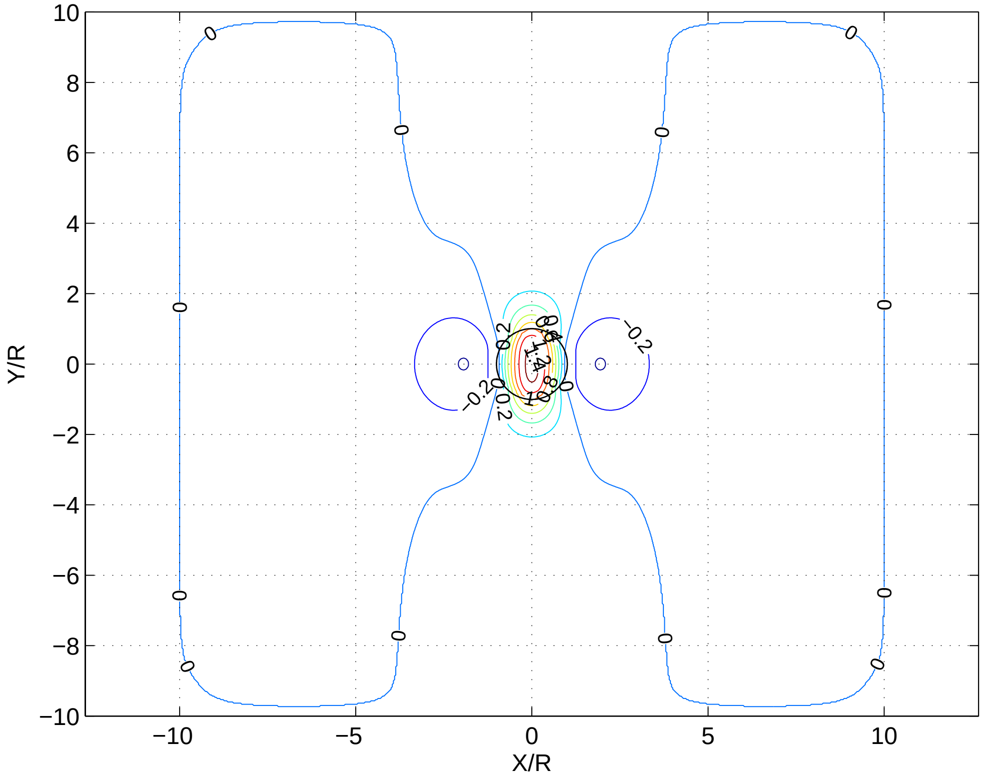

Figure 3.4: The y-velocity contours in the lab frame of reference. $Y_g = 0.1$, $Bo = \infty$, $Bn = 1.38$

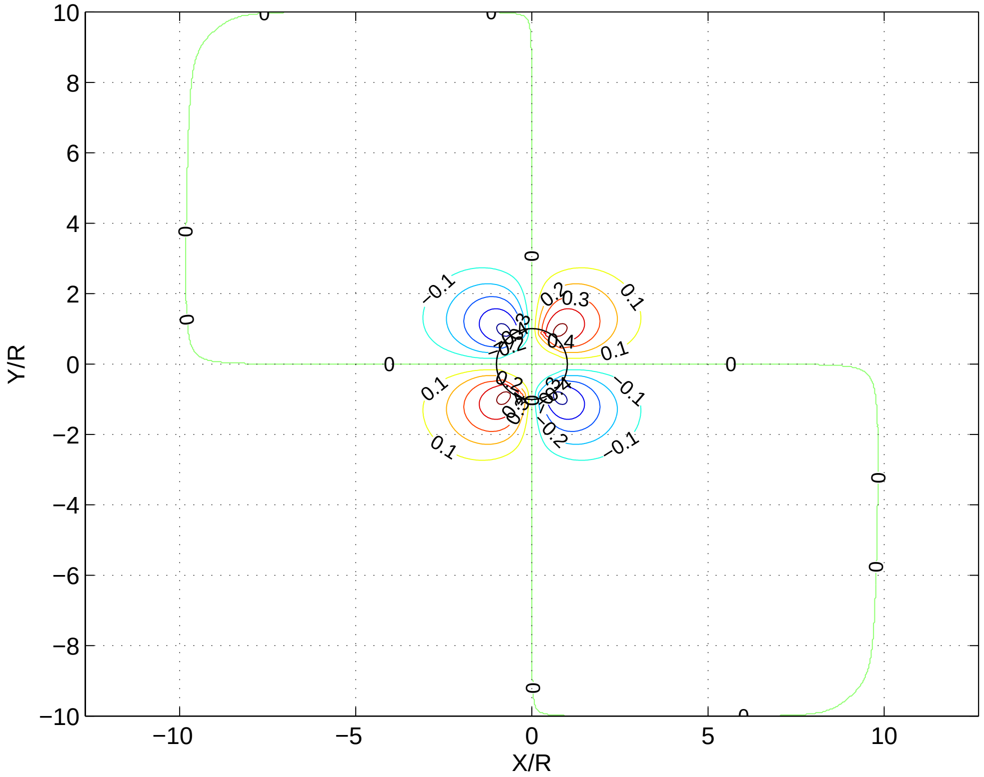

Figure 3.5: The X-velocity contours in the lab frame of reference. $Y_g = 0.1$, $Bo = \infty$, $Bn = 1.38$

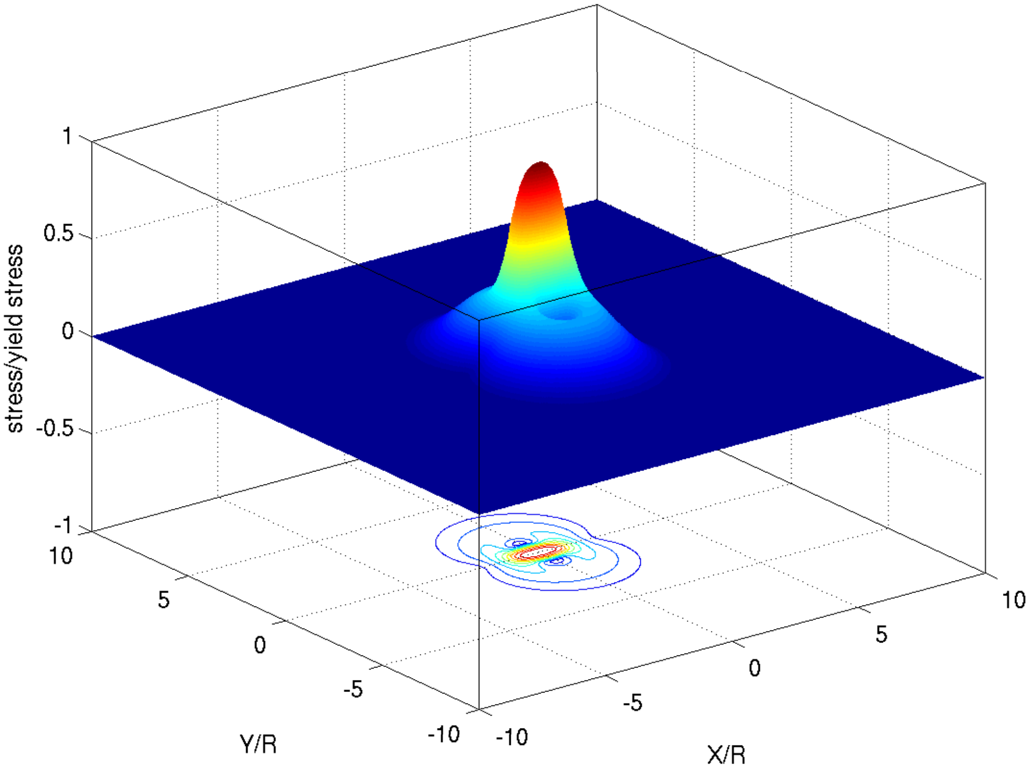

Figure 3.6: Surface plot of the velocity magnitude. $\tau_y = 0.01$, $\sigma = 0$, $\rho_r = 0.01$, $\eta_r = 0.001$.

3.4.1 Convergence

Convergence with respect to mesh

We used two different meshes (see table 3.1) to ensure that the results are independent of the mesh size. In Figure 3.7, the yield surfaces for a typical case using two meshes have been plotted. The parameters are as follows: $Bn = 1.97$, $\rho_r = 2$, $\eta_r = 1$, $Bo = \infty$. The regularization parameter used in the calculation for mesh $A1$ was $\epsilon = 4 \times 10^{-5}$ and for mesh $A2$ was $\epsilon = 6 \times 10^{-5}$. Despite slightly different values of the regularization parameter, there is almost no discernible difference between the yield surfaces obtained in the two cases. The stress on the y-axis and the equator (or x-axis) have been plotted in Figure 3.8. The symbol (□), or the blue color, represents the result of mesh $A1$ and the symbol (o), or the red color, the result of mesh $A2$. The results are converged with respect to the mesh density. Most of the calculations in this work were done using one of the two meshes. Generally, the smaller mesh was used for larger simulations, where the evolution of the bubble shape is being tracked. The finer mesh was used for cases where only a snapshot at a given time is required.

Table 3.1: Details of the two different mesh sizes used.

Mesh ID	no. of nodes	no. of elements
A1	160801	40000
A2	361201	90000

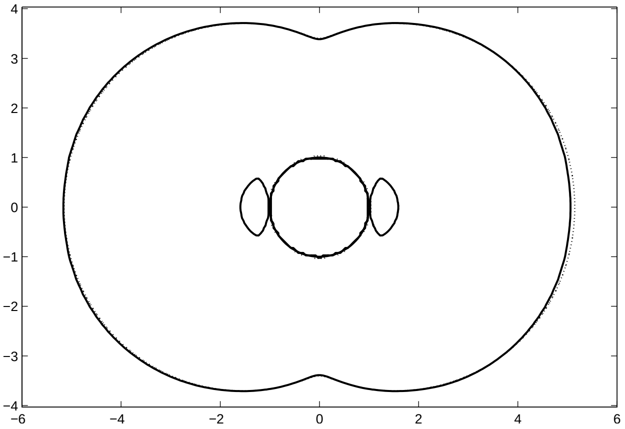

Figure 3.7: Yield surface for a drop falling in a Bingham fluid for two different meshes (A1 and A2). The solid line is for mesh A1 and the broken line for mesh A2. The results are converged with respect to the mesh as there is no discernible difference between the yield surfaces.

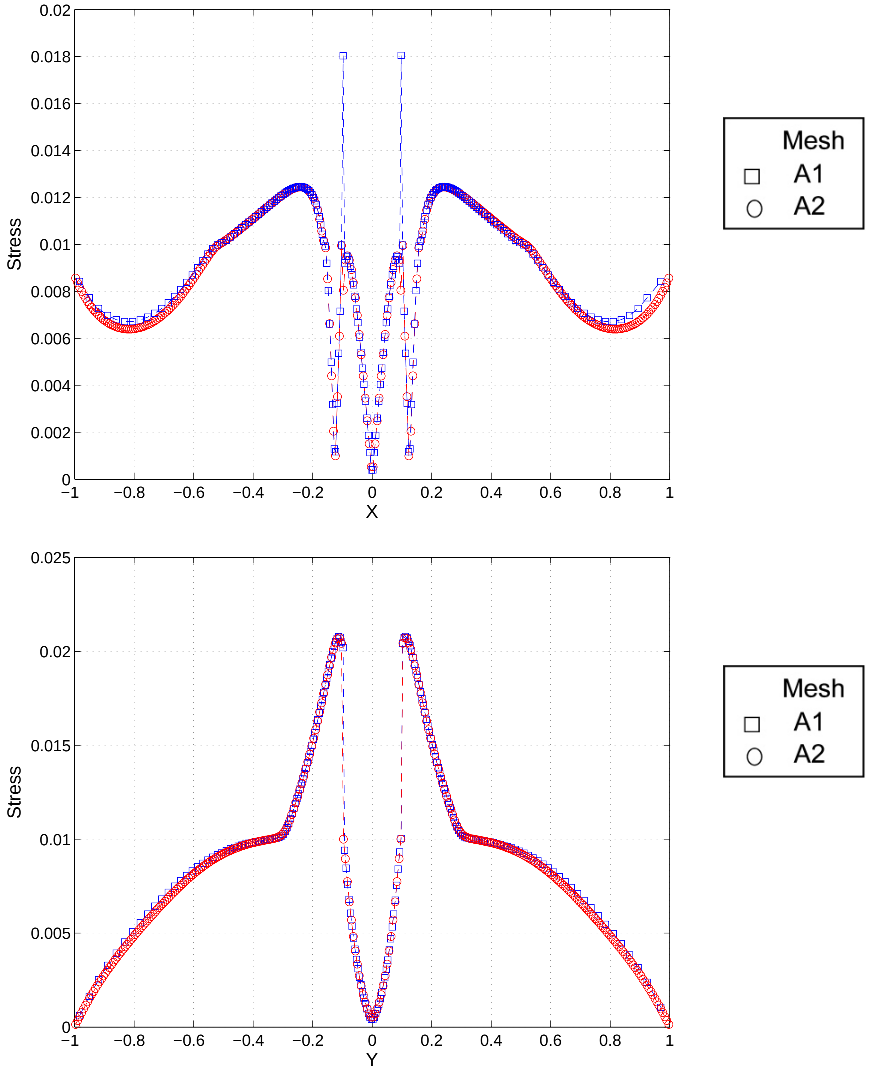

Figure 3.8: Stress invariant on the x and y-axis for two different meshes used.

Convergence with respect to regularization

The Bingham model, Eq. 3.6, is regularized to give a continuous equation for stress over the entire domain of the yield stress fluid. There is more than one way to regularize the Bingham model, as discussed in [FN05]. We recall that the regularized equation in this thesis is

$$\tau = \{\eta_p + \frac{\tau_y}{\sqrt{(\dot{\gamma}^2 + \epsilon^2)}}\}\mathbf{D}$$

where ϵ is called the regularization parameter. As $\epsilon \to 0$, the regularization equation tends to the exact Bingham model. In Figure 3.9, the stress invariant has been plotted on the equator and on the y-axis for three different values of the regularization parameter ($\epsilon = 2.5 \times 10^{-5}, 1 \times 10^{-5}$ and 3×10^{-6}). There is almost no change in the stress as we decrease the regularization parameter by one order of magnitude. Thus we conclude that the results are converged with respect to ϵ.

Convergence with respect to box size

The walls have been assumed to be far away from the bubble or drop, which is placed at the center. We need to check the validity of this assumption. Mitsoulis [Mit04] explored the wall effects on the yield surface for flow of a viscoplastic fluid around a solid cylinder. He observed that for $Bn > 1$ the drag coefficient is independent of box sizes ranging from 8 to about 50 times the diameter. For $Bn < 1$ the drag coefficient decreases as the box size is increased. This observation might be explained in terms of the fact that for small Bingham number, the Bingham model is very close to being a

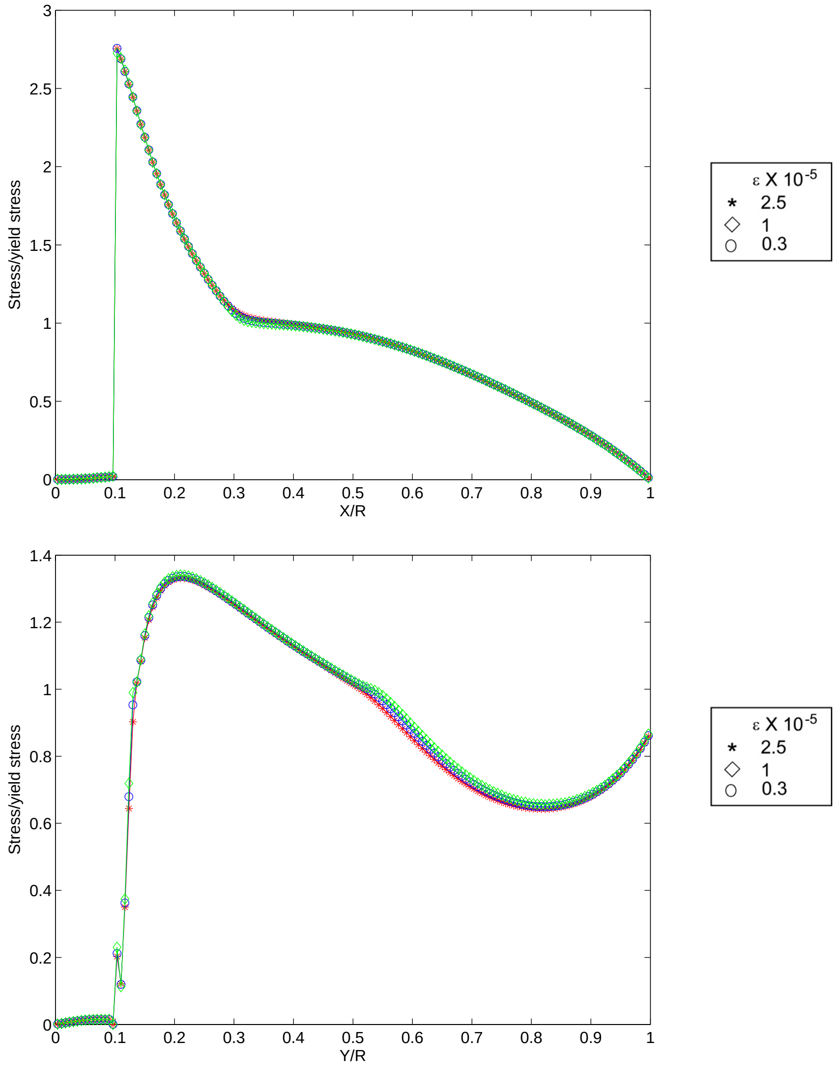

Figure 3.9: Effect of regularization parameter on stresses in x- and y-direction for the case of a bubble. $Y_s = 0.01$, $\eta_r = 0.01$, $\rho_r = 0.01$.

Newtonian fluid and numerical methods may not produce an accurate enough solution due to the Stokes paradox [Tan93].

In this work, the ratio of the box size H to the drop diameter $2R$ varies from 10 to 20. The drag coefficient, $C_s = \pi R^2(\Delta\rho g)/(\eta V)$, for a rising bubble is plotted in Figure 3.10 for two cases: $R1$ with $H/2R = 10$ and $R2$ with $H/2R = 20$. Figure 3.10 shows that there is almost no effect of the box size on the drag coefficient.

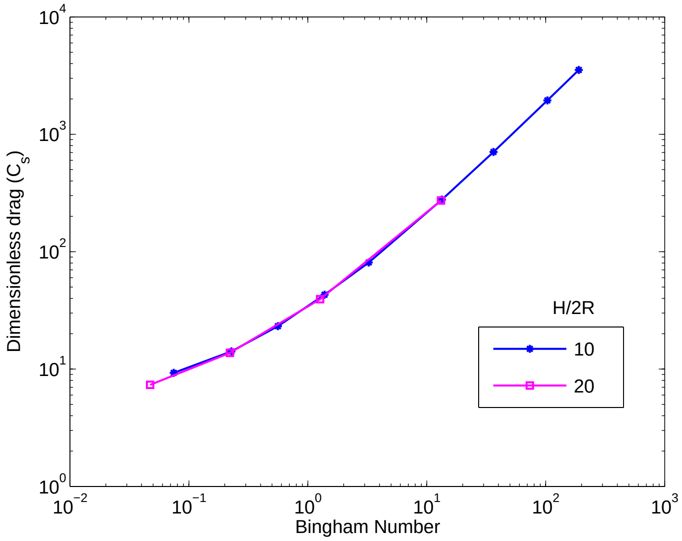

Figure 3.10: Drag coefficient with the Bingham number for bubbles of two different sizes. $H/2R = 10$ for $R1$ and $H/2R = 20$ for $R2$. The results for both the cases coincide, indicating that the results are independent of the box size.

3.4.2 Normal stress boundary condition on the interface

For any problem containing more than one phase there are certain boundary conditions that must be satisfied. At the interface, the tangential components of the velocity and tractions must be continuous. The normal tractions satisfy the following equation:

$$\hat{P} - P + ((\tau - \hat{\tau}) \cdot \mathbf{n}) \cdot \mathbf{n} = \sigma \nabla \cdot \mathbf{n} \tag{3.10}$$

where τ is the deviatoric stress and P is the pressure. A carat $\hat{()}$ denotes the physical quantity inside the dispersed phase.

For $\sigma = 0$, the equation just states that the normal stresses across the interface are balanced by the pressure difference:

$$\hat{P} - P = -((\tau - \hat{\tau}) \cdot \mathbf{n}) \cdot \mathbf{n} \tag{3.11}$$

Inside a bubble there can be no stress, requiring $\hat{\tau} \cdot \mathbf{n} = 0$. On a bubble surface we thus obtain,

$$\tau \cdot \mathbf{n} + (\hat{P} - P) = 0 \tag{3.12}$$

or, for a circular (or cylindrical) bubble and taking the pressure inside the bubble to be zero,

$$\tau_{rr} - P = 0 \tag{3.13}$$

where τ_{rr} is the rr component of the deviatoric stress tensor. Thus, a bubble surface can sustain non-zero deviatoric normal stresses, which are balanced by pressure.

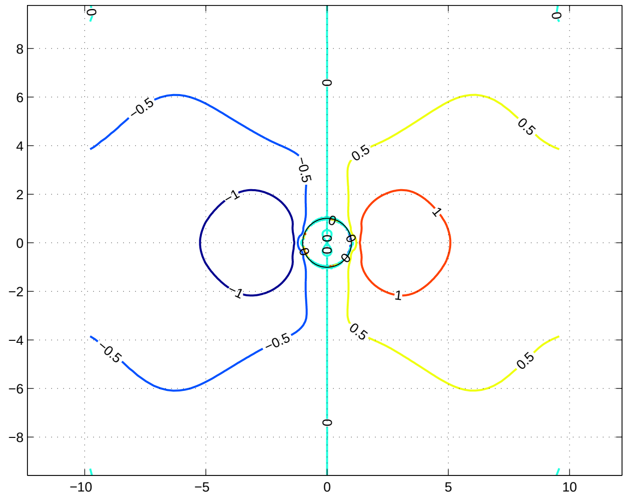

Figure 3.11: Contours of $r\theta$ component of stress tensor, normalized with the yield stress. Bubble with $Ca = \infty$

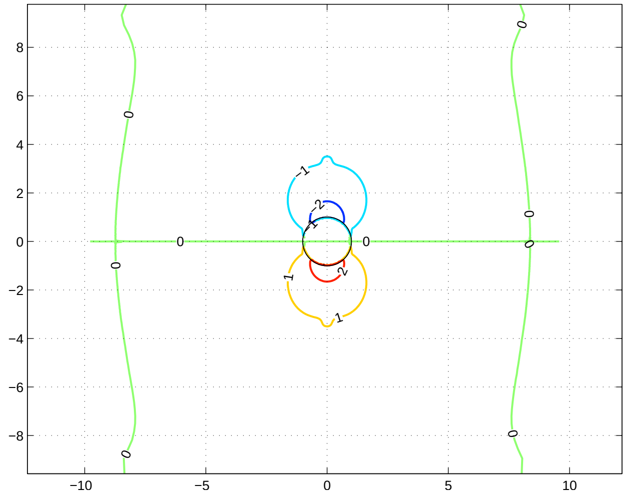

Figure 3.12: Contours of rr component of the stress tensor normalized with the yield stress. Bubble with $Ca = \infty$

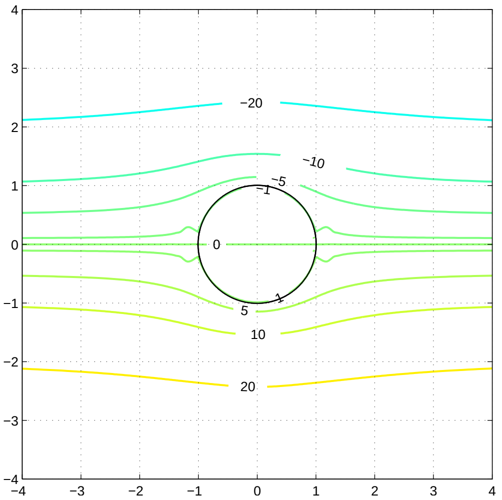

Figure 3.13: Pressure contours normalized with yield stress. Bubble with $Ca = \infty$

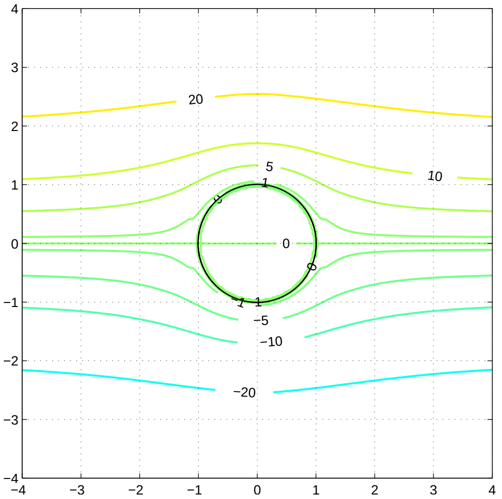

Figure 3.14: Difference between rr component of the stress tensor and the pressure. Note that the difference goes to zero almost everywhere on the bubble surface.

The $r\theta$ and rr components of stress are shown in Figures 3.11 and 3.12 normalized by the yield stress for a bubble rising with $\sigma = 0$ ($Ca = \infty$). Shear stresses are identically zero on the bubble interface (Figure 3.11). Also, the shear stress on the entire y-axis is zero, with fore-aft symmetry. The normal component of the stress (Figure 3.12) is zero on the equator; on the bubble surface it increases from zero on the equator to its largest magnitude on the poles. Thus, the deviatoric normal stress on the bubble is generally non-zero. From equation 3.12, this normal stress should be balanced by the pressure. The pressure contours are shown near the bubble in Figure 3.13, and the total radial stress $\tau_{rr} - P$ is shown in Figure 3.14. As we can see, this quantity is zero almost everywhere on the bubble surface, and we can conclude that the normal stress balance has been implemented accurately in the solution method.

3.4.3 Yield surfaces

The yield surface is defined as the surface in three dimensions or the curve in two dimensions that has a yielded domain on one side and an unyielded domain on the other side. Figure 3.15 shows typical calculated yield surfaces, where gray regions are unyielded and white are yielded. Bold lines dividing the two regions represent the yield surface. The outer boundaries of the container are beyond the outer yield surface, and the flow is independent of the length scale of the container. In this figure, the ratio of inner to outer fluid density is 0.01, the density difference is 1, and the ratio of inner fluid viscosity to η_p is 0.01. $Bn = 1.38$ and $Bo = \infty$. We note that the results are symmetric around the y-axis and there is also fore-aft symmetry. There is yielded domain, or a “shell”, around the bubble, and its extent is finite. The domain beyond this shell is unyielded everywhere.

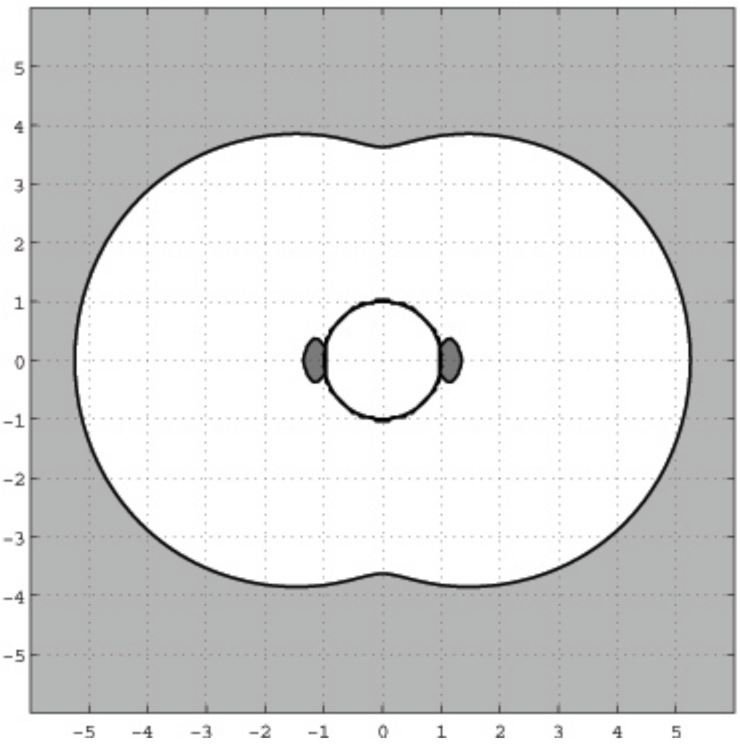

Figure 3.15: Shape of the yield surface for a rising bubble. The gray region is unyielded and the white is yielded. $Bn = 1.38$

There are two unyielded “ears” on the equator near the interface. Such an un-yielded region was also observed for the case of flow around a solid cylinder by Besses et al [BMJ03] and Mitsoulis [Mit04]. A similar region was observed in the work of Liu et at. [LMD02] for flow around a solid sphere, but in Liu's work the region was small and the size of this region decreased with the regularization parameter and looked like it would disappear in the Bingham limit. No such dependance on the regularization parameter was observed in this work.

There is a finite yielded region around an object moving in a viscoplastic fluid. In order to conserve mass, there has to be a region inside this yielded domain where we observe backflow. In two dimensions this backflow seems to result in a solid-body rotation of the unyielded region. For more information on the nature of backflow see section 3.4.4.

Another feature in the figure is that the "ears" are attached to the bubble surface. For flow around a solid cylinder the "ears" are observed to be further away from the surface of solid cylinder [Mit04]. Everywhere on the bubble surface the shear stress is zero. For the bubble to move through the matrix of yield stress fluid, it needs to overcome the yield stress. Thus, the bubble surface must have some regions which have a normal stress comparable to or greater than the yield stress so that it can "melt" the yield stress fluid around it. Clearly, the normal stresses on the equator must be zero, as the solution is fore-aft symmetric. On the equator, both normal and shear stresses are thus zero, and this is the reason for the existence of an unyielded region touching the bubble interface.

Figure 3.16 shows these ears for a bubble for different Bingham numbers ranging from 1.38 to 36.4. The recirculation in the two dimensional flow field induces rotation that causes a precession of the unyielded region. In all the results with $Bn > 1$ (Figure 3.16), there is a single large recirculating

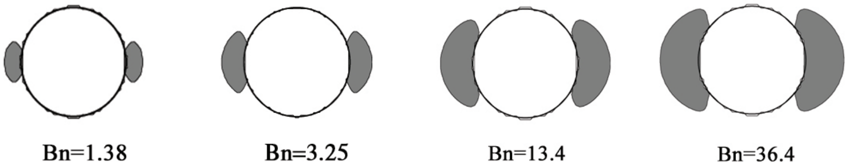

Figure 3.16: The shape of the un-yielded region for a bubble rising on the equator with increasing Bingham number [1.38, 3.25, 13.4 and 36.4]

unyielded region touching the bubble interface. For smaller Bingham number, $Bn < 1$, there is an indication that the recirculation is away from the bubble interface and hence leads to an unyielded region detached from the surface.

In Figure 3.17, the yield surface near the bubble surface is shown for $Bn = 0.227$. Other relevant parameters are $\eta_r = 0.01$, $\rho_r = 0.01$, $Ca = \infty$. The stress invariant on the equator is shown for the same set of parameters in figure 3.18. For small Bingham number the numerical results might not be accurate for the following reasons: First, the extent of the outer yield region is comparable to the size of the calculation domain, and hence there might be some effects from the presence of walls. Second, as is well known, the Stokes solution for a Newtonian fluid around a cylinder does not exist; for small Bingham numbers, the fluid properties are very close to being Newtonian and numerical solutions may not give accurate results, similar to Tanner's [Tan93] results on flow of a power-law fluid around a solid cylinder. Tanner observed that boundary integral methods do not match the analytical solutions for a small power law index. Third, the rotating unyielded region is very small and we would require a much finer mesh around that region to be sure about its existence.

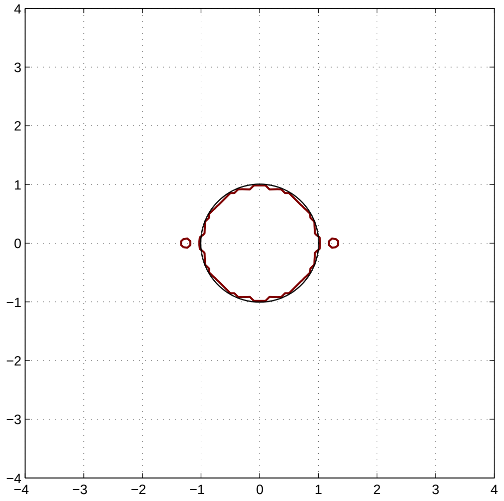

Figure 3.17: Yield surface near the bubble interface for small Bingham number ($Bn = 0.227$). The results might not be accurate as the fluid behavior is very close to Newtonian

In Figure 3.19 the normalized stress on the interface is plotted as a function of the x-coordinate for three different Bingham numbers: $Bn = 0.579$ (o), 1.77 ($*$) and 23.53 ($\diamond$). $x = 0$ corresponds to the point on the bubble surface on the equator and $x = \pm 1$ refers to the poles on the bubble interface. As the Bingham number is increased, the normalized stress decreases on the interface. At low Bingham number ($Bn = 0.579$), the stress everywhere is greater than the yield stress; at higher Bingham numbers the stress level falls below the yield value near the equator.

Figures 3.20 and 3.21 show the evolution of the unyielded region near the

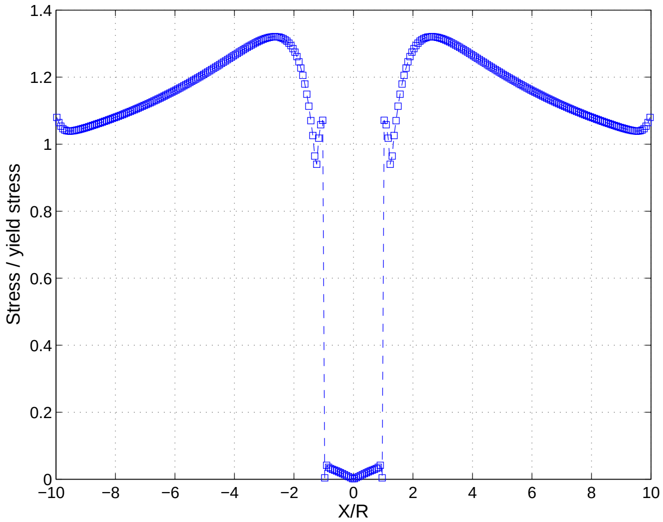

Figure 3.18: Stress invariant on the equator. $Bn = 0.227$.

falling drop and the very viscous drop, respectively, with increasing Bingham number. As the Bingham number is increased the unyielded region becomes attached to the surface. For the case of very viscous drops, the ears are never attached to the surface, as in the case for solid cylinders [Mit04].

Further evidence that such an un-yielded region can exist is provided by the vorticity ($\omega = \nabla \otimes \mathbf{U}$), which is a measure of the rotational tendency of the material. Figure 3.22 shows the contour plot for the vorticity. The dotted line is the yield surface. The un-yielded region near the drop has a constant vorticity over the entire domain, which means that the un-yielded region is rotating as a solid body, with a uniform angular velocity. Another feature in the vorticity plot is that nearly all of the vorticity is contained within the outer un-yielded surface, which is consistent with the conclusion that

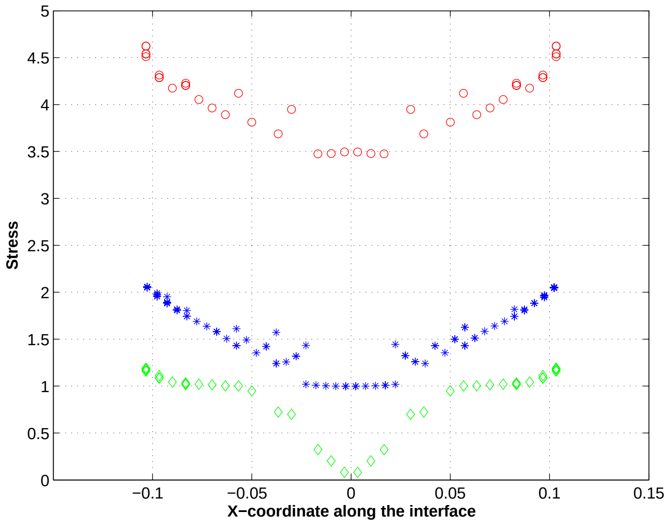

Figure 3.19: Effect of Bingham number on the stresses at the interface. The stress value (normalized with the yield stress) at the interface is plotted with its position in the x-direction. Bn = 0.579(red (o)) , 1.77(blue ($*$)) and 23.53(green ($\diamond$)).

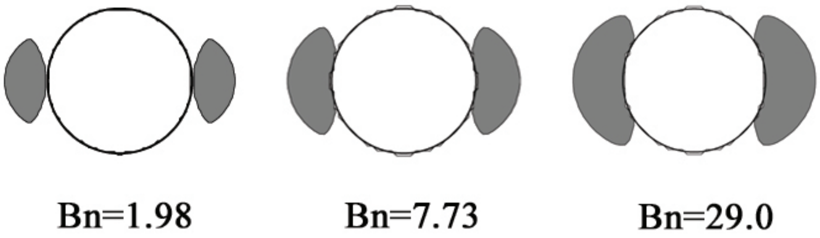

Figure 3.20: The shape of the un-yielded region on the equator for a falling drop with increasing Bingham number

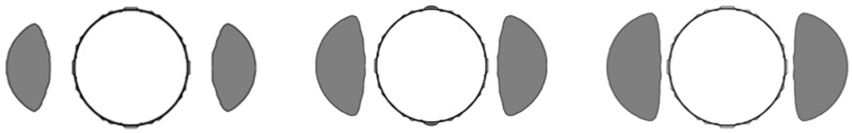

Bn=1.85 **Bn=10.7** **Bn=38.0**

Figure 3.21: The shape of the un-yielded region on the equator for a very viscous falling drop with increasing Bingham number [1.85, 10.06, and 37.67]

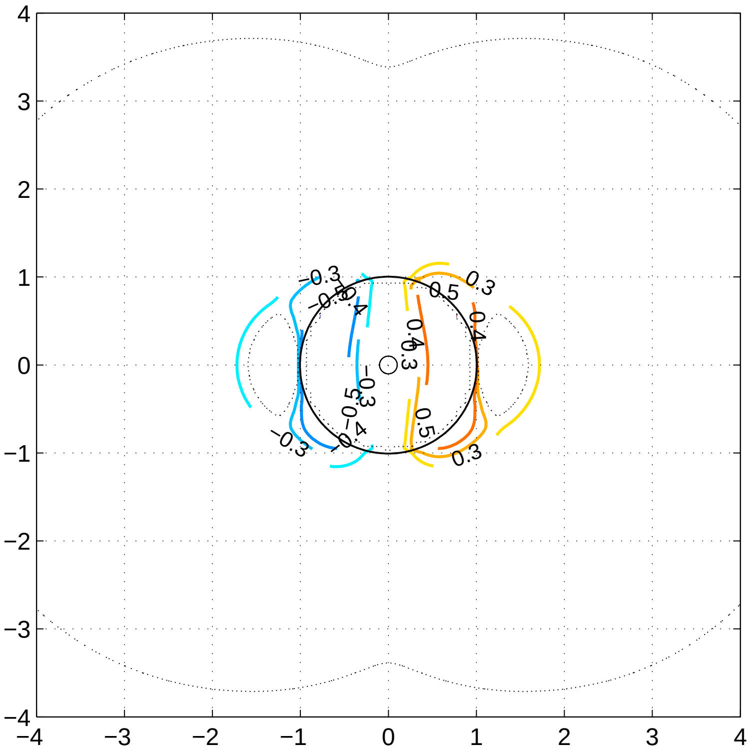

Figure 3.22: The vorticity contour plot for a falling drop. $Bn = 1.77$, $\eta_r = 1$, $\rho_r = 2$.

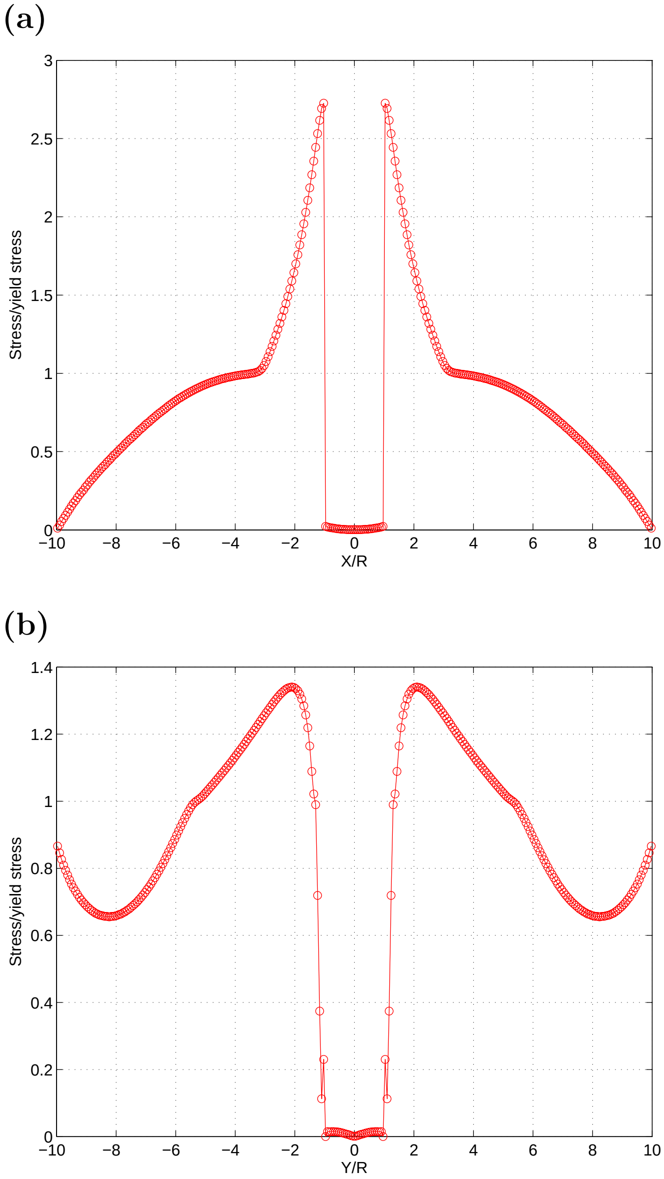

Figure 3.23: Plot of normalized stress in (a) the direction of the rising bubble and (b) in the perpendicular direction. The transition from yielded to unyielded is marked by the presence of an inflection point. $\tau_y = 0.01$, $\sigma = 0$, $\rho_r = 0.01$, $\eta_r = 0.01$.

the outer domain acts like a solid. The translation of these regions, which rotate as solid bodies and translate with the drop, is peculiar in the sense that material points inside this region keep renewing. Hence, this region is continuously being ‘melted’ on its trailing end and ‘re-formed’ with new material points on the leading end.

The stress normalized with the yield stress is plotted as a function of the coordinates on the interface in Figure 3.23. The signature of the yield stress in the form of an inflection point can be seen. We use the presence of the inflection point in the stress as an indicator for the yield surface in this work.

3.4.4 Backflow

Contours of velocity magnitude for a rising bubble are plotted in Figure 3.24. The velocity quickly approaches zero as we approach the outer yield surface. The streamlines in the laboratory frame of reference are shown in Figure 3.25a. The streamlines cross the interface in this frame of reference, which simply denotes the fact that the bubble itself is moving. If we draw the streamlines from the frame of reference moving with the center of mass of the bubble then we recover the familiar streamlines (Figure 3.25b). It is to be noted that the “back-flow” is not because of the closed box in which the bubble is rising, but it is rather due to the un-yielded outer fluid in the far-field. The flux in the yielded region is tabulated in Table 3.2 for different regularization parameters. A positive flux is the total flow rate in the direction of bubble rise. The total flux is the net flow rate in the yielded

Table 3.2: Details of flux in the yielded region. Total positive flux, total flux, ratio of positive to negative flux

Reg. Parameter	Positive flux	Total flux	Ratio
7.5×10^{-5}	5.32×10^{-5}	5.73×10^{-6}	0.892
2.5×10^{-5}	4.98×10^{-5}	1.71×10^{-7}	0.966
1.5×10^{-5}	4.92×10^{-5}	-9.07×10^{-7}	1.018
0.4×10^{-5}	7.06×10^{-5}	$-4.85 \times^{-7}$	1.0148

region, which should equal zero for mass conservation. The ratio of the positive flux and the negative flux does approach unity as the regularization parameter decreases.

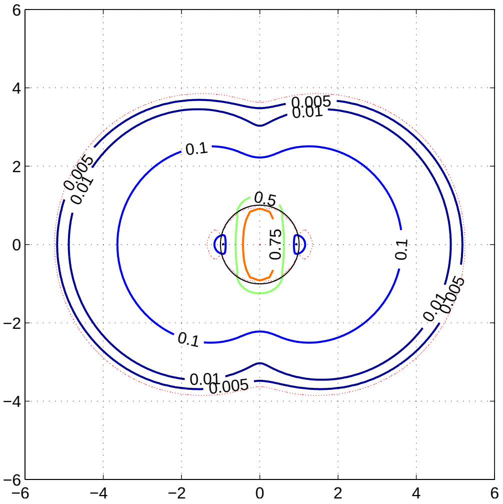

Figure 3.24: Contours of the magnitude of the velocity normalized by the maximum velocity. The dashed (red) line is the yield surface. $\tau_y = 0.01$, $\sigma = 0$, $\rho_r = 0.01$, $\eta_r = 0.01$.

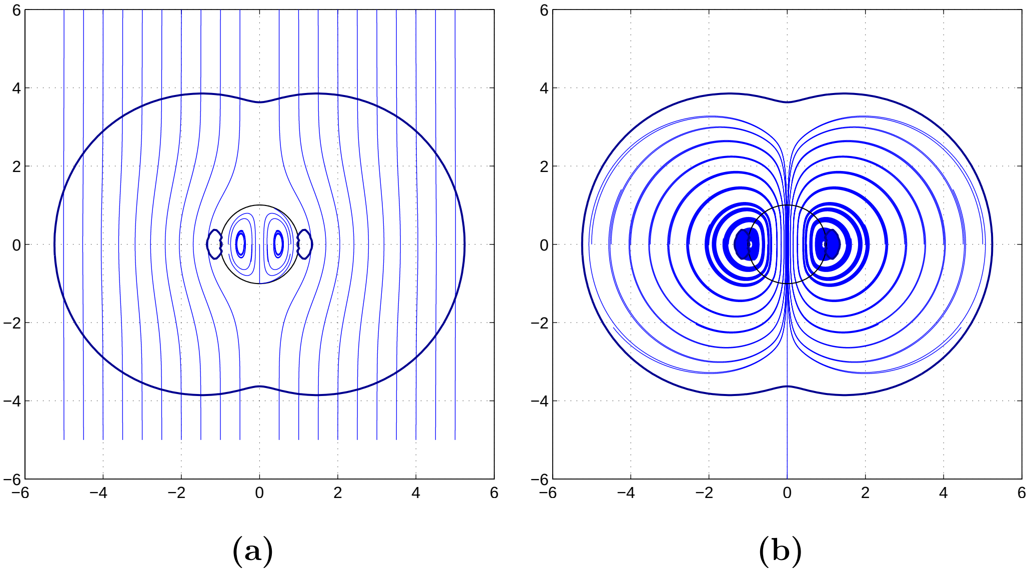

(a) **(b)**

Figure 3.25: Streamlines for a rising bubble, $Bn = 1.38$, (a) in the frame of reference of the bubble and (b) in the laboratory frame reference.

3.4.5 Effect of interfacial tension

Figure 3.26 shows the normalized stress invariant on the equator for three different Bond numbers ($Bo = \infty$ (o), 10.0 ($\triangle$) and 2.0 ($\diamond$)). The rise velocity observed in all the cases was essentially the same, with a Bingham number $Bn = 11.36$. Overall, no effect of surface tension was observed on the drag coefficient (C_s) for a circular bubble.

For a bubble rising in a Newtonian fluid, the spherical shape is the steady solution even for infinite Bond number. This means that the surface tension only contributes to the pressure field near the spherical bubble (see Leal [Lea92]). Thus, analogous to the case of bubbles in a Newtonian fluid, the surface tension plays little role in the stress field for a Bingham fluid as long as the bubble is circular. A change in the surface tension is balanced by the corresponding change in the pressure difference between the outside and inside of the bubble.

3.4.6 Effect of yield stress (Y_g)

As we increase the yield stress (dimensionless yield parameter, $Y_g = \frac{\tau_y}{\Delta\rho g R}$) it becomes harder for the bubble to move. The velocity of the bubble becomes smaller and the location of the outer yield surface moves closer to the bubble surface. The unyielded ears become larger in size. Ultimately, the ears and the outer unyielded region merge and the bubble comes to a complete stop. The value of Y_g at which this happens is called the critical dimensionless yield stress, or Y_g^*. Bn is plotted as a function of Y_g in Figure 3.27 for five

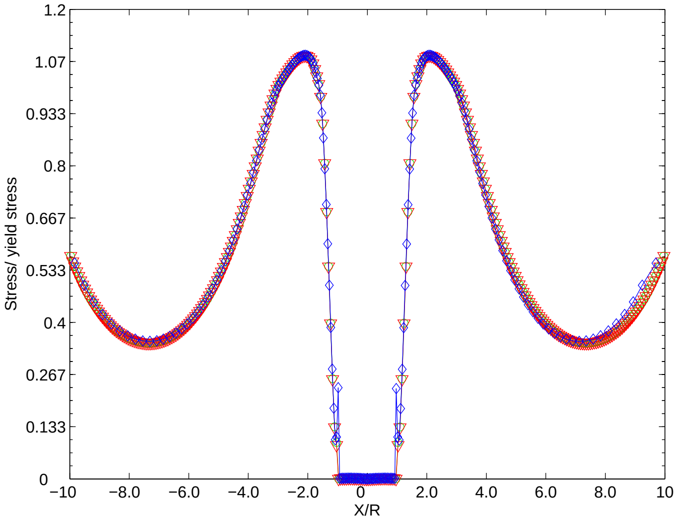

Figure 3.26: Plot of the normalized stress invariant on the equator at various Bond numbers. $Bo = \infty$ (o), 0.132 ($\triangle$), 0.026 ($\diamond$). Bingham number, $Bn = 11.36$, viscosity ratio, $\eta_r = 0.01$.

different cases: bubble ($\circledast$) $\eta_r = 0.01$ and $\rho_r = 0.01$; smaller bubble ($\Box$); drop (o) $\eta_r = 1$ and $\rho_r = 2$; very viscous drop ($\diamond$) $\eta_r = 1000$ and $\rho_r = 2$; and solid cylinder ($+$). $R/H = 20$ for all the cases except the "smaller bubble", where $R/H = 40$; there is no difference between the "smaller bubble" and the "bubble". Thus we can conclude that for the range of parameters in this paper we can neglect the wall effects. Modified Bingham number, defined as $Bn_m = \frac{Bn}{1+Bn}$ is also shown as a function of the dimensionless yield stress in the figure.

The value of Y_g^* at which a bubble will not rise is approximately 0.167. As we increase the viscosity ratio and we go from a bubble to a very viscous drop the value of Y_g^* falls to about 0.12. This can be explained by noting that a very viscous drop is similar to a solid cylinder, where the no-slip boundary condition retards the motion.

A slightly different version of the code was developed to study the flow of a yield stress fluid around a solid cylinder. The Bingham number for a solid cylinder was less than that for a very viscous cylindrical drop at a given value of the yield parameter, which is an anomalous result. This discrepancy can be attributed to the fact that for bubbles and drops, the physical properties (viscosity and the density) have been smoothed near the interface. When the change in physical properties is dramatic, as for very viscous drops, some error is introduced. In fact, the effective diameter of the drop is reduced by the order of the mesh size. If we replot the results using a lower value of radius ($R_{new} = R - h$, where $h = R \times 0.05$ is the mesh size near the interface) for the very viscous drop, the results overlap with the solid cylinder, as shown

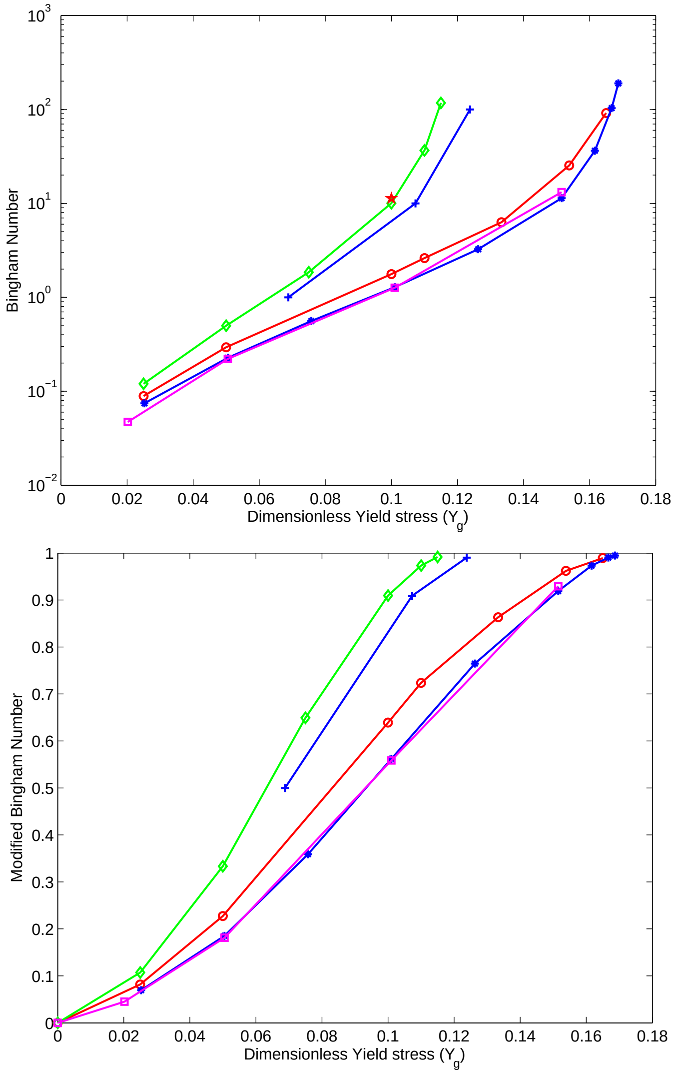

Figure 3.27: Plot of Y_g with Bingham number and Modified Bingham number for drop (o), bubble ($\divideontimes$), smaller bubble ($\Box$), very viscous drop ($\diamond$) and solid cylinder ($+$). As Y_g increases, it becomes harder and harder for drops to move. The minimum value of Y_g at which the drops stops to move is denoted by Y_g^*. Y_g^* decreases as the viscosity ratio increases.

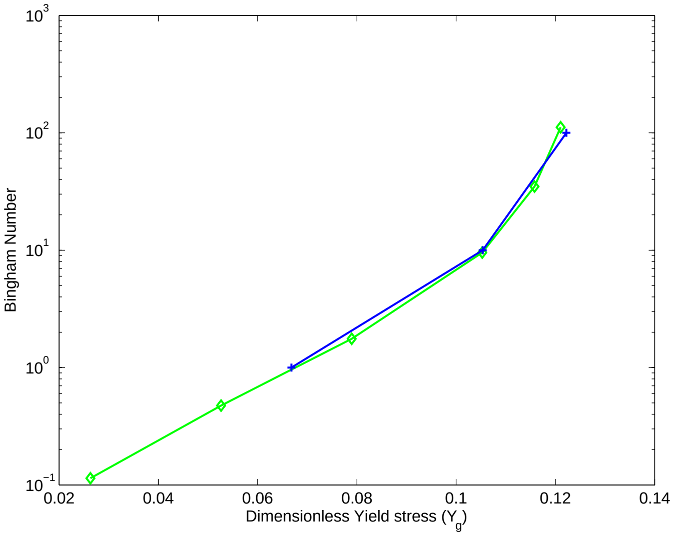

Figure 3.28: Plot of Y_g with Bingham number for very viscous drop ($\diamond$) and solid cylinder ($+$) using reduced radius (see text for details).

in Figure 3.28.

3.4.7 Drag coefficient

The drag coefficient, $C_s = \pi R^2(\Delta\rho g)/(\eta V)$, is plotted as a function of the Bingham number in Figure 3.29. It is worth noting that this is a different non-dimensionalization of stress than usual ρV^2. The drag coefficients for very viscous drops are comparable to the values obtained by Besses and coworkers [BMJ03]. All the results lie between the maxima ($\triangle$) and the minima ($\triangledown$) calculated using the variational results of Adachi and Yoshioka ([AY73]).

3.4.8 Evolution of a single rising bubble

The shape of a single rising bubble is of interest. In a Newtonian fluid a rising bubble always remains spherical under Stokes flow conditions [Lea92]. This is true irrespective of the Bond number of the bubble. Chhabra [Chh93] has an extensive review and references on the shapes and drag coefficients of rising bubbles in various Newtonian and non-Newtonian fluids.

The problem of a rising bubble in a non-Newtonian fluid like a power-law fluid is non-linear, and the exact solution is still unknown even under creeping flow assumptions. This problem has been approached only under the assumption of very small deviations from a Newtonian fluid, where the bubble is assumed to be spherical [See for example Hirose and Young[HMY69], Kawase and Ulbrecht [KU]and Bhavaraju *et al* [BMB78]]. Tsukada *et al* [TMHI90]

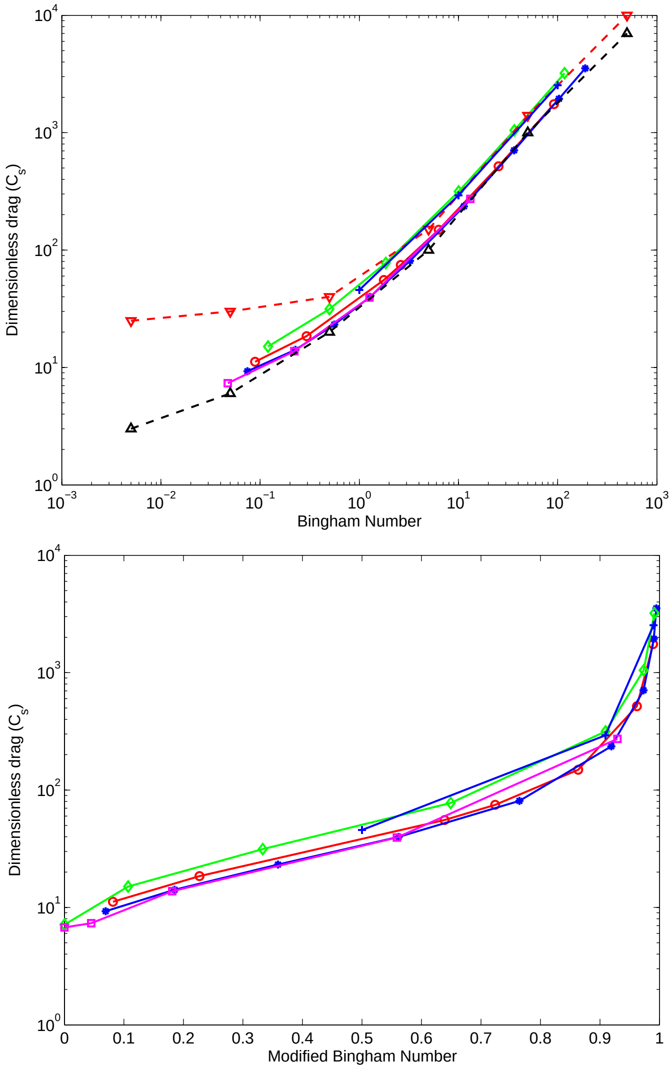

Figure 3.29: Plot of C_s with Bingham number and Modified Bingham number for bubble ($\divideontimes$), smaller bubble ($\square$), drop (o), very viscous drop ($\diamond$) and solid cylinder ($+$). Also shown are the variational bounds: maxima ($\triangle$) and minima (∇)

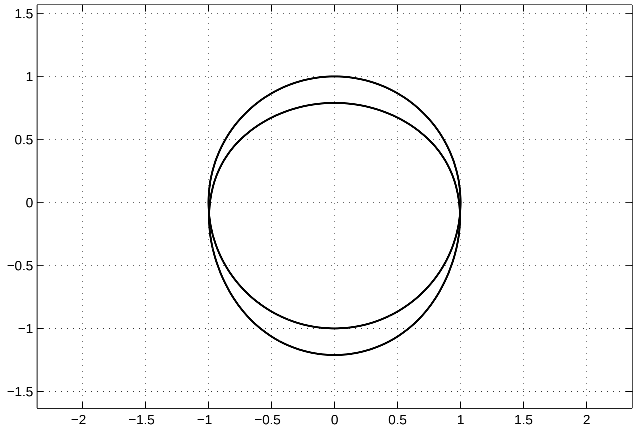

Figure 3.30: Evolution of a single drop falling. Time, $t = 72.5$, $Bn \sim 20$, $Y_g = 0.1$, $Ca = \infty$.

experimentally developed a shape map of bubbles rising in a power-law fluid. They show that the bubbles remain spherical for low Reynolds numbers.

For the case of a bubble rising in a yield stress fluid there is even less data available. Stein and Buggisch [SB00] report experimental data on the rise of bubbles in a pulsating pressure field. As far as we know there are no other experimental data on the shapes of a rising bubbles in a yield stress fluid. Potapov *et al* [PSLN06] report Volume of Fluid calculations of a falling drop in a Bingham fluid. They show that a single falling drop does not remain spherical in their calculations.

In our calculations we obtain a fore-aft symmetric solution with the normal stress boundary condition satisfied for essentially circular bubbles and drops irrespective of the magnitude of the Bond number. Figure 3.30 shows the shape of a falling drop after time $t = 72.5$. [$Bo = \infty$, $Y_g = 0.1$,

$Bn = 1.77$]. The drop evolves to a shape that is only slightly different from circular; any deviation from a circular shape could be the result of the small error associated with the calculations. Furthermore, the calculations shown here have infinite Bond number, which is the most sensitive case in terms of stability of the circular solution. For flow of a Newtonian fluid around a bubble, the spherical shape is the solution of the creeping flow equations, although the solution is unstable under infinitesimal perturbations.

3.5 Conclusions

Converged results have been obtained for a steady two-dimensional rising bubble or a drop in a yield stress fluid. The domain size is large enough that the wall effects can be neglected. A finite yielded domain around the bubble is obtained. Two rotating unyielded "ears" are also obtained around the bubble. These results are very similar to the results for flow around a solid cylinder. The rotating ears for a bubble are always attached to the bubble surface. This is in contrast to a solid cylinder, where these regions are detached from the solid surface. For the intermediate case of a drop, the rotating ears are attached to the surface for high Bingham number, but are detached at low Bingham number.

The critical yield parameter for the bubble is around 3/4 times the value for a very viscous drop or a solid cylinder. No effect of surface tension on the critical yield parameter or on the drag experienced by the circular bubble was observed.

Chapter 4

Interacting bubbles

4.1 Introduction

At the US Department of Energy's Hanford site it has been observed that large bubbles sometimes rise to the top of a tank of radioactive colloidal waste sludge and burst. This phenomenon adds to the storage concerns that radioactive materials pose. Small gas bubbles that are present in the radioactive sludge apparently come together and coalesce to form large bubbles. The radioactive waste exhibits a yield stress [GTD$^+$97]. The phenomenon of bubbles overcoming a yield stress, coming in close contact to each other and then coalescing is not well understood. This chapter is an attempt to explore this physical phenomenon using the computational tools described in chapter 2. It builds on the results of a single rising bubble in a viscoplastic fluid presented in the previous chapter and tries to explore the effect of the presence of another bubble in the vicinity of the first. The next section presents a brief snapshot of the prior work on which the current study stands. That is followed by the results of two and three interacting bubbles with various initial configurations.

4.2 Literature Survey

Interacting bubbles rising under conditions of low Reynolds number form the basis of the dynamics of many multiphase systems, which are important in various industrial processes. Generally, in a multiphase system, the bubbles are interacting, deforming, colliding, coalescing or breaking up, giving rise to a very complex fluid mechanical problem. Two or three interacting bubbles under creeping flow conditions form a useful model to study such a complex system.

For two interacting bubbles or drops in a Newtonian fluid there has been an extensive literature in the past several decades. Davis and coworkers [DSR89] analyzed the flow field for two drops very close to each other using lubrication analysis. Rother, Zinchencko and Davis [RZD97] then used matched asymptotic methods to analyze the effect of slight deformation on coalescence efficiency. Leal and his group ([Lea04] and references therein) have studied drop interaction and coalescence using four roll mills and computational tools like boundary integrals. Baldessari and Leal [BL06] extended the analysis of Rother *et al* to take into account the overall deformation of drops on coalescence. These studies concentrate on the regime where the deformation is neglected or is very small ($Ca << 1$).

At the other end of the spectrum is the case of very high Bond number, where the deformation is large. Manga and Stone [MS93] conducted experiments and boundary integral calculations to study collinearly rising drops in a Newtonian fluid. They concentrated on the regime in which the buoyancy force is dominant as compared to the surface tension ($Bo > 1$), and they showed that the hydrodynamics cause the rising bubbles to align and increase the coalescence efficiency. Kushner and coworkers [IRD01] conducted experiments and verified the conditions for such interactions as separation, capture, breakup and pass-through for two interacting bubbles.

All of the aforementioned literature deals with Newtonian fluids. There has been very little work on interacting bubbles in non-Newtonian fluids. For a review of the motion of bubbles and drops in non-Newtonian fluids see Chhabra [Chh93]. Potapov and coworkers [PSLN06] conducted a numerical study of falling drops under gravity in cylindrical tubes using volume of fluid methods implemented in the commercial CFD code FLUENT. They observed that the falling drops can coalesce and then fall together as a single drop. There has been no experimental work on interacting drops or bubbles in a yield stress fluid.

For the Newtonian fluid, one of the main tools for the case of two drops close to each other is lubrication analysis. It has been shown by Lipscomb and Denn [LD84] that lubrication analysis may give incorrect unyielded regions in the squeeze flow problem. They show that the terms usually neglected in the lubrication analysis are significant for a yield stress fluid and hence cannot be neglected. Thus, analytical work in studying yield stress fluids is limited.

In this chapter the mechanics of two and three interacting bubbles in a yield stress fluid are explored.

4.3 Collinearly rising bubbles

This section deals with the case of two bubbles rising collinearly. Figure 4.1 depicts the schematic of the initial configuration and shows the variables involved. The initial distance between the drops is D. The physical properties of both the drops are the same; i.e. they have the same viscosity and density.

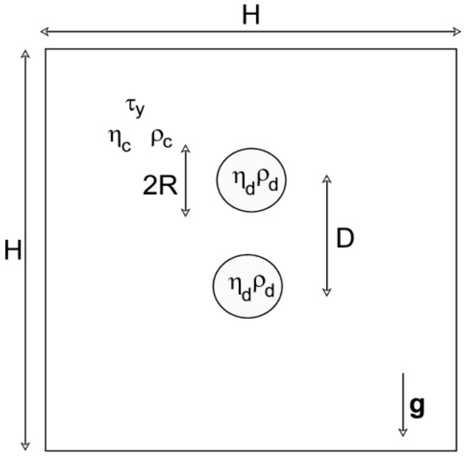

Figure 4.1: Schematic of the initial configuration for collinearly rising bubbles

4.3.1 Yield surface and unyielded regions

The dimensionless yield stress based on a single bubble is defined as

$$Y_g = \frac{\tau_y}{\Delta\rho\mathbf{g}R} \tag{4.1}$$

where τ_y is the yield stress, $\Delta\rho\mathbf{g}$ is the gravitational force per unit volume, and R is the radius of the bubble. Other relevant dimensionless parameters are the Bond number, $Bo = \frac{\Delta\rho\mathbf{g}R^2}{\sigma}$, which is the ratio of buoyancy force to the surface tension force; the Bingham number, $Bn = \frac{\tau_y R}{V\eta_p}$, which is the ratio of the yield stress to the viscous force; and the viscosity ratio, $\lambda = \eta_d/\eta_p$. The characteristic length (R) is chosen to be the radius of the larger bubble in the case of two bubbles of different size, and the characteristic velocity is the velocity of the center of mass of the bubbles.

In Figure 4.2 the yield surfaces at time $t = 0$ for the case of two collinearly rising bubbles of the same size are shown. The initial distance between the centers is $D = 2.5R$. The gray region is the unyielded region and the white region is either yielded or is the inner Newtonian fluid region (inside the bubbles). Here, the yield stress $Y_g = 0.2$, the Bond number $Bo = 10$, the Bingham number $Bn = 2.25$, and the viscosity ratio, $\lambda = 0.01$. There is an outer unyielded region and there are two unyielded “ears” very similar to the ones obtained in the case of flow of a yield stress fluid around a single cylindrical bubble or a solid cylinder. Because of the outer yield surface there is a recirculating flow, which induces a rotation. Such recirculation gives rise to an unyielded region in two dimensional flows similar to flow around a cylinder or a bubble. As the bubbles rise these unyielded regions “melt”

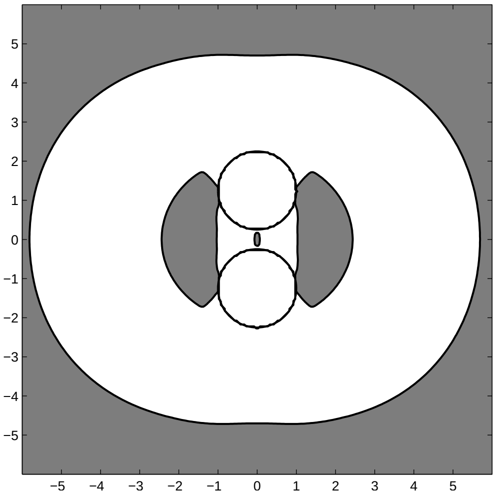

Figure 4.2: Typical yielded regions obtained for two collinearly rising bubbles of the same size. The unyielded regions are shown in gray. $Y_g = 0.2$, $Bo = 10$, $\lambda = 0.01$, $Bn = 2.25$

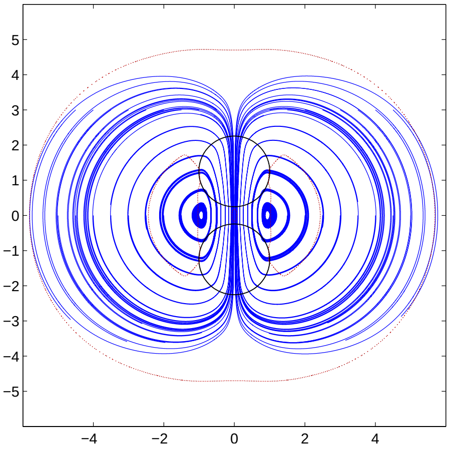

Figure 4.3: The streamlines for two equal sized bubbles rising (laboratory frame of reference).

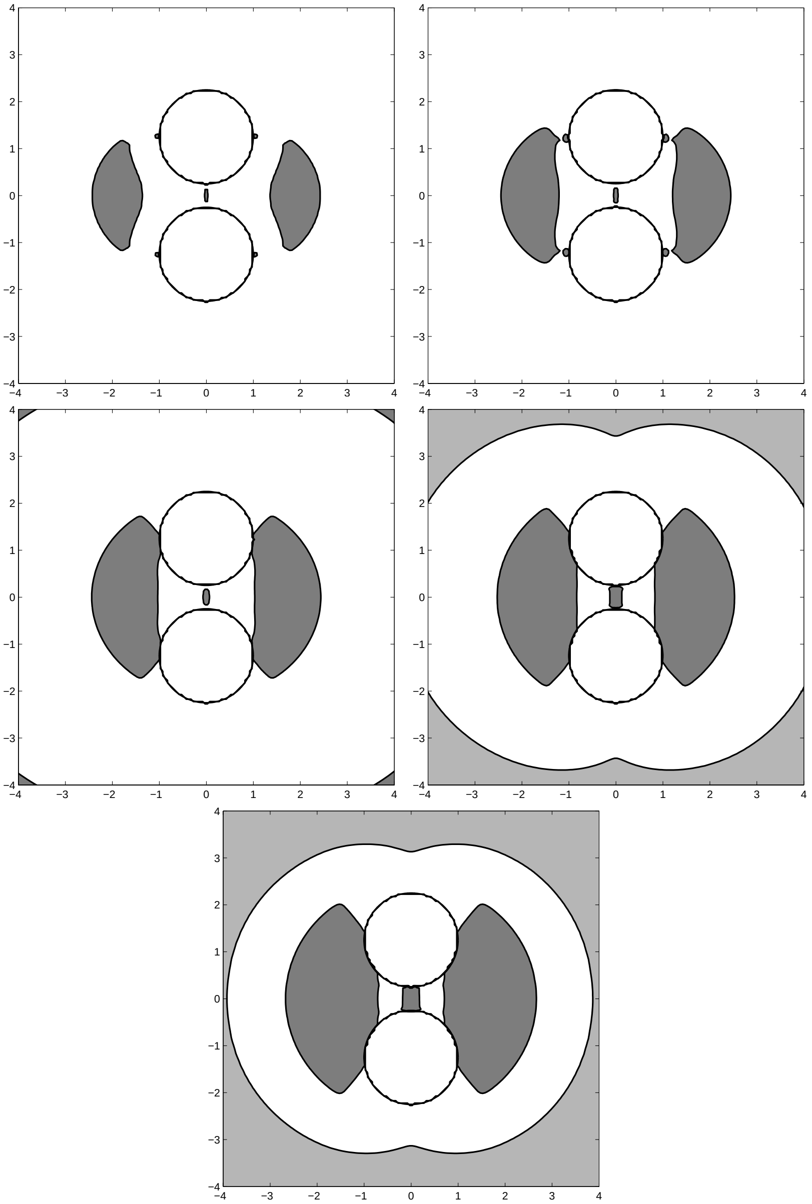

Figure 4.4: Effect of yield stress on the shape of unyielded region (shown in gray). $Y_g = 0.125$, 0.15, 0.2, 0.25 and 0.275. Corresponding Bingham numbers: $Bn = 0.61$, 0.82, 2.25, 9.06 and 33.21

and “reform” at the trailing and leading ends, respectively. In Figure 4.3 the streamlines from the laboratory reference frame are shown depicting the recirculation.

In Figure 4.4 the unyielded regions for different values of Y_g are shown: $Y_g = 0.125$, 0.15, 0.2; corresponding Bingham numbers are $Bn = 0.61$, 0.82, 2.25[1]. The initial distance between the centers is $D = 2.5R$. For the low values of Y_g the rotating “ears” are detached from the bubble interface. In addition, there are small unyielded regions located near the equatorial planes of each bubble. These unyielded regions are very similar to those obtained on the surface of a single rising bubble in a yield stress fluid [chapter 3]. For a single bubble the normal component of the stress is zero on the equatorial plane due to the fore-aft symmetry and the shear component of the stress is zero as the bubble surface is incapable of sustaining shear. Thus, the unyielded regions on the equatorial plane of a bubble are obtained. For larger yield stresses the rotating “ears” become larger and the unyielded regions on the bubble interface merge with these large rotating “ears”, as seen in the second and third image in Figure 4.4.

There is a small unyielded region on the y-axis mid-way between the rising bubbles. The reasons why it can exist is that both the bubbles are of same size and shape to begin with and thus are rising at the same velocity. This gives rise to a region with uniform velocity between the bubbles, leading to

---

[1] c.f. It has been shown by Tanner [Tan93], that the creeping flow solution exists for the flow shear thinning fluid around a cylinder. It is required that $Bn > 1$ to have sufficient shear thinning behavior to obtain accurate numerical solution.

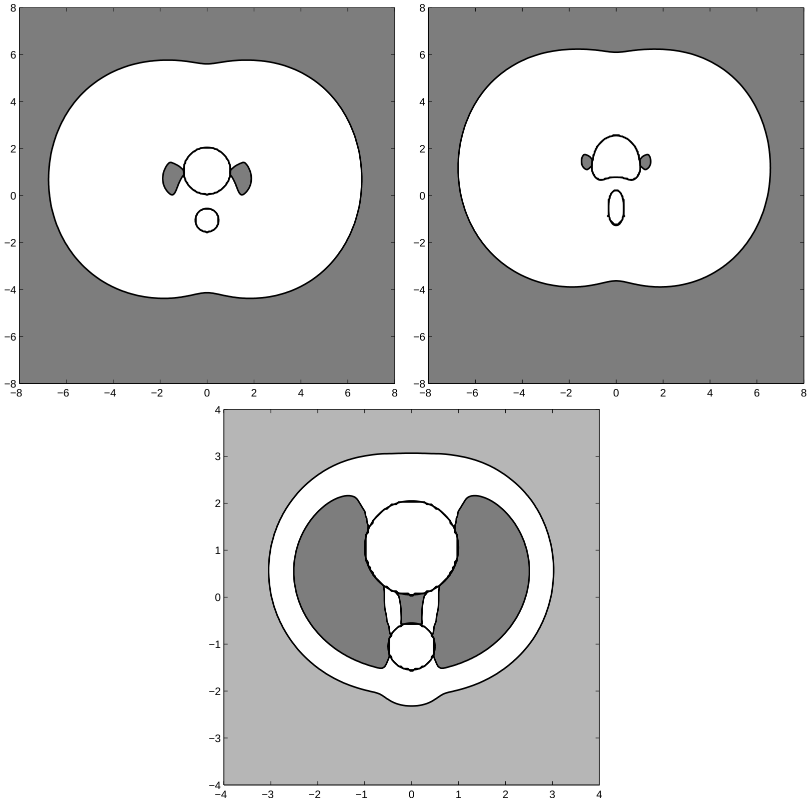

Figure 4.5: Typical yielded regions obtained for two collinearly rising bubbles of different size. The radius of smaller trailing bubble is half the radius of the larger bubble. The physical properties of both the bubbles are same. The unyielded regions are shown in gray. **For first two figures:** based on the larger bubble, $Y_g = 0.1$, $Bo = 10$, $\lambda = 0.01$, $\bar{t} = 0$, 0.81. Bingham number at time zero $Bn = 0.79$ **Third figure:** $Y_g = 0.2$, $Bo = 10$, $Bn = 84.74$

an unyielded region. In the case of two unequal bubbles rising collinearly, this unyielded region would not exist. See Figure 4.5 for the case of a smaller bubble trailing behind the larger one. The trailing bubble has a radius equal to one half of the larger bubble. The initial distance between the bubbles $D = 2R$. where R is the radius of the larger bubbles. $Y_g = 0.1$ for the top two frames and $Y_g = 0.2$ for the bottom frame, based on the larger bubble. There is no unyielded region on the equatorial plane of the smaller bubble when for $Y_g = 0.1$. At the smaller value of dimensionless yield stress $Y_g = 0.1$ the smaller bubble alone will not be able to rise and at the higher value ($Y_g = 0.2$), both the bubbles alone cannot rise.

4.3.2 Effect of initial distance

The buoyant force must exceed the integrated yield stress on the surface for any motion to take place. For a given yield stress of the fluid, there is a critical size that a bubble must exceed in order to rise. Bubbles or drops that are too small to overcome the yield stress individually may move as pairs when they are sufficiently close to each other.

Figure 4.6 shows the effect of the initial distance (D) between the rising bubbles, with $D/R = 2.1$, 2.5, 4.0 and 6.0. The dimensionless yield stress based on a single bubble is $Y_g = 0.2$, which is greater than the critical yield stress for a single bubble ($Y_g^* = 0.167$); i.e., a single bubble is not able to overcome the yield stress of the fluid and rise. As is evident from the figure, however, two bubbles can rise together if they are sufficiently close to each other. If the initial distance between the bubbles is of the order of $6R$, they no longer feel the effect of each other and they do not rise (last image in Figure 4.6). A similar result was obtained by Liu and coworkers [LMD03] for flow past two collinear spheres, where they reported that the yielded regions of individual spheres do not interact when the distance between the spheres is $D \sim 5R$.

A similar result is obtained when the yield stress is less than the critical value, as shown in Figure 4.7. Here, $Y_g = 0.15$, which is less than the critical yield parameter (${Y_g}^* = 0.167$). At $D \sim 8R$, the bubbles are almost completely enclosed in their own yielded regions, and there is almost no interaction between them. As the initial distance between the bubbles is increased, the size of the rotating ears increases and the size of the unyielded regions on the equatorial planes of each bubble increases. At $D \sim 8R$ the region of rotating ears becomes connected to the outer unyielded region and the unyielded region on the equatorial plane of each bubble becomes attached to the bubble surface.

4.3.3 Effect of yield stress on evolution

The time evolution of two two-dimensional bubbles in a Newtonian fluid is shown in Figures 4.8 and 4.9 . There is a no slip boundary condition on the walls of the container, so this is not a simulation of two bubbles rising in an infinite Newtonian fluid but rather in a closed container; the walls of the container are assumed to be too far away to present any significant effect

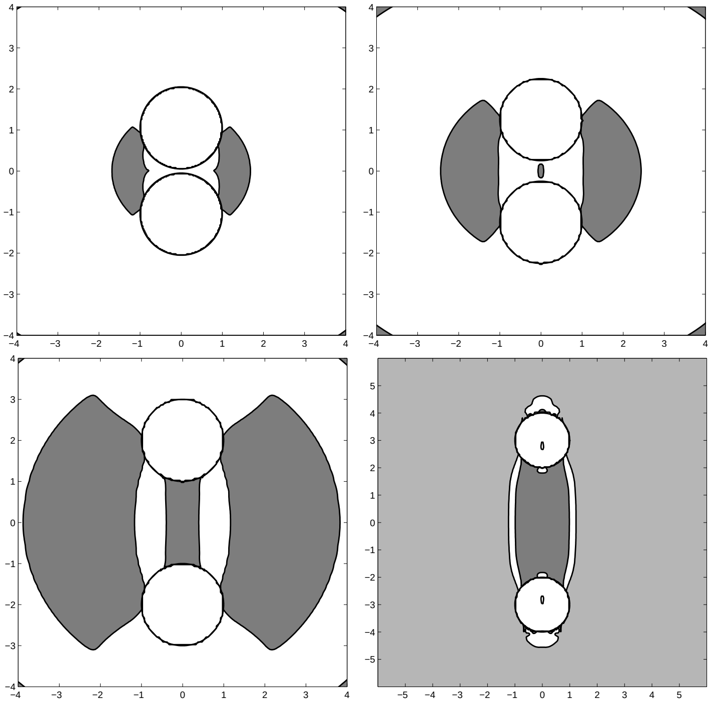

Figure 4.6: The effect of initial distance (D) between the center of bubbles on the yield surface. Each bubble individually will not be able to rise (Yield parameter is greater than the critical yield), but if the bubbles are close enough, they can rise together. D/R = 2.1, 2.5, 4.0, 6.0; Corresponding Bingham numbers Bn = 1.17, 2.25, 18.21, 1188.4 $\sim \infty$; $Y_g = 0.2$, $\lambda = 0.01$, $Bo = 10$

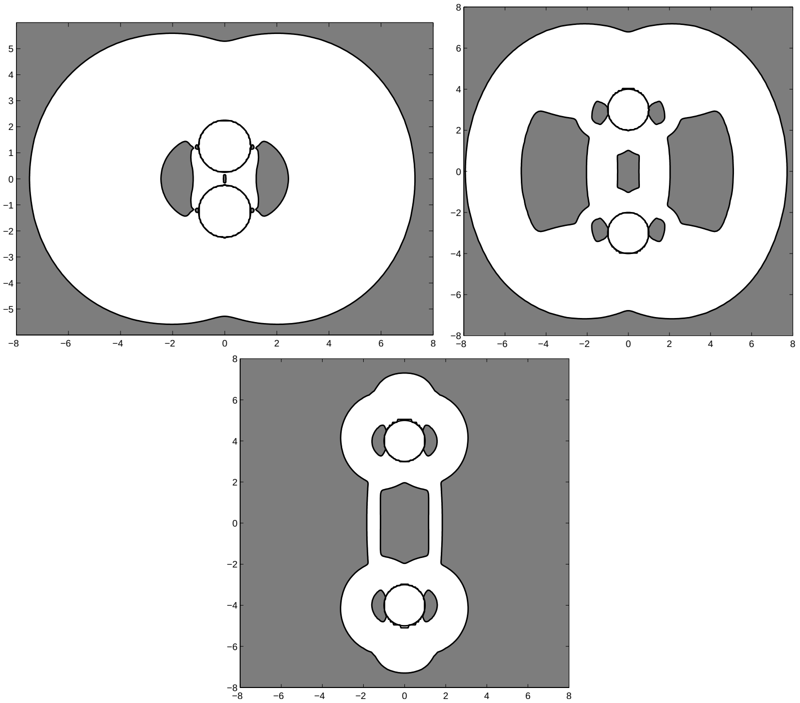

Figure 4.7: The effect of initial distance (D) between the center of bubbles on the yield surface. The yield parameter is less than the critical yield. $D/R = 2.5$, 6.0, 8.0; $Y_g = 0.15$, corresponding Bingham numbers $Bn = 0.82$, 4.90, 13.71. Bingham number for a single bubble rising under same conditions is 13.39, which is almost same as the last case shown here. $\lambda = 0.01$, $Bo = 10$

on the evolution, however. The Bond number $Bo = \Delta\rho\mathbf{g}R^2/\sigma$ equals 10 and 2, respectively, and the dimensionless yield stress $Y_g = \tau_y/(\Delta\rho\mathbf{g}R)$ is of course equal to 0. The trailing drop starts out with a circular cross-section and then becomes extended in the direction of the motion. It then assumes a "parachute" shape and develops a tail, which elongates with time. The leading drop flattens, becomes convex at its lower edge, and envelopes the top of the trailing drop. Ultimately, the simulation predicts that coalescence takes place. Coalescence is a very complex phenomena in which the thin film between bubbles first thins and then rapidly ruptures under the influence of Van der Waals forces [Mar69], [Lea04]. To study this phenomena in detail one needs to resolve the length and time scales more than is possible in the present code. Zheng *et al*[ZLAC05] have developed an adaptive volume remeshing method and have implemented level set techniques to study coalescence in a Newtonian fluid.

The series of shapes obtained here are very similar to the shapes obtained by Manga and Stone [MS93] for axisymmetric drops. Manga and Stone carried out boundary integral calculations and also conducted experiments using axisymmetric drops in an infinite medium. They showed that for drops with $\lambda \sim 1$ the tail is significant for $Bo > 10$. For lower values of λ the tail is observed at even smaller values of Bond number. The two-dimensional bubbles in a closed container studied here have shapes that are very similar.

The presence of a yield stress leads to bubble shapes that are quite different from the shapes observed for Newtonian fluids. Figure 4.10 shows the time sequence of two rising bubbles of the same size, with $Y_g = 0.15$ based

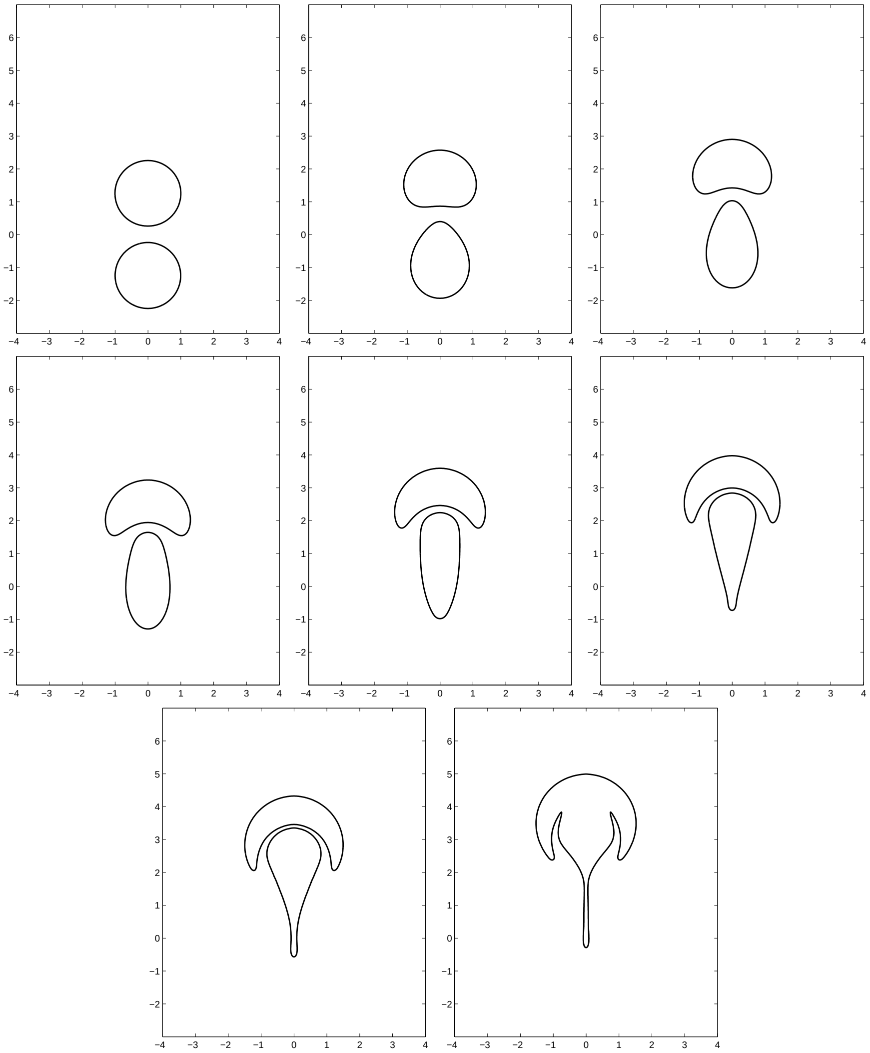

Figure 4.8: Evolution of the two collinearly rising bubbles in Newtonian fluid. $t = 0.1$, 5, 10, 15, 20, 25, 29.5 and 38.5. $\bar{t} = t/(\eta_p R/\sigma) = .001$, 0.05, 0.10, 0.15, 0.20, 0.25, 0.295 and 0.385. Bond number $Bo = 10$ and dimensionless yield stress $Y_g = 0$

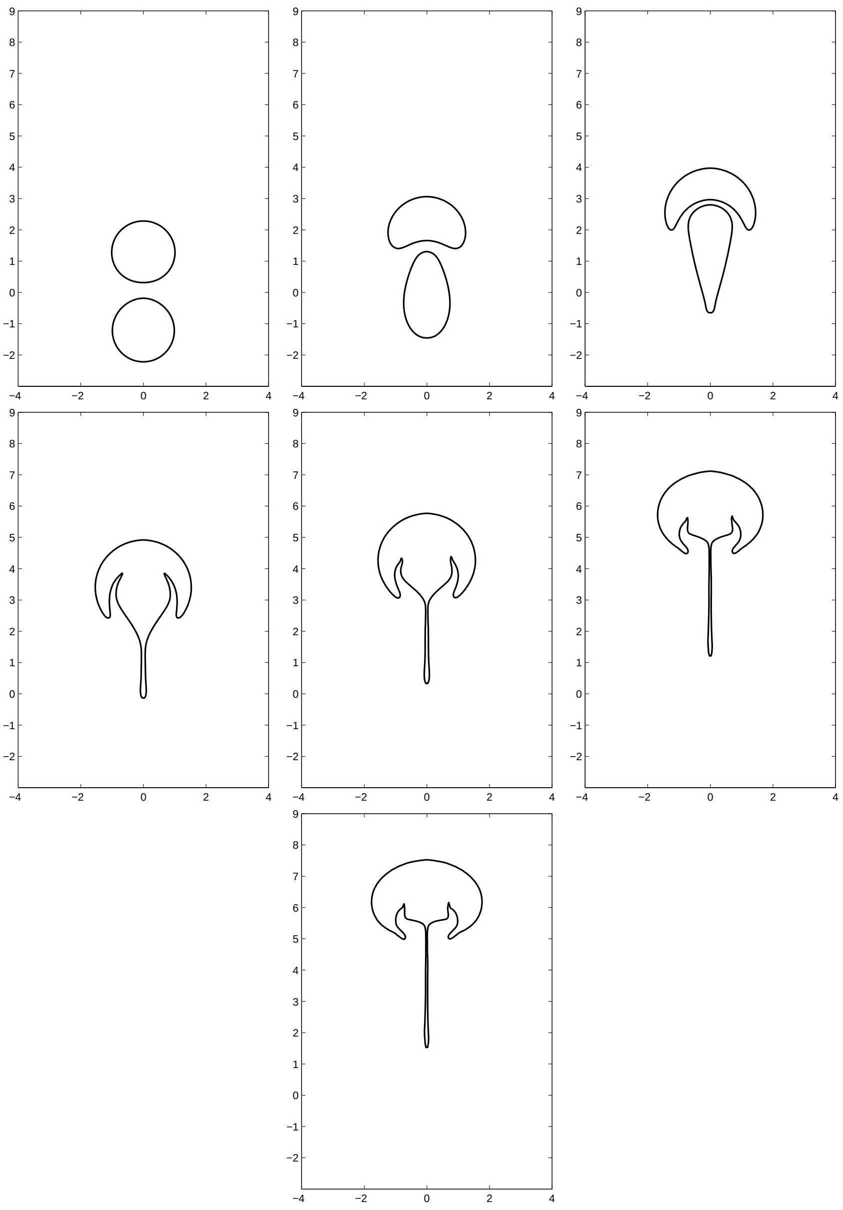

Figure 4.9: Evolution of the two collinearly rising bubbles in Newtonian fluid. t = 0.5, 12.5, 25, 37.5, 50, 75, and 85. $\bar{t} = t/(\eta_p R/\sigma)$ = .025, 0.625, 1.25, 1.875, 2.5, 3.75 and 4.25. Bond number $Bo = 2$ and dimensionless yield stress $Y_g = 0$

on a single bubble, $Bo = 10$ and $\lambda = 0.01$. The trailing bubble, starting from a circular cross-section, first takes a shape of a teardrop, followed by a transition to a "peanut" shape. It then takes on a parachute shape very similar to the Newtonian case, but with a wider tail. The leading drop behaves in a similar manner to the Newtonian case and takes on a crescent shape that forms an envelope above the top of the trailing drop. Ultimately, the simulations predict coalescence similar to the rising bubbles in a Newtonian fluid. The gray regions depict the unyielded regions near the bubble interface.

Figure 4.11 shows the time evolution of two collinearly rising bubbles in a yield stress fluid under conditions in which a single bubble cannot rise alone ($Y_g > Y_g^*$). The unyielded region near the bubble interface is shown in gray. Here, $Bn = 2.67$ based on the initial separation and $Ca = 1.88$ for each bubble, based on the initial rise velocity of the bubbles. The Bond number, $Bo = \Delta \rho g R^2/\sigma$, is equal to 10. These shapes are reminiscent of the droplet shapes in a yield stress fluid reported by Potapov [PSLN06].

In both these cases (Figure 4.10 and 4.11) the unyielded ears start as symmetric rotating regions. As the bubbles evolve, these regions break up into separate regions attached to each bubble. The transition takes place at a later stage for the higher yield stress fluid compared to the case with the lower yield stress.

The peanut shape adopted by the trailing drop can be explained by the fact that the two solid rotating regions on the sides of bubble act like a pair of tongs. As the bubbles rise, these solid regions are simultaneously stretching the leading bubble and pinching the trailing bubble at its mid-point. There

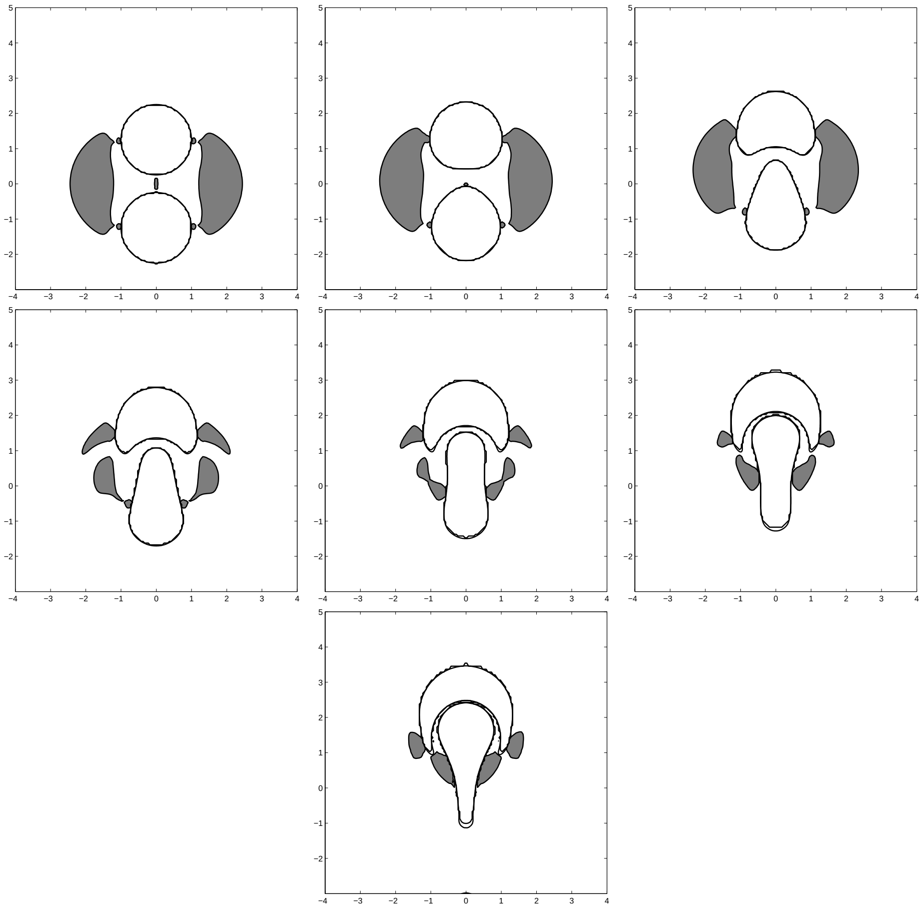

Figure 4.10: Evolution of two rising collinear bubbles at yield stress = 0.015. t = 0.1, 5, 25, 35, 45, 55, 64. $\bar{t} = t/(\eta_p R/\sigma)$ = .001, 0.05, 0.25, 0.35, 0.45, 0.55 and 0.64. Bond number $Bo = 10$ and dimensionless yield stress based on the bubble radius $Y_g = 0.15$. Bingham number at time zero $Bn = 0.82$

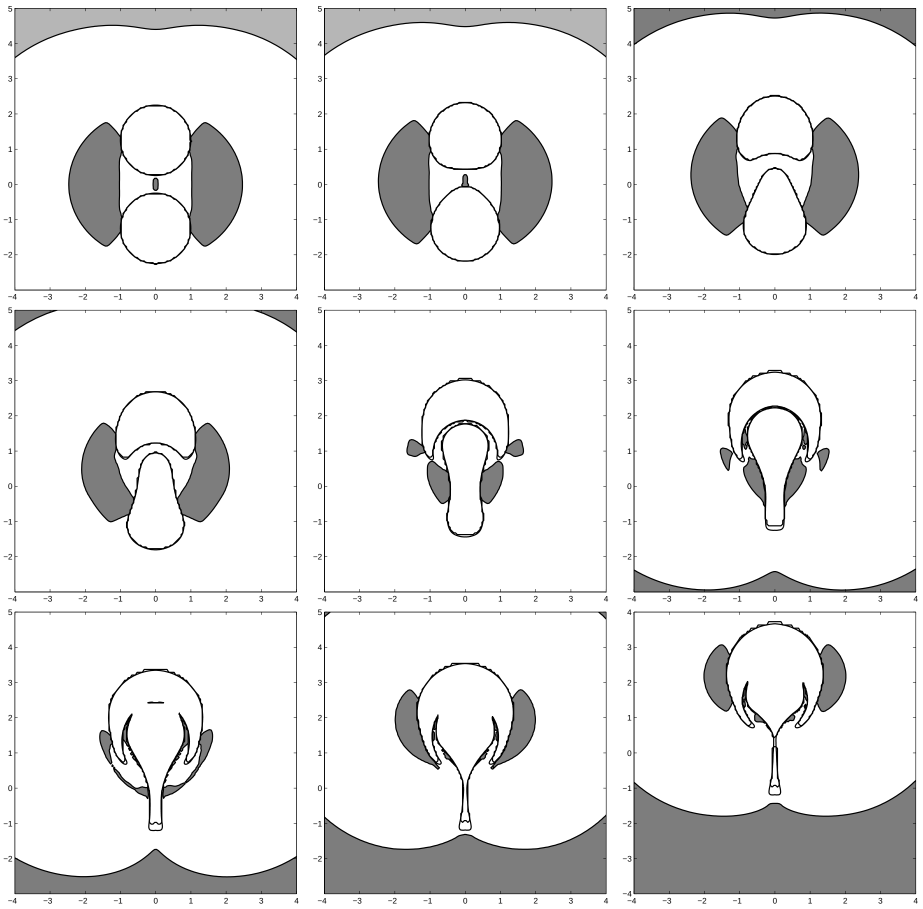

Figure 4.11: Evolution of the two collinearly rising bubbles. The gray regions represents unyielded domains and white regions are yielded. Bold and dark lines are the yield surface. Note how the trailing bubble takes a shape of a tear drop and the leading bubble becomes crescent shaped. A single bubble under these conditions will not be able to rise. $t = 0.1$, 10, 35.5, 55, 80.0, 93.5, 101.5, 120.5 and 134.5. $\bar{t} = t/(\eta_p R/\sigma) = .001$, 0.1, 0.355, 0.55, 0.80, 0.935, 1.015, 1.20 and 1.34. Bond number $Bo = 10$ and dimensionless yield stress $Y_g = 0.2$, Bingham number at time zero $Bn = 2.25$

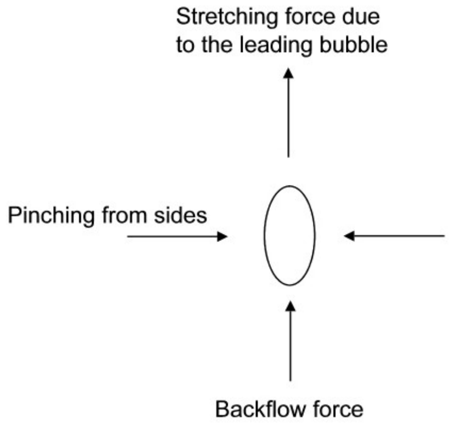

Figure 4.12: The schematic of the forces acting on the trailing bubble that can lead to a “peanut” shape.

are three “forces” that are acting on the trailing bubble (Figure 4.12): It is being stretched in the y-direction due to the leading bubble, it feels a “pinching” force due to the solid rotating region and a “flattening” force from the bottom due to the backflow. The net effect of these force gives the trailing bubble a peanut shape.

4.3.4 Effect of interfacial tension

Interfacial tension is expected to play a large role in the evolution of the shape of the bubbles. Figures 4.11 and 4.13 show the evolution of bubbles ($\lambda = 0.01$) at $Bo = 10$ and 2, respectively. $Y_g = 0.2$ for both the cases. The initial evolution of the bubbles in both figures is very similar. Starting from circular cross-section, the trailing bubble attains the shape of a “teardrop” and then it becomes a "peanut" in shape. Beyond this the trailing bubble at the lower Bond number starts to develop a cavity giving it a shape similar to a "fishtail" (Figure 4.13), whereas no such shape is observed at the higher Bond number (Figure 4.11). Development of a cavity or a "fishtail" shape is also observed for two collinearly falling drops ($\lambda = 1$). Figures 4.14 and 4.15 show the evolution of drops of unequal size at $Bo = 10$ and 1 respectively. The radius of the larger drop is twice that of the smaller one. $Y_g = 0.1$ for both cases. At lower Bond numbers the trailing bubble attains a "pacman" shape due to the development of the cavity. In comparison, none of the Newtonian calculations show the splitting in the tail of the trailing bubble or drop.

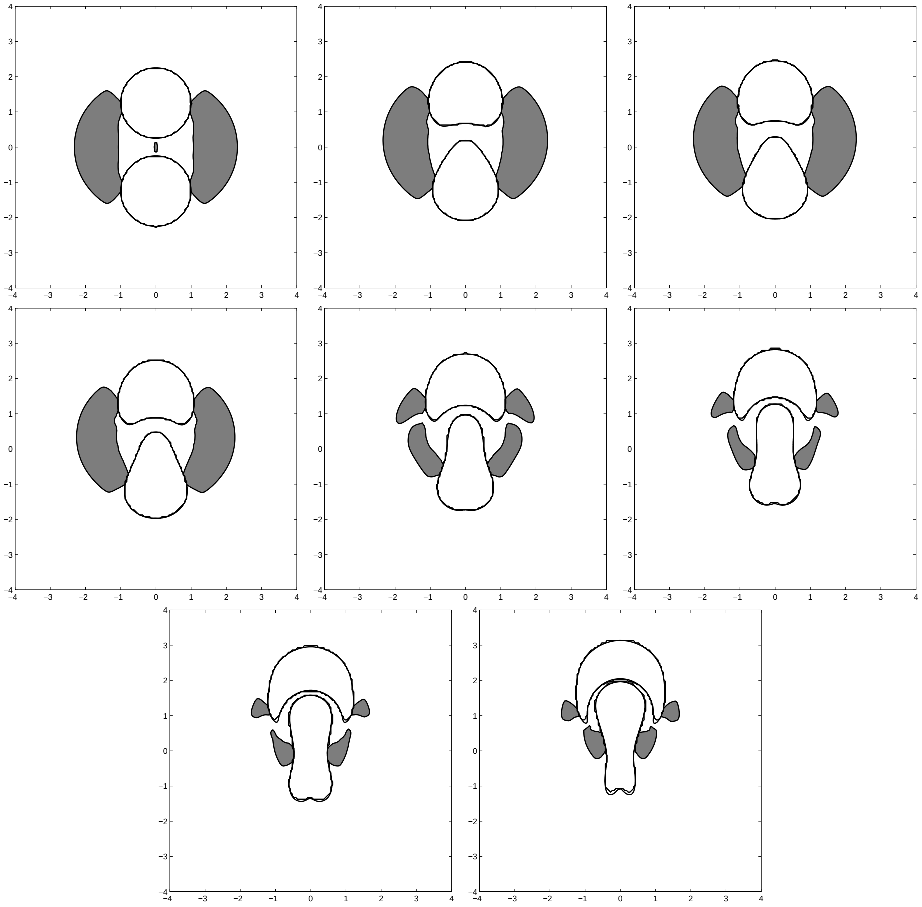

Figure 4.13: Evolution of rising collinear bubbles at $Y_g = 0.2$, Bo=2, $\lambda = 0.01$. The frames are at time $t = 0.1$, 25, 30.5, 40.0, 60.0, 70.0, 79.5 and 90.0. $\bar{t} = t/(\eta_p R/\sigma) = 0.005$, 1.25, 1.502, 2.00, 3.0, 3.5, 3.975 and 4.5. $Bn = 2.23$

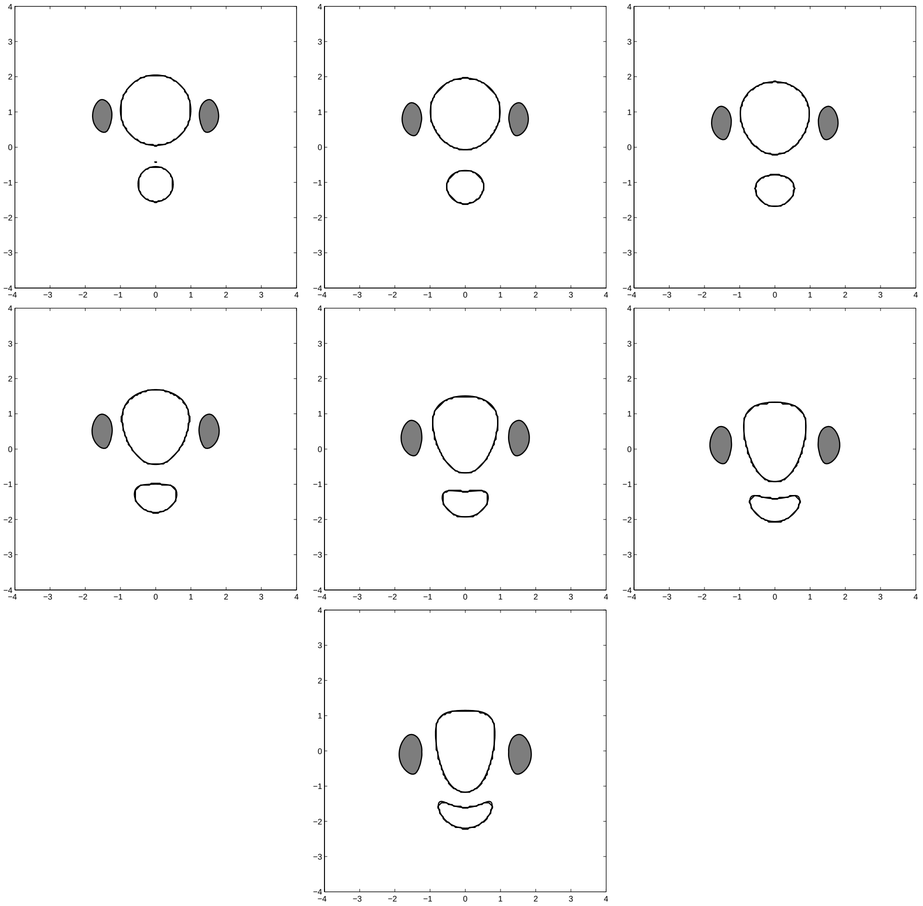

Figure 4.14: Two drops of unequal size falling under gravity. $Bo = 10$, $Y_g = 0.1$, $Bn = 1.2$; $\bar{t} = 0.001$, 0.11, 0.23, 0.43, 0.63, 0.83, 1.03

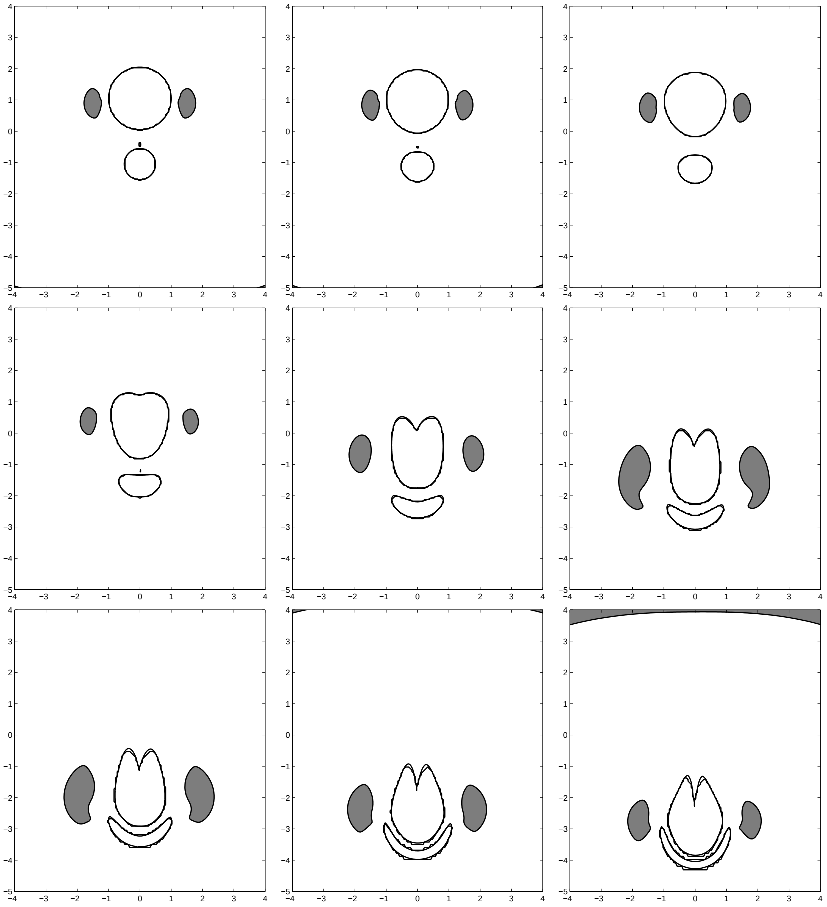

Figure 4.15: Two drops of unequal size falling under gravity. $Bo = 1$, $Y_g = 0.1$, $Bn = 1.22$ $\bar{t} = 0.01$, 1.0, 2.00,3.05, 4.3, 5.0, 6.00, 6.80, 7.40

The presence of similar cusps in two dimensional systems has previously been reported (see Joseph *et al* [JNRR91] and Jeong and Moffat [JM92]). Joseph *et al* conducted an experiment in which they kept two cylinders just below the free surface in a fluid. They observed the development of cusps on the free surface when both the cylinders rotated in a certain direction.

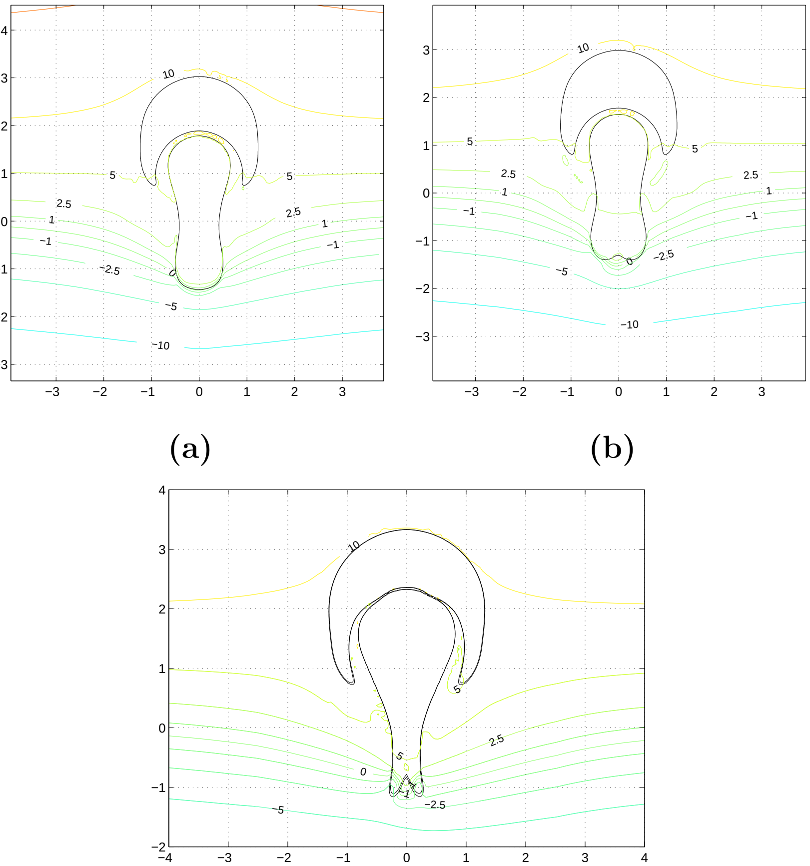

(a) **(b)**

(c)

Figure 4.16: Pressure contours for various cases; (a) $Bo = 10$, $Y_g = 0.2$, $\bar{t} = 0.815$; (b) $Bo = 2$, $Y_g = 0.2$, $\bar{t} = 4.05$; (c) $Bo = 2$, $Y_g = 0.2$, $\bar{t} = 5.10$.

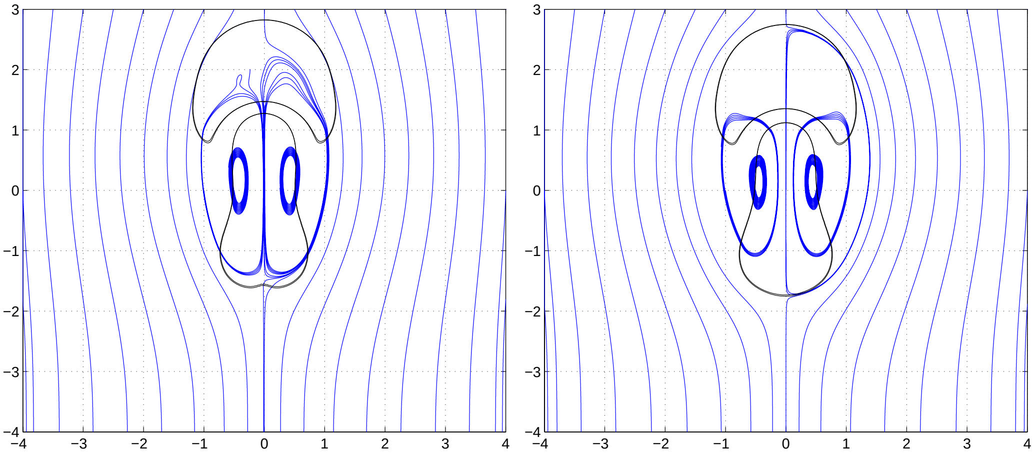

Figure 4.17: Streamlines to explain the reason behind the cusp. Left figure is at $Bo = 2$ and right figure is at $Bo = 10$.

Jeong and Moffat explained the formation of cusps by a presence of a single dipole below a straight horizontal free surface. Such a dipole then gives rise to circular motion of the fluid in the phase in which it is present, and beyond a critical capillary number, a cusp is obtained.

Similar arguments can be used for the two bubbles studied here. Figure 4.17 shows the streamlines for two different cases: $Bo = 2$, which shows the development of a fishtail, and $Bo = 10$, which does not show the fishtail. The two figures are chosen at times that visually depict similar shapes of the bubbles. The streamlines are relative to a frame of reference attached to the trailing end of the bottom bubble. It is evident that two re-circulating regions develop that are very similar to the ones obtained by Jeong and Moffat. At the higher Bond number, the size of the recirculation region is bigger than at the lower Bond number. At the higher Bond number, the streamlines that are not part of the recirculation zone never cross the bubble interface, whereas, at the lower Bond number the streamlines from the non-recirculating zone cross the leading bubble. It indicates that the distance between the top edge of the leading bubble and the bottom edge of the trailing bubble is decreasing with time only at the lower Bond number, which manifests in the development of the cavity. The streamlines show the mechanism of how the cavity develops, but do not provide the answer to the question as to why the streamlines at the higher Bond number are different from the ones at the lower Bond number.

Another relevant fact that should be considered here is that the spherical shape is a stable solution to the problem of a single falling drop in an otherwise quiescent fluid. This means that for small shape perturbations at finite Ca the drop will tend to become spherical again (see Kojima *et. al.* [KHA84], and Pozrikidis [Poz90]). Under finite deformations, however, the shape can become unstable and lead to long tails for prolate drops and cavities for oblate drops [KL89] even for finite Bond numbers. In addition, the instability is limited to the rear part of the translating drop; the front of the drop tends to remain spherical in both the cases. Here, the trailing drop is deformed under the influence of the leading drop. For the drops rising in a Newtonian fluid, the trailing drop tends to become prolate and thus becomes unstable and forms a long tail. For the bubbles rising in a yield stress fluid, the development of the tail is hindered due to the backflow. If the backflow is strong enough, the bottom of the trailing bubble will flatten, giving it characteristics very similar to the bottom of an oblate drop and, possibly, developing a cavity.

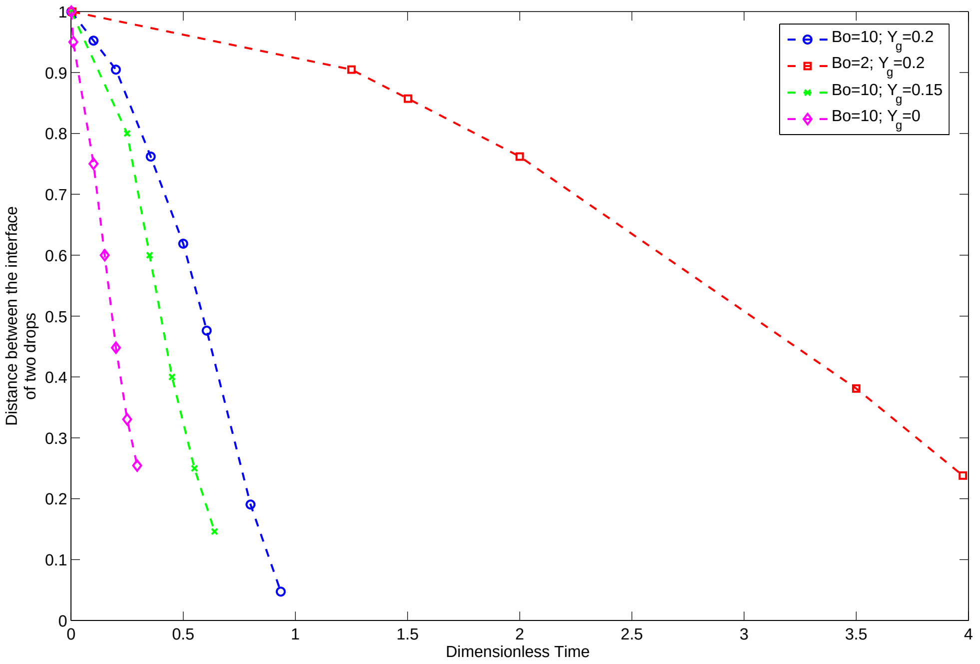

Figure 4.18: Distance between the interface of two bubbles on the y-axis. Dimensionless time is defined as $\bar{t} = t/(\eta_p R/\sigma)$.

Figure 4.18 shows the distance between the surfaces of two bubbles on the y-axis with time for different sets of parameters. The distance between the bubbles is normalized by the initial distance. The bubbles in a Newtonian fluid take the least time to approach and coalesce. As the yield stress is increased, it becomes harder for the bubbles to move, hence they take longer to come closer. Decreasing the Bond number also has a similar effect of increasing the time of approach of the bubbles.

4.4 Side-by-side configuration

4.4.1 Yield surfaces and unyielded regions

Now consider bubbles that are initially in a side-by-side configuration, as shown in Figure 4.19. The effect of yield stress on the yield surfaces can be seen in Figure 4.20 for the bubbles with an initial distance between the centers equal to $D = 2.5R$. Here, Y_g based on one bubble is equal to 0.1, 0.15, 0.16, 0.175. The critical values Y_g^* for one bubble is 0.167. The gray regions depict the unyielded domains. Similar to a rising single bubble in a yield stress fluid, an outer unyielded region is obtained and rotating "ears" are observed on the equator. The region between the bubbles around the equator is also unyielded, especially at the higher values of Y_g. At $Y_g = 0.1$ two unyielded islands are also observed on the y-axis. Figure 4.21 shows the streamlines at $Y_g = 0.1$ in the laboratory frame of reference. There are four recirculation regions in total; two corresponding to each bubble. Bubbles lie in each others' backflow regions, which hinders the rise of each bubble. The Bingham number, which is inversely proportional to the rise velocity, equals 15.1 for each bubble in the bubble pair at $Y_g = 0.1$, while the Bingham number for a single rising bubble under the same conditions is $Bn = 13.4$. This is in contrast to the case of collinearly rising bubbles, which interact in a way that facilitates motion.

At $Y_g = 0.175$ the "outer" unyielded region is attached to the bubble surfaces. Outer halves of the bubbles are in unyielded regions and the inner halves are exposed to the yielded regions. There is an unyielded region on

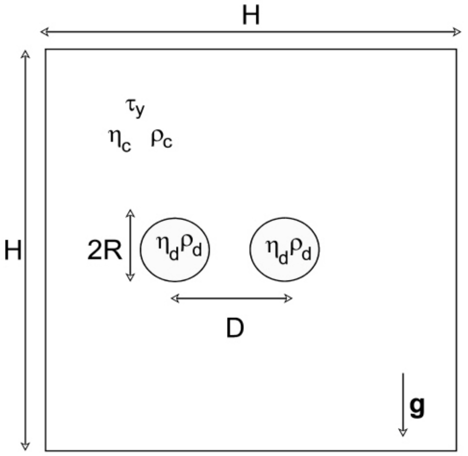

Figure 4.19: Schematic of the initial configuration and physical parameters for side-by-side rising bubbles.

the equator joining the two bubbles. Streamlines for $Y_g = 0.175$ are shown in Figure 4.22. Contours of the magnitude of the velocity for $Y_g = 0.175$ are also shown in the same figure. The velocity magnitude outside the yielded region is almost zero everywhere, indicating that the streamlines in this region are only due to the regularization of the Bingham model. Figure 4.23 shows the time evolution of the bubbles at $Y_g = 0.17$; there is no upward motion, but the calculation does show some rotational motion and the resulting shape change of the bubbles.

Figure 4.24 shows the unyielded regions for two rising bubbles of the same size as a function of the distance between them ($Y_g = 0.15$). The Bingham number as a function of distance is non-monotonic in the sense

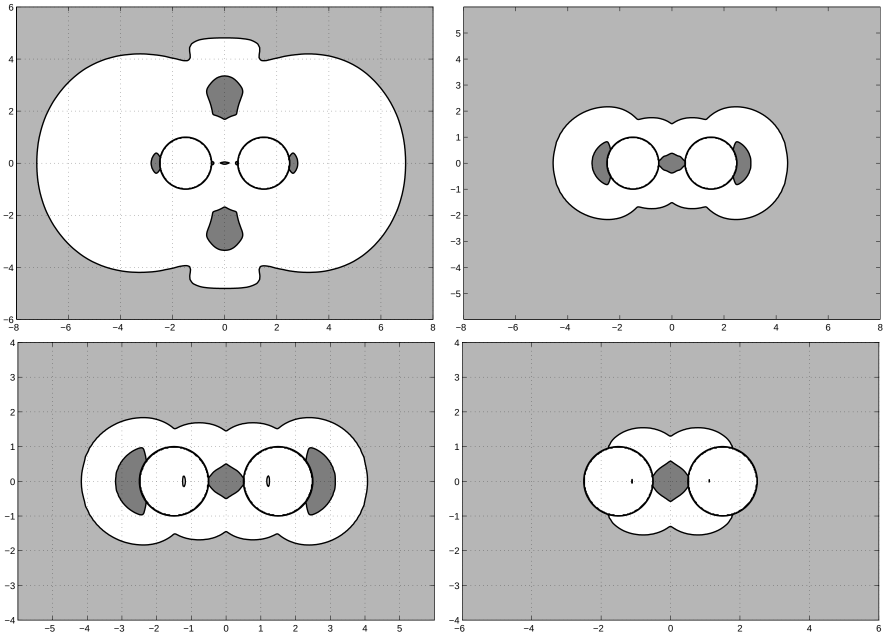

Figure 4.20: Effect of the yield stress. $Y_g = 0.1$, 0.15, 0.16, 0.175. $Bn = 1.73$, 13.52, 31.55, 104.69 A single bubble stops rising at ${Y_g}^* = 0.167$

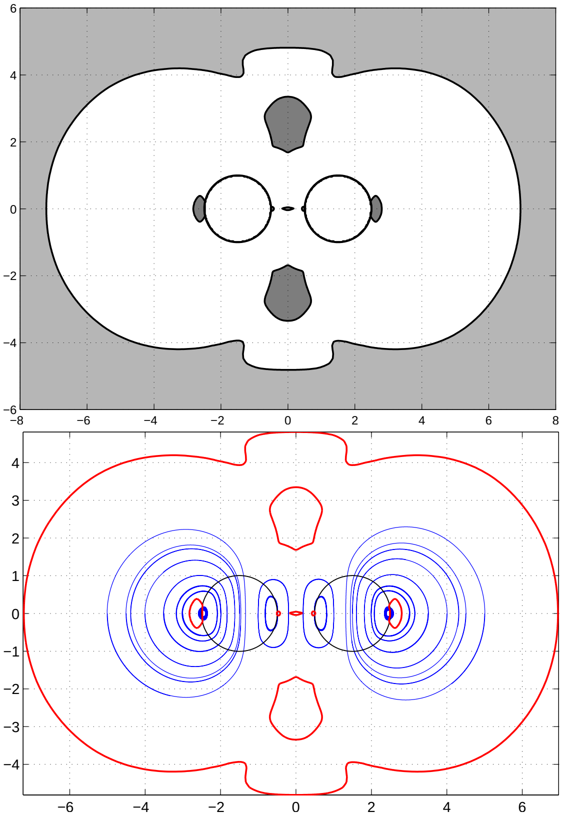

Figure 4.21: Streamlines for $Y_g = 0.1$ at $t = 0$.

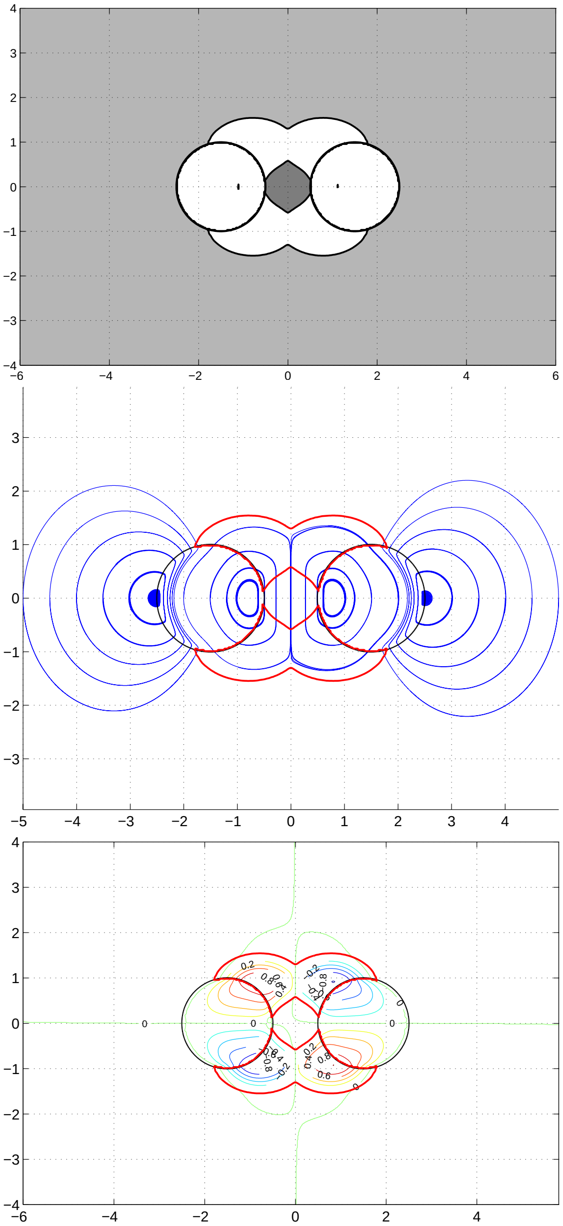

Figure 4.22: Streamlines for $Y_g = 0.175$ and velocity magnitude contours. The bubbles are not actually rising, but only rotating.

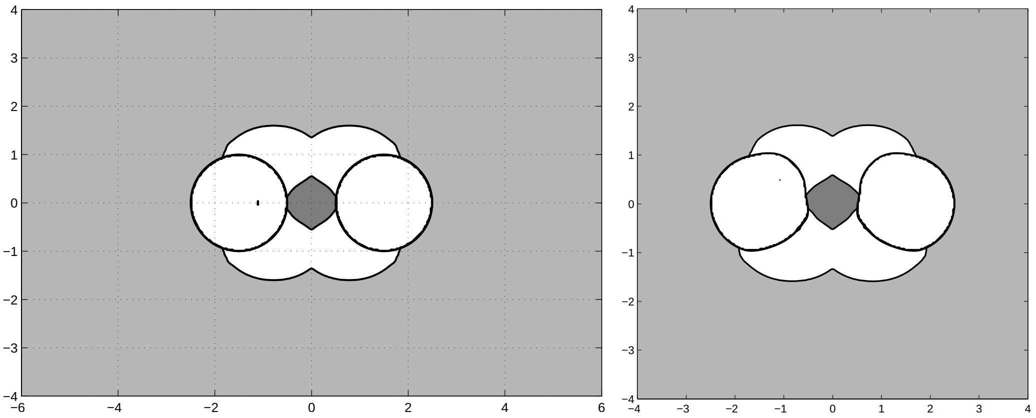

Figure 4.23: Evolution of two SBS bubble when $Y_g = 0.17$. The second picture is at $t = 237.5$. Bubbles are deforming while rotating but not rising!

that it first decreases from 15.06 at a distance of $D = 3R$ to $Bn = 8.67$ at a distance of $D = 6R$ and then it increases back to $Bn = 13.77$ at $D = 8R$. In comparison, $Bn = 13.39$ for a single bubble rising alone, which is very close to the value obtained at $D = 8R$. Thus, it can be concluded that at that distance the bubbles no longer feel the effect of each other. When the bubbles are very close to each other, they hinder each others rise, causing the Bingham number to be higher than for a single bubble case. It is not clear why the Bingham number should drop below the value of a single bubble as the distance between the bubbles is increased.

The critical yield stress for a single bubble rising in a yield stress fluid is $Y_g^* = 0.167$ [See chapter 3]. In the collinear configuration Y_g^* depends on the distance between the bubbles; the smaller the distance, the higher the critical yield stress. For $D \geq 8R$, the critical yield stress is the same as for

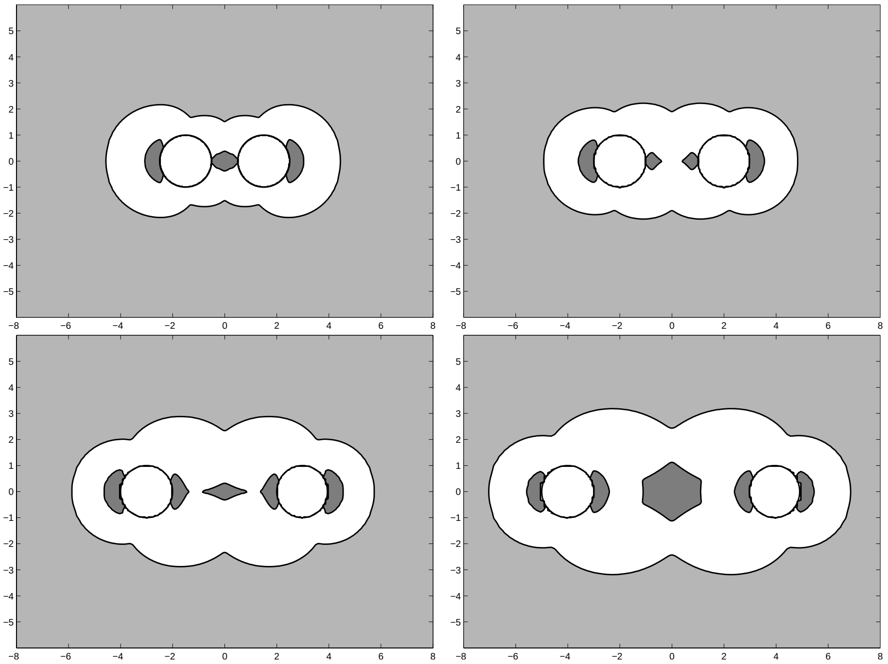

Figure 4.24: Effect of distance. $Y_g = 0.15$, $D/R = 0.3$, 0.4, 0.6, 0.8. $Bn =$ 15.06, 9.67, 8.67, 13.77. In comparison the Bingham number obtained for a single rising bubble under the same conditions is $Bn = 13.39$.

the single bubble (refer to Figure 4.4); at $D = 6R$ and $2.5R$ the critical yield stress equals $Y_g^* = 0.20$ and 0.30, respectively. In the SBS configuration, the bubbles are unable to rise for values of the yield stress beyond the critical yield stress for a single bubble.

Merkak [MJM06] conducted experiments with two interacting spheres and observed that in SBS configuration the presence of a sphere has little effect on drag experienced by the other sphere. Our observation that two bubbles cannot rise together even if they are very close together ($D \sim 2.5R$) is consistent with their experimental observation.

This observed difference between collinear and SBS configurations can be attributed to the fact that in the collinear case the stresses due to the lower bubble act normal to the upper bubble, thus enhancing the total stress exerted by the bubbles on the fluid. In the SBS configuration the bubbles lie in each other's back flow region, and thus are unable to help each other to rise.

In Figure 4.25, the evolution of two bubbles in the SBS configuration with $D = 2.1R$ is shown; $Y_g = 0.1$, $Bo = \infty$ and $Bn = 1.08$. The bubbles rise together, and the solution always remains symmetric about the y-axis (as expected). Also, the bubbles move away from each other as they rise. This lateral motion is very similar to the case of a bubble in a Newtonian fluid rising near a vertical wall [TTMM02].

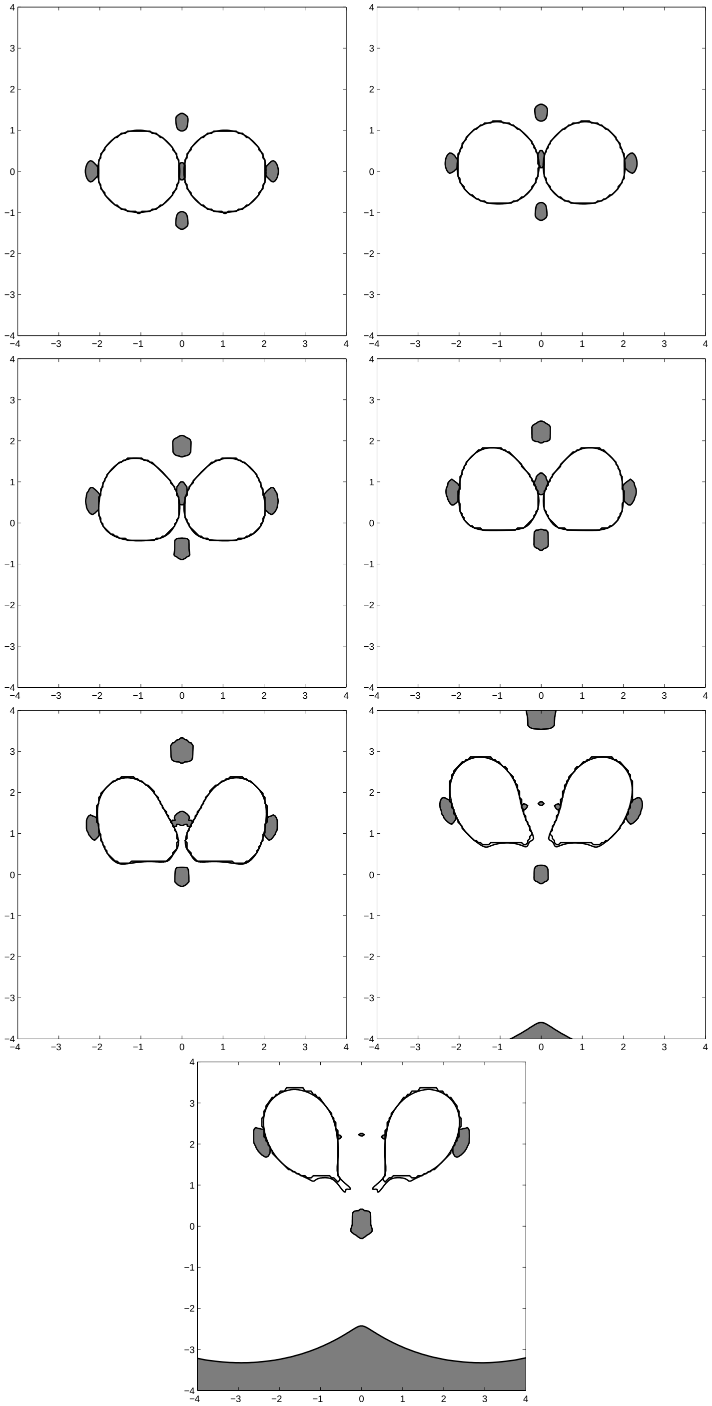

Figure 4.25: Evolution of side-by-side bubbles. $Y_g = 0.1$. $Bn = 1.086$. $Bo = \infty$ $t = 0.1$, 20, 49, 74, 124, 174 and 224. A single bubble stops rising at ${Y_g}^* = 0.167$

4.4.2 Entrapment of smaller bubble

If two different sized bubbles are used, the smaller bubble may become trapped while the bigger one can rise. Figure 4.26 shows such a case ($Y_g = 0.1$, based on the larger bubble; $D = 3R$). The Bingham number obtained is $Bn = 1.96$ (for a single larger bubble, $Bn = 1.38$). Under these conditions, the larger bubble alone can rise, but the smaller bubble cannot rise alone. Here, the smaller bubble sits on the edge of the yielded region around the larger bubble. The streamlines are also depicted in Figure 4.26.

Another case in shown in Figure 4.27, where the distance between the bubbles is reduced to $D = 2.5R$. Here, the smaller bubble sits completely in the yielded region of the larger bubble. Interestingly, two additional unyielded regions are observed around the smaller bubble, which look like the blades of a fan. Figure 4.28 shows the time evolution of this case. Note that the smaller bubble is not rising, but only deforming, whereas the larger one is deforming as well as rising. The unyielded region around the smaller bubble is starting to merge with the outer unyielded region, indicating that if the simulation proceeds the larger bubble will rise alone, leaving the deformed smaller bubble behind.

4.5 Off-center bubbles

Until now this chapter has explored collinear or SBS bubbles. In realistic emulsions most of the interactions between the bubbles or droplets will deviate from such ideal initial configurations. This section will explore the initial

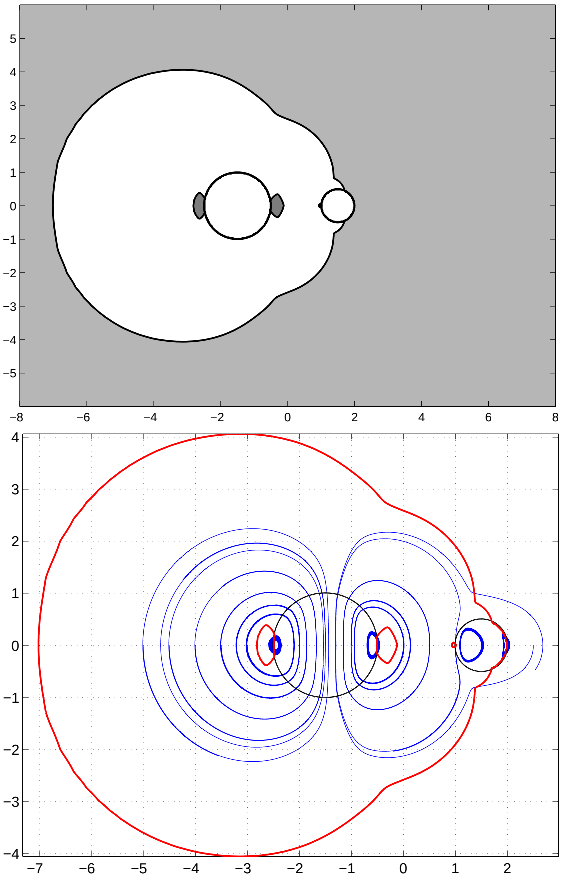

Figure 4.26: The smaller bubble alone cannot rise and the bigger alone can rise. $Y_g = 0.1$, $Bn = 1.96$, $D = 3R$

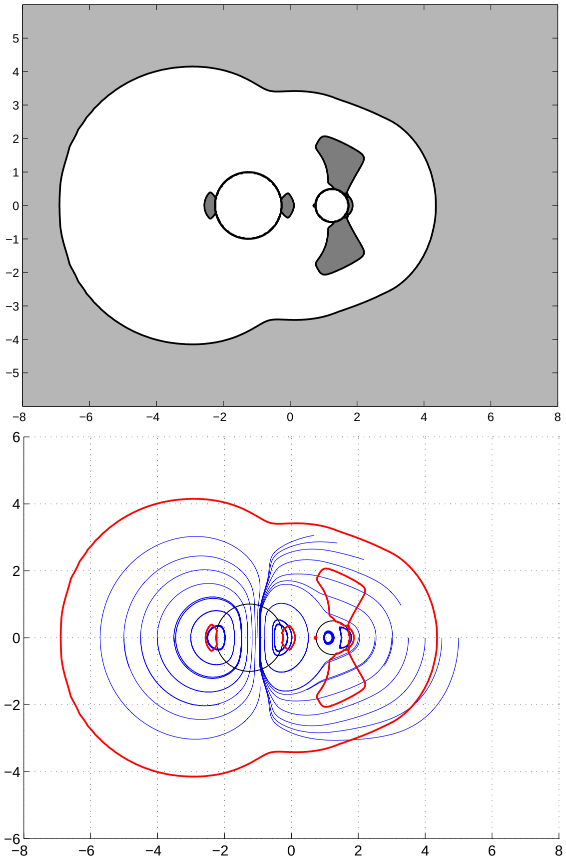

Figure 4.27: The smaller bubble alone cannot rise and the bigger alone can rise. $Y_g = 0.1,\ Bn = 2.06,\ D = 2.5R$

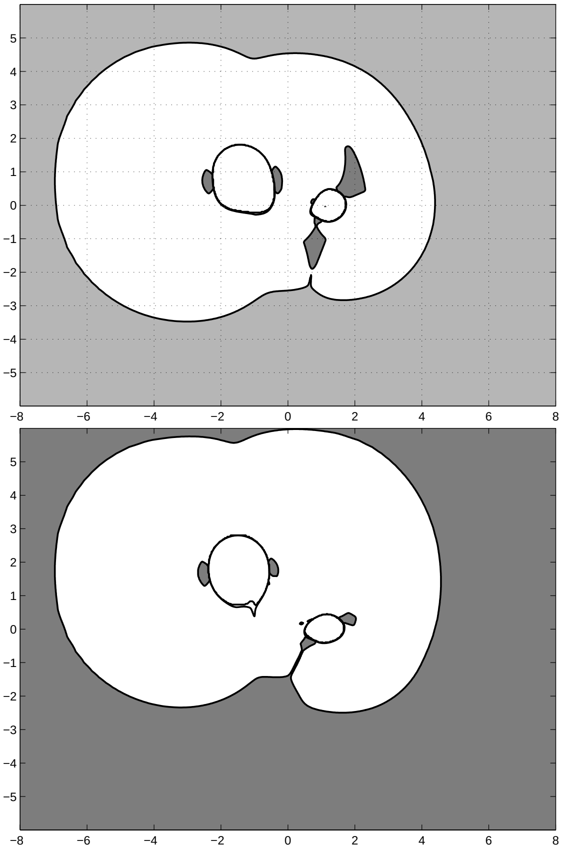

Figure 4.28: Evolution showing the entrapment of the smaller bubble. Frames after $t = 111$ and 218.5; $\bar{t} = 1.11$, 2.18; $Y_g = 0.1$, $Bo = 10$.

configurations in which the bubbles are not aligned but are off-center to start with. Manga and Stone [MS93] have shown that off-center drops in a Newtonian fluid display a rich variety of results. They showed that if the drops are off-center to start with and the leading drop is larger then the trailing drop will tend to align with the larger rising drop. They observed that this phenomenon can lead to higher efficiency of coalescence in an emulsion. If the smaller drop is leading, then the larger trailing drop will catch up with the smaller drop and, depending on physical conditions, will either coalesce or by-pass the smaller drop. If by-pass happens then the smaller drop is pulled to the wake of the bigger drop and there is again a tendency to align and coalesce. Figures 4.29 and 4.30 show the results for evolution of rising off-center bubbles when the larger bubble is leading and trailing, respectively.

Figures 4.31 and 4.32 show the evolution of bubbles for $Y_g = 0.1$ and $Y_g = 0.15$, respectively, for “off-center” bubbles. Under these conditions the smaller bubble will not rise alone and the critical yield stress for the larger bubble alone is $Y_g^* = 0.167$. The line joining the centers of the bubbles makes an angle of 45 degrees with the horizontal and the initial distance between the centers is $D = 2.45R$. The smaller bubble lies in the yielded region of the larger bubble and two recirculating unyielded regions on the equator of the larger bubble are observed. As the bubbles evolve with time, the trailing smaller bubble is stretched and then is pulled towards the wake of the larger leading bubble. This pull is due to the deformation of the bubbles, as shown by Manga and Stone [MS93] for the drops in a Newtonian fluid. At $Y_g = 0.1$ (Figure 4.31) the trailing bubble develops a thin tail very similar to the tail of

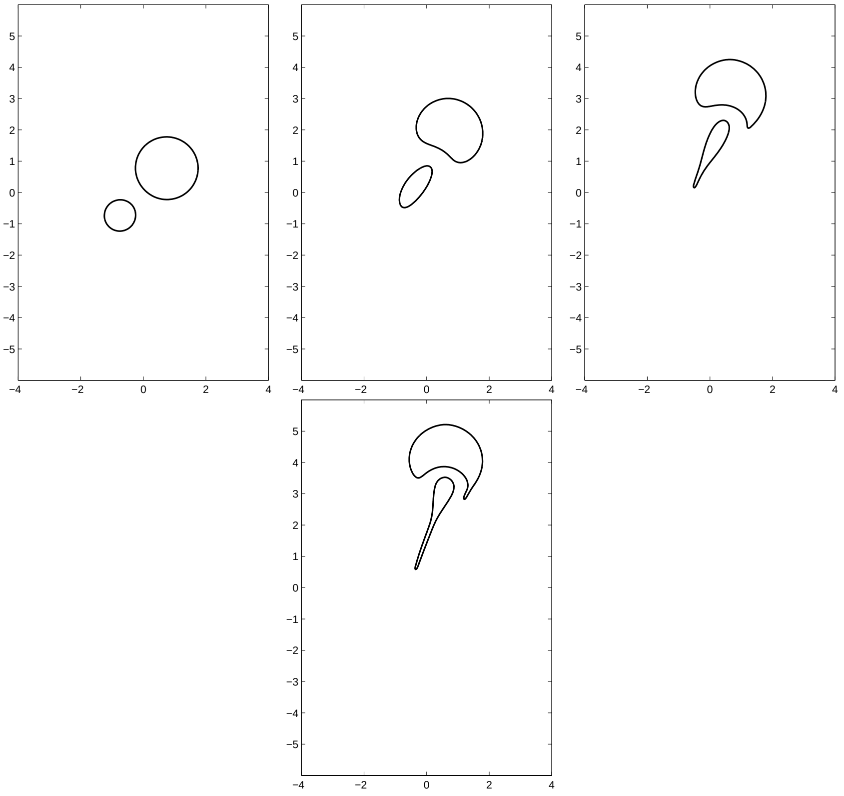

Figure 4.29: Bubbles 45 degrees off center line; larger bubble leading. Image after $t = 0.5,\ 25.0,\ 50.0,\ 70.0$; $\bar{t} = 0.005,\ 0.25,\ 0.50,\ 0.70$. $Y_g = 0$, $Bo = 10$, (based on larger bubble)

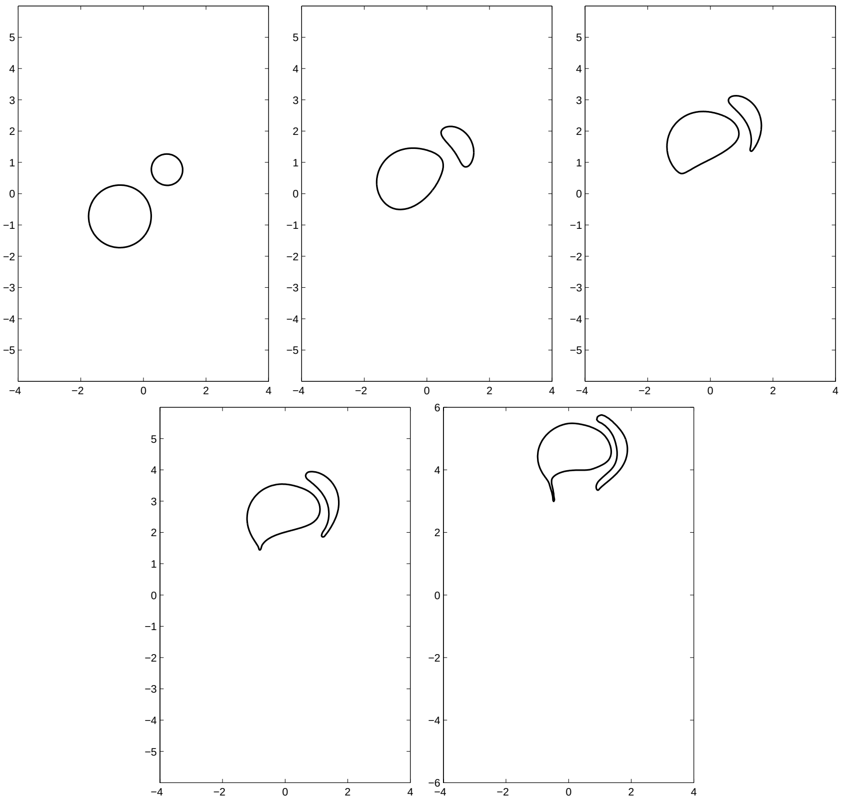

Figure 4.30: Bubbles 45 degrees off center line; larger bubble trailing. Image after $t = 0.5$, 25.0, 50.0, 70.0, 115.0; $\bar{t} = 0.005$, 0.25, 0.50, 0.70, 1.15. $Y_g = 0$, $Bo = 10$, (based on larger bubble)

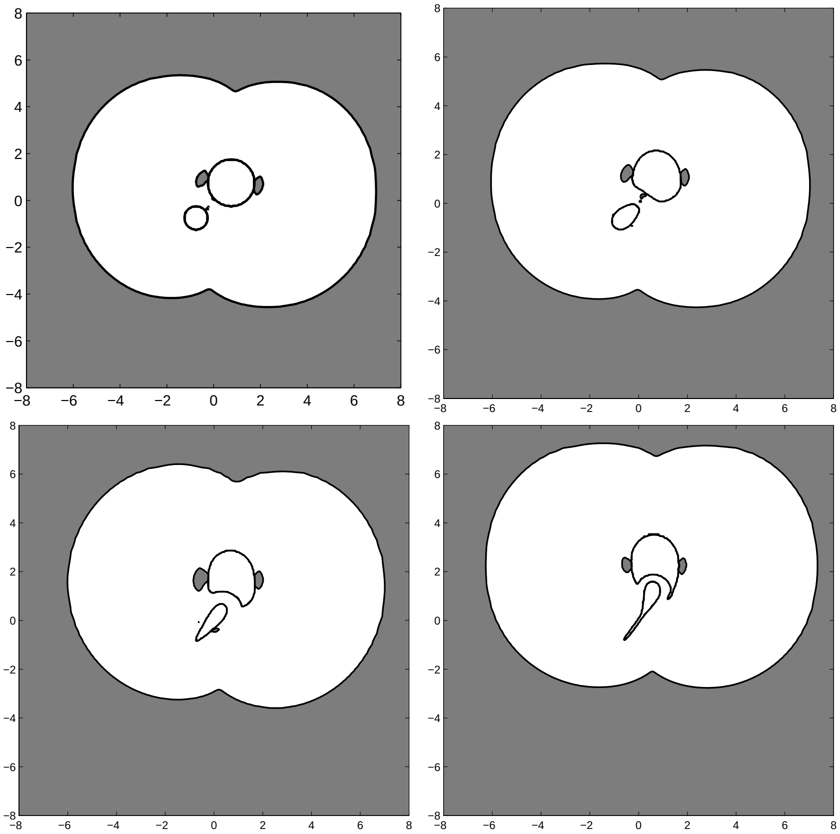

Figure 4.31: Bubbles 45 degrees off center line. Image after $t = 0.1$, 40, 98.5, and 183.5; $\bar{t} = 0.001$, 0.40, 0.98 and 1.83. $Y_g = 0.10$, $Bo = 10$, $Bn = 1.08$ (based on larger bubble; Bingham number estimated at time $\bar{t} = 0.001$ and is based on velocity of center of mass of bubbles.)

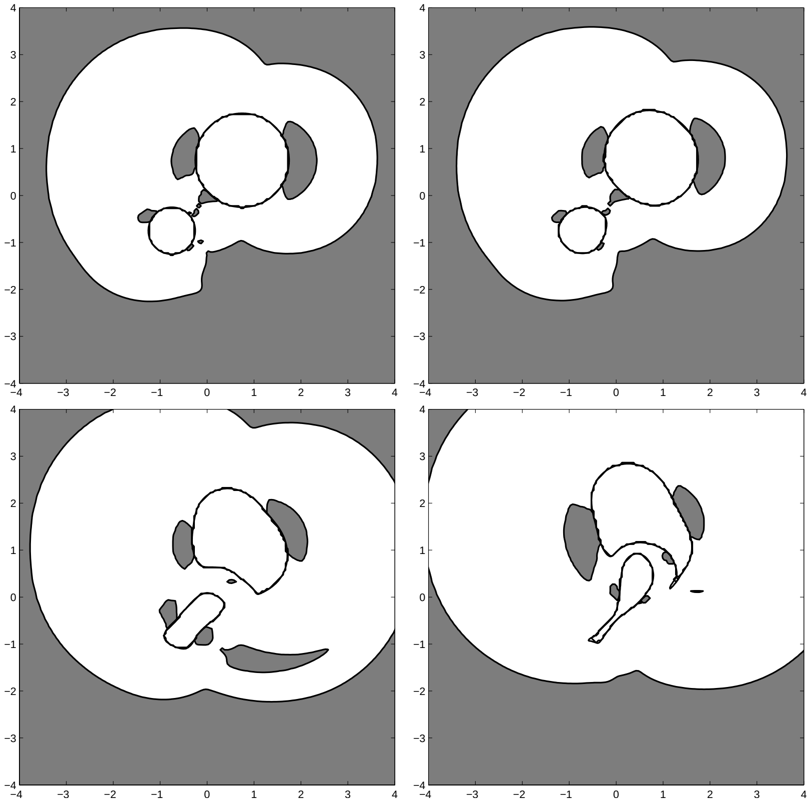

Figure 4.32: Bubbles 45 degrees off center line. Image after $t = 0.1$, 30, 170.4 and 311.5; $\bar{t} = 0.001$, 0.30, 1.70 . $Y_g = 0.15$, $Bo = 10$, (based on larger bubble), $Bn = 10.17$

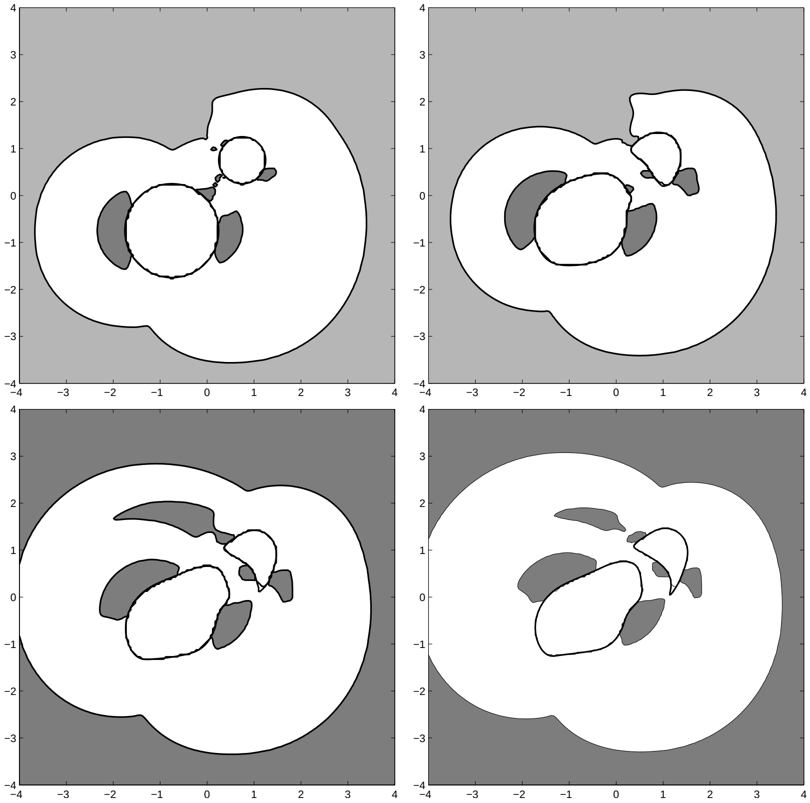

Figure 4.33: Bubbles 45 degrees off center line. Image after t = 0.5, 147.5, 252.5, 297.5; $\bar{t}$ = 0.005, 1.475, 2.52, 2.97. Y_g = 0.15, Bo = 10, (based on larger bubble); $Bn = 11.89$

the trailing bubble for collinearly rising bubbles in a Newtonian fluid. As the yield stress in increased to $Y_g = 0.15$ (see Figure 4.32), the tail is suppressed due to the backflow and a thick small tail is observed. As the bubbles rise and deform, the smaller trailing bubble catches up with the larger leading bubble and the chances of coalescence increase.

Figure 4.33 shows the evolution of off-center bubbles when the smaller bubble is leading; $Y_g = 0.15$, $Bn = 9.0$, and $Bo = 10$.

4.6 Coordinated motion: Three bubbles

In the previous sections, the motion of two interacting bubbles in a Bingham fluid has been explored. In this section we will extend the study to three interacting bubbles. We will concentrate on three initial configurations of bubbles: collinear, upward pointing equilateral triangle (UPET) and downward pointing equilateral triangle (DPET).

Figure 4.34 shows the yield surfaces for three collinearly rising bubbles with a distance $D = 2.5R$ between centers. For the images shown in the figure, the dimensionless yield stress Y_g equals 0.3, 0.35 and 0.4, respectively. There is an outer unyielded region and there are two large rotating ears on the sides, very similar to two collinearly rising bubbles. At these physical conditions, the critical yield stress for two collinear bubbles is $Y_g^* \sim 0.3$. As the yield stress is increased the rotating ears become bigger and the outer yield surface approaches closer to them.

Figures 4.35 and 4.36 show the configurations and the yield surfaces for

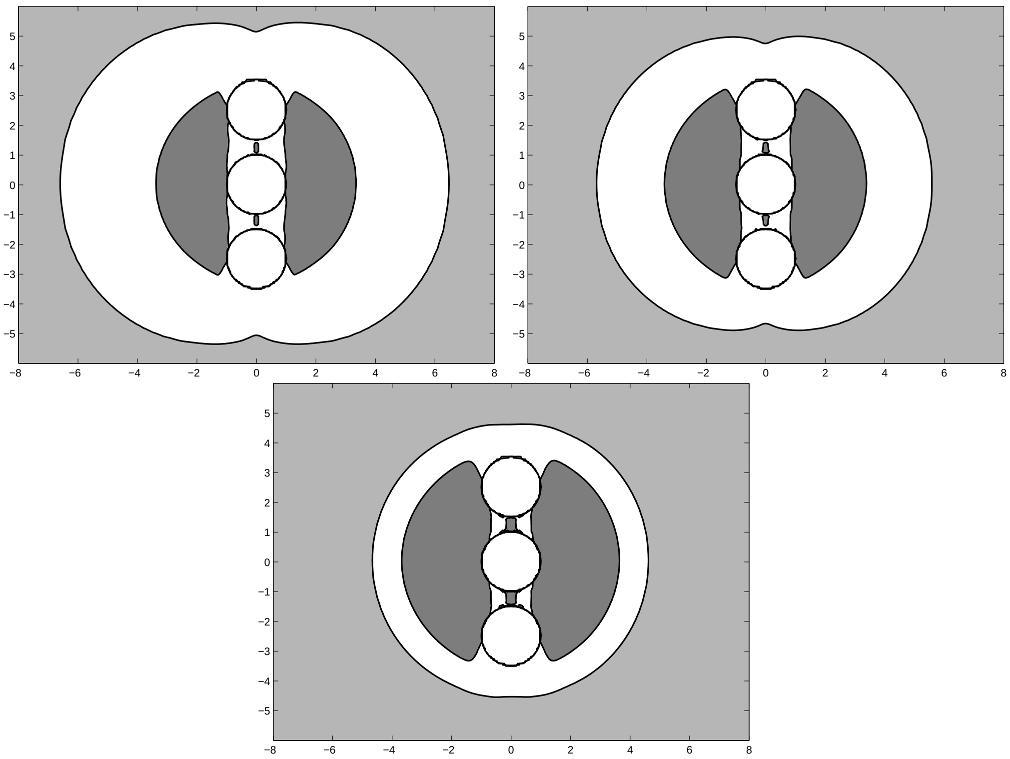

Figure 4.34: Effect of yield stress; three bubbles in collinear configuration; $Y_g = 0.3$, 0.35 and 0.4; $Bn = 3.21$, 8.25 and 44.66; $Bo = 10$

the bubbles in downward and upward pointing equilateral triangles, respectively. Two bubbles are horizontally aligned and the third bubble is either at the top (UPET) or at the bottom (DPET). The distance between the centers of the bubbles is $D = 2.5R$. In the following text, horizontally aligned bubbles will be called HABs and the third bubble will be called TB.

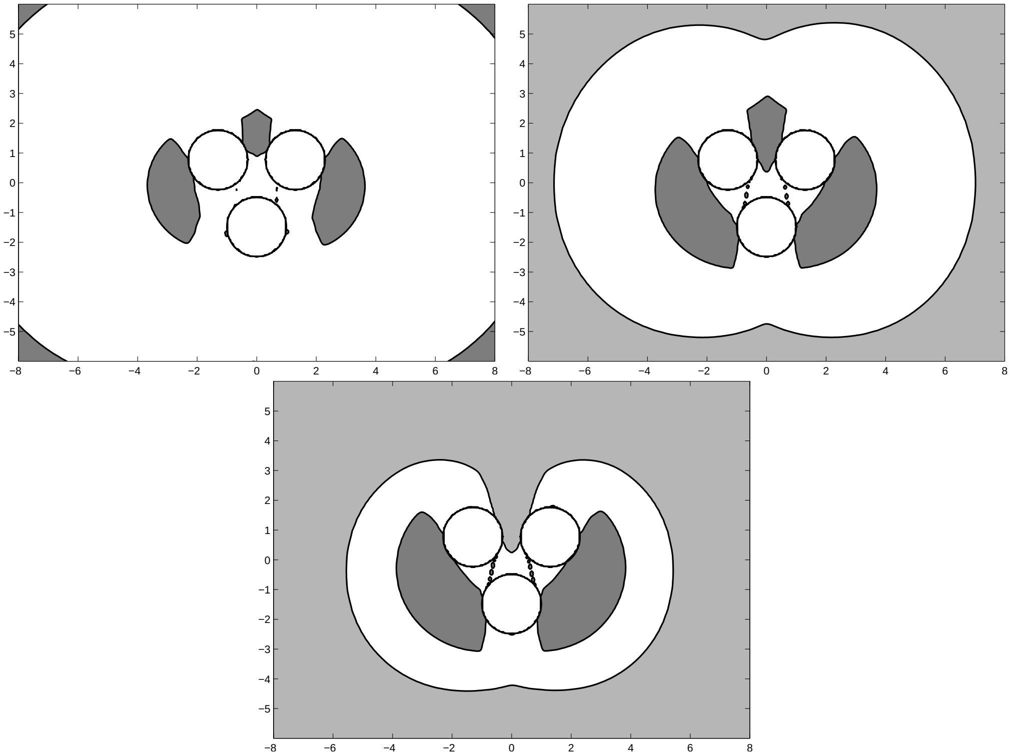

Figure 4.35: Effect of yield stress; three rising bubbles in DPET configuration; $Y_g = 0.15$, 0.2, and 0.225; $Bn = 1.3$, 6.1 and 24.86; $Bo = 10$

The yield surfaces for UPET and DPET are almost mirror images of each other, and the Bingham number observed at each yield stress for both

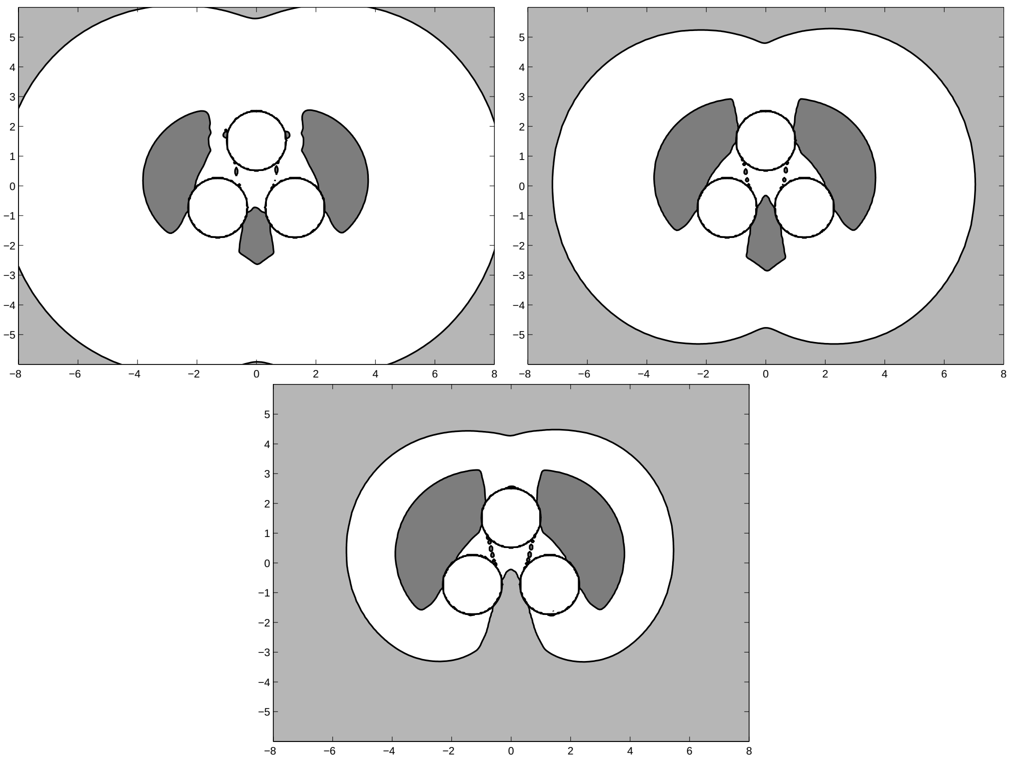

Figure 4.36: Effect of yield stress; three rising bubbles in UPET configuration; $Y_g = 0.175$, 0.2, and 0.225; $Bn = 2.33$, 6.1, and 25.4; $Bo = 10$

configurations is very similar. For a dimensionless yield stress Y_g of less than 0.225 the outer yielded surface is detached from the bubble surfaces, while HABs are connected to each other via an unyielded region between them. There are large unyielded recirculating regions (ears) on each side of the three bubbles. These regions are attached to the outside of HABs, while they attach to the TB only at higher values of the yield stress ($Y_g \geq 0.2$). At $Y_g \geq 0.225$ the outer unyielded region merges with the unyielded region between HABs. On increasing the yield stress further, the rotating ears become larger and then, ultimately merge with the outer unyielded region. At such a yield stress the bubbles stop rising.

In Figure 4.37 the Bingham number as a function of the yield stress for different configurations is shown: single bubble (red open circles), two collinear bubbles (blue asterisks), two SBS bubbles (green diamonds), three collinear bubbles (black squares), and three up-equilateral bubbles or UPET (magenta triangles). The distance between the bubble pairs is $D = 2.5R$. The line corresponding to two SBS bubbles almost coincides with the single bubble case and has the same critical yield stress ($Y_g^* \sim 0.167$). The three collinear bubble configuration is the most effective in terms of overcoming the yield stress and has the highest critical yield stress (~ 0.425). For two collinear bubbles and the UPET configuration $Y_g^* = 0.3$ and 0.25, respectively. It is interesting to note that the two collinear bubbles have a higher value of Y_g^* than the UPET configuration. This observation might be explained by noting that for two bubbles, the collinear configuration is the most effective in overcoming the yield stress and SBS is the least effective way. Bubbles in

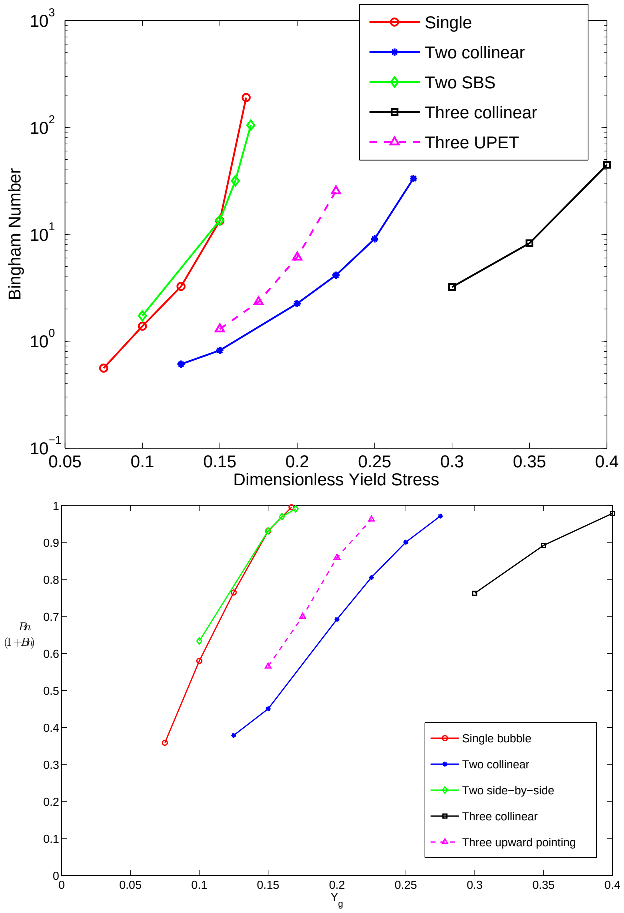

Figure 4.37: Bingham number and Modified Bingham number $Bn/(1 + Bn)$ as function of dimensionless yield stress for various configurations of bubbles: Single bubble (red open circles), two collinear bubbles (blue asterisks), two SBS bubbles (green diamonds), three collinear bubbles (black squares), and three up-equilateral bubbles or UPET (magenta triangles).

any other configuration are expected to have intermediate values of Y_g^*. In the UPET configuration, two of the bubbles are in SBS configuration and the third bubble is placed in a way that is intermediate between SBS and collinear to both the bubbles. Thus the overall configuration behaves as two bubbles with an intermediate configuration.

4.6.1 Evolution

Manga and Stone observed that the behavior of the cluster of drops in a Newtonian fluid can be explained by the interactions between pairs of drops [MS95]. Figures 4.38 and 4.39 show the evolution of three rising bubbles in a Newtonian fluid starting from UPET and DPET configurations, respectively. In the UPET configuration the top bubble flattens as it rises and then takes on a crescent shape very similar to the leading bubble in the two bubble configuration. The two trailing HABs are pulled to the wake of the top bubble and develop long tails. This observation is very similar to the alignment of bubbles obtained for two off-center bubbles (section 4.5).

Similarly, in the DPET configuration (Fig. 4.39) the top two bubbles pull the trailing bubble towards their wake. Under the force from both the leading bubbles the trailing bubble deforms and is stretched from the top. It then develops “two heads”, each being pulled towards one of the leading bubbles. The trailing bubble also develops a tail.

Figures 4.40 and 4.41 show the evolution of the bubbles rising in a Bingham fluid in the UPET and DPET configurations respectively. The dimensionless yield stress $Y_g = 0.15$ and the Bond number $Bo = 10$. The Bingham number, Bn at time $t = 0$ equals 1.29 and 1.09 for the UPET and the DPET configurations, respectively. In Figure 4.40 the frames shown correspond to the dimensionless time $\bar{t} = 0.001$, 0.115 and 0.675. In Figure 4.41 the frames are shown at time $\bar{t} = 0.001$, 0.15 and 0.775. The evolution of rising bubbles is similar to the Newtonian case with the difference being that the trailing bubble is flat at its bottom. This might be attributed to the backflow due to the finite yielded region around the bubbles, as in the case of two collinear bubbles.

4.7 Conclusions

In this chapter, the evolution of two and three bubbles starting from various configurations has been explored. It is found that two or three bubbles can rise together under conditions where a single bubble may not be able to rise. The configuration of bubbles plays a major role in determining the critical yield stress. A collinear configuration is the most effective in overcoming the yield stress and a side-by-side configuration the least effective, with an off center configuration being intermediate.

The shape evolution of bubbles in a yield stress fluid is found to be quite different from the Newtonian case. Two bubbles, starting from circular shapes, deform and approach each other even if the bubbles are of the same size. The symmetry of the problem is lost as the leading bubble tends to become an oblate and trailing bubble tends to become a prolate. Under

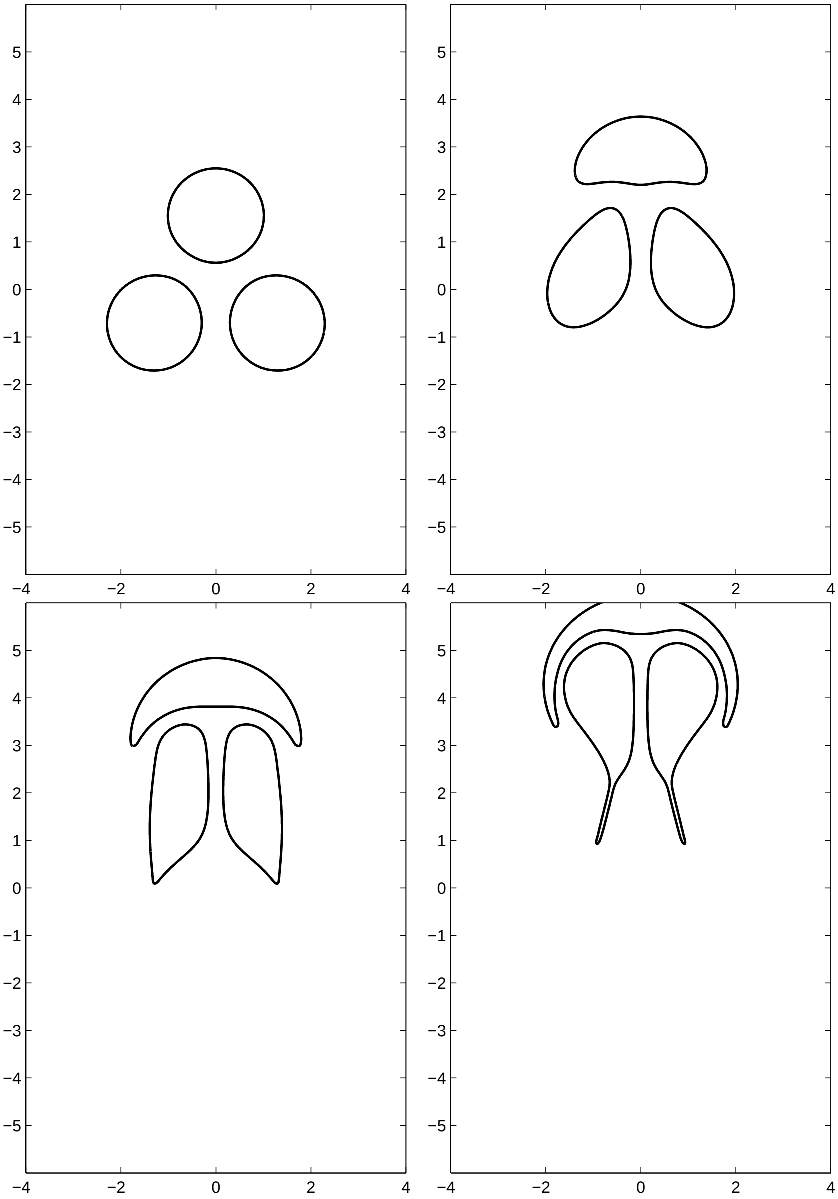

Figure 4.38: Evolution of three rising bubbles in the UPET configuration; $Y_g = 0$, $Bo = 10$; $\bar{t} = 0.005$, 0.15, 0.30 and 0.475

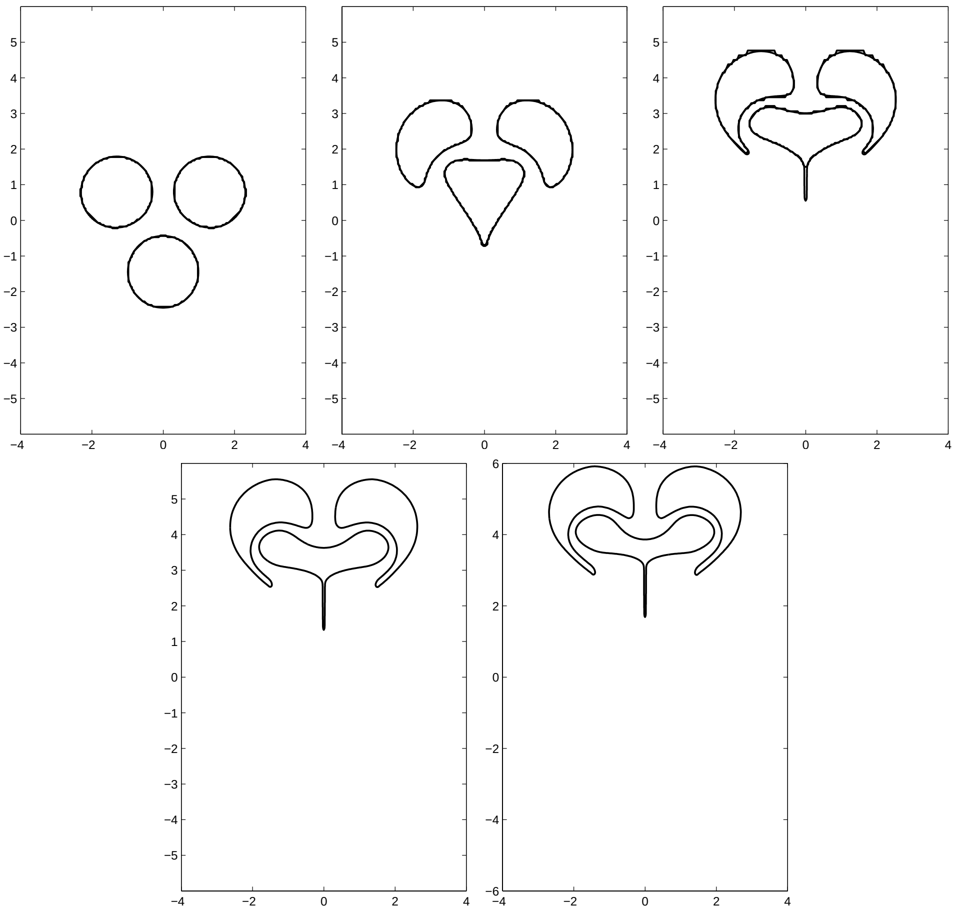

Figure 4.39: Evolution of three rising bubbles in the DPET configuration; $Y_g = 0$, $Bo = 10$; $\bar{t} = 0.005$, 0.25, 0.475, 0.625, 0.70

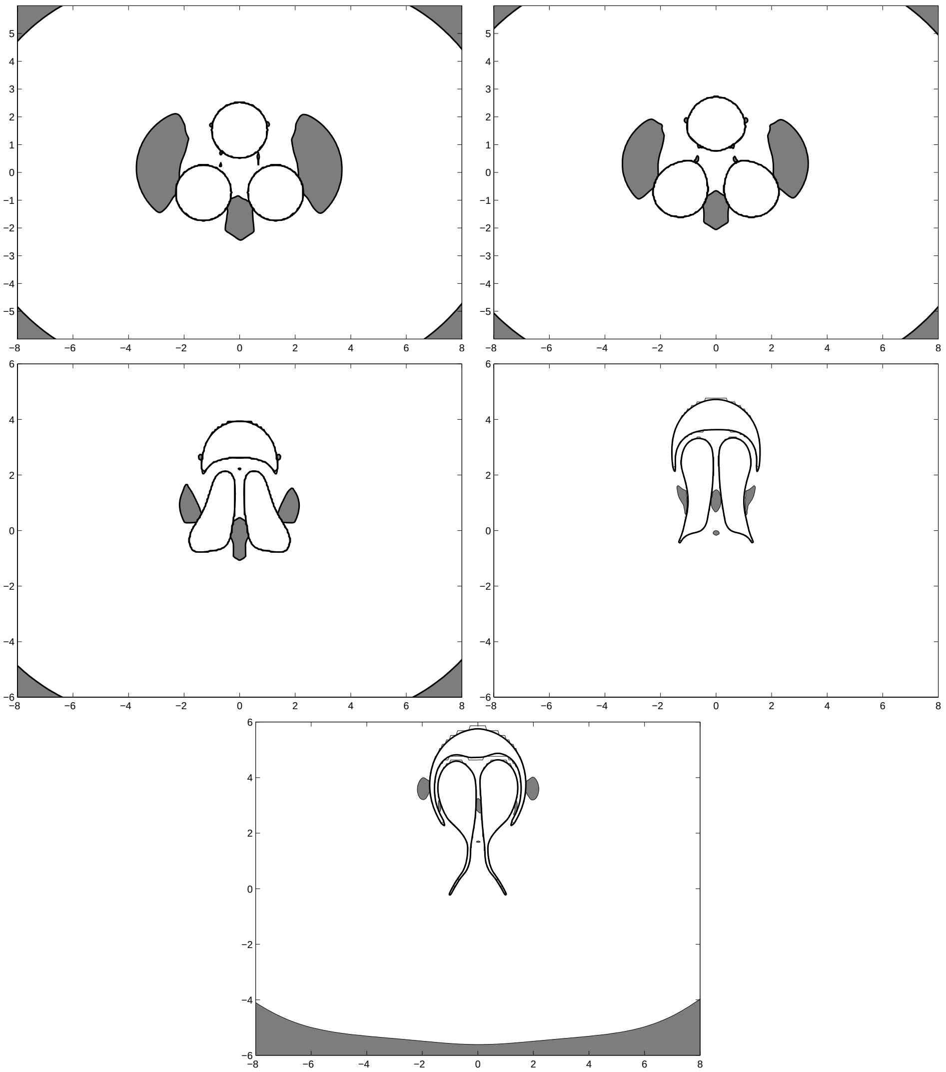

Figure 4.40: Evolution of three rising bubbles in the UPET configuration; $Y_g = 0.15$; $Bo = 10$; $Bn = 1.29$; $t = 0.1$, 11.5, 67.5, 90.0, 120.0; $\bar{t} = 0.001$, 0.115, 0.675, 0.90, 1.20

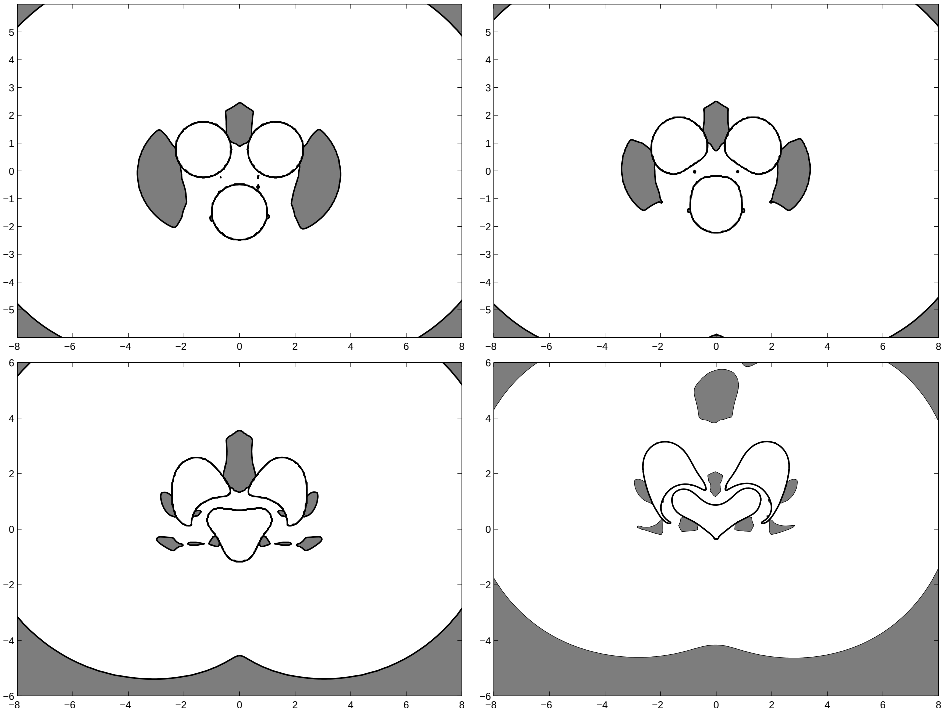

Figure 4.41: Evolution of three rising bubbles in the DPET configuration; $Y_g = 0.15$; $Bo = 10$; $Bn = 1.09$; $t = 0.1$, 15, 77.5, 140.0; $\bar{t} = 0.001$, 0.15, 0.775, 1.40

certain conditions the development of a cavity or fishtail is observed in the trailing bubble, the mechanism of which is still not well understood. The backflow due to the finite yielded region acts to flatten the bottom of the trailing bubble. It is known that oblate drops rising in a Newtonian fluid are unstable, developing a cavity on the bottom. Similarly, the flattening of a trailing bubble in a yield stress fluid gives it characteristics of an oblate and then a cavity or a fishtail structure may develop. This flattening of the trailing bubbles is also observed for the three rising bubbles in DPET or UPET configuration.

For the bubbles which are off-center to begin with, there is a tendency to align as they rise, increasing the coalescence efficiency in a bubbly fluid. Under the flow field of the leading bubble, the trailing bubble deforms and is pulled to the leading bubble‘s wake. The leading bubble, meanwhile, evolves from a circular shape to a crescent. The effect of yield stress is observed in flattening of the trailing edges of the bubbles.

As in Newtonian fluids, the behavior of three rising bubbles in a yield stress fluid can be understood by considering the pair interactions. In the UPET configuration the top bubble pull the HABs to its wake, very similar to the two interacting bubbles in an off-center configuration. The trailing bubbles are stretched in the direction of rising bubbles, they deform symmetrically and catch up with the leading bubble. In the DPET configuration both the top bubbles pull the trailing bubble to their wake. Under two forces from different directions the trailing bubble developes two heads. The overall evolution remains symmetric about the y-axis.

Chapter 5

Summary and future work

5.1 Summary

A finite element-based code using level-set methods has been successfully implemented to study the motion of two-dimensional bubbles and drops in a yield stress fluid. A regularized Bingham model was used for the yield stress fluid and converged results with respect to the regularization parameter were obtained. It was also confirmed that the results are converged with respect to the mesh density used and the flow is independent of the container walls.

A finite yielded region is obtained around a single rising bubble. Beyond a certain distance from the bubble the fluid remains unyielded. Due to the finiteness of the yielded domain, a region of back flow is required to conserve mass. In the yielded region near the bubble surface, two rotating unyielded "ears" are observed on the equatorial plane of the bubble. These rotating regions rise with the bubble, melting and reforming at the trailing and leading edge, respectively.

The configuration of bubbles plays a major role in determining the value of the critical yield stress. Two interacting bubbles can rise together even if a single bubble is not able to rise. A collinear configuration of bubbles is observed to be the most effective in overcoming the yield stress and a side-by-side configuration the least effective, with an off-center configuration intermediate. The critical yield stress obtained for a side-by-side configuration is similar to that of a single bubble.

The behavior of three interacting bubbles can be understood by considering each bubble pair. The critical yield stress for an upward pointing equilateral triangle (UPET) configuration is observed to be smaller than two collinear bubbles but greater than the side-by-side SBS configuration. This observation can be explained by noting that the two bubble on the bottom are horizontally aligned to each other, thus acting very similar to an SBS configuration. The top bubble is placed off-center from either of the bottom two bubbles, thus the top and bottom bubbles behave very similarly to two off-center bubbles. The net result of one SBS and two off-center interactions gives the UPET configuration a critical yield stress between that of the SBS and collinear configuration.

The shape evolution of rising bubbles is also studied. A single bubble in a Newtonian fluid remains spherical under creeping flow conditions. A bubble rising in a yield stress fluid is also expected to remain spherical (or circular for two-dimensions). Small deformations were observed in this study, but these can be attributed to accumulation of small errors inherent in any computational scheme.

Two collinear bubbles rising together lose fore-aft symmetry, the leading bubble tending to an oblate shape and the trailing bubble to a prolate shape. The shape evolution of the trailing bubble differs from that in a Newtonian fluid. The trailing bubble acquires a “peanut” shape, which is believed to be due to the back flow. At higher Bond numbers, it develops a fishtail or a cavity at the trailing edge. The leading bubble flattens and envelopes the top of the trailing bubble. Ultimately, the bubbles coalesce and form a “shade tree” structure that is very similar to the newtonian case but with smaller tail.

If the bubbles are initially off-center, there is a tendency for them to align as they rise and deform. Such an alignment can potentially increase the coalescence efficiency in a bubbly fluid.

Evolution of three interacting bubbles can be understood by considering the interaction of each bubble pair. In the UPET configuration the top bubble pulls both bottom bubbles in to its wake, similar to the behavior of two off-centered rising bubbles. In the DPET configuration the two top bubbles try to pull the bottom bubble in to their respective wakes, which can be explained by considering the off-center interaction between the top and bottom bubbles.

Backflow due to the finite yielded domain around the bubbles plays a large role in determining the critical yield stress as well as the evolution shapes of the bubbles. The trailing bubble in a Newtonian fluid develops a long tail. In a yield stress fluid, the tail is suppressed due to the backflow and may even give rise to a “fishtail” structure, as observed for collinearly rising bubbles.

5.2 Further suggestions

The following is a short list suggesting a few directions in which the current work can be further expanded.

- In this work, the Bingham model was chosen to explore the effect of a yield stress on the rising bubbles. The Bingham model lacks any description of kinetics of the transformation from unyeilded to yielded domains; i.e. there is no rate dependance for the material to transform from a yielded state to unyielded state. It is important to understand the mechanism of such a transformation, especially in order to study the unsteady flow behavior of yield stress fluids.
- There have been a few attempts in the literature trying to explain the presence of yield stress in particulate suspensions [KSBH97], but a more general framework describing the yield stress in other materials, such as block copolymers or even a binary mixture of Lennard-Jones fluid, is lacking.
- The Bingham model assumes that the fluid beyond the yield stress behaves as a shear thinning fluid with no elasticity. In reality, history effects have been shown to be very important in yield stress fluids [ACU90], [HSCC98]. The problems involving interacting bubbles are

inherently unsteady problems, as the bubble shapes evolve with time and elastic effects might be important. Thus, there is a need for a model which includes both yield stress and elasticity.

- Coalescence is a very complex physical phenomena that involves not only hydrodynamics but also very small scale, or Van der Walls forces. A detailed study of coalescence is needed for yield stress fluids that will also take in account the heterogeneities present in the yield stress fluid, which will be present in the thin liquid film prior to coalescence.

Bibliography

[AA74] B.E. Anshus and G. Astarita. Oscillations in a Bingham body. *AICHE J.*, 20:832, 1974. 4

[ACU90] D.D. Atapattu, R.P. Chhabra, and P.H.T. Uhlherr. Wall effect for spheres falling at small Reynolds number in a viscoplastic medium. *J. Non-Newtonian Fluid Mech.*, 38:31–42, 1990. 7, 31, 139

[ACU95] D.D. Atapattu, R.P. Chhabra, and P.H.T. Uhlherr. Creeping sphere motion in Hershel-Bulkley fluids: flow field and drag. *J. Non-Newtonian Fluid Mech.*, 59:245, 1995. 31

[AMB01] A.N. Alexandrou, T.M. McGilvreay, and G.R. Burgos. Steady HerschelBulkley fluid flow in three-dimensional expansions. *J. Non-Newtonian Fluid Mech.*, 100:77–96, 2001. 6

[AS67] R.W. Ansley and T.N. Smith. Motion of spherical particles in a Bingham plastic. *AICHE J.*, 13:1193, 1967. 30

[AY73] K. Adachi and N. Yoshioka. On creeping flow of a viscoplastic fluid past a circular cylinder. *Chem. Eng. Sci.*, 28:214–226, 1973. 6, 31, 72

[BA99] G.R. Burgos and A.N. Alexandrou. Flow development of Herschel-Bulkley fluids in a sudden three-dimensional square expansion. *J. Rheol.*, 43:485–498, 1999. 6

[Bar99] H.A. Barnes. The yield stress—a review or ‘$\pi\alpha\nu\tau\alpha\ \rho\epsilon\iota$’—everything flows? *J. Non-Newtonian Fluid Mech.*, 81:133–178, 1999. 5, 29

[Bat67] G.K. Batchelor. *Introduction to fluid mechanics.* Cambridge Mathematical Library, 1967. 33

[Bat95] Klaus-Jurgen Bathe. *Finite element procedures.* Prentice Hall, 2 edition, 1995. 10, 19

[BDY70] R.B. Bird, G.C. Dai, and B.J. Yarusso. The rheolgy and flow of viscoplastic materials. *Rev. Chem. Eng.*, 1:1982, 1-70. 1, 29

[BE80] M. Bercovier and M. Engelman. A finite-element method for incompressible non-Newtonian flows. *J. Comput. Phys.*, 36:313–326, 1980. 35

[Bin22] E.C. Bingham. *Fluidity and Plasticity.* McGraw-Hill, 1922. 3

[BL06] F. Baldessari and L.G. Leal. Effect of overall drop deformation on flow-induced coalescence at low capillary numbers. *Phys. Fluids*, 18:013602, 2006. 77

[BM97a] M. Beaulne and E. Mitsoulis. Creeping motion of a sphere in tubes filled with a Herschel-Bulkley fluid. *J. Non-Newtonian Fluid Mech.*, 72:55–77, 1997. 31

[BM97b] J. Blackery and E. Mitsoulis. Creeping motion of a sphere in tubes filled with a Bingham fluid. *J. Non-Newtonian Fluid Mech.*, 70:59–77, 1997. 32

[BMB78] S.M. Bhavaraju, R.A. Mashelkar, and W.H. Blanch. Bubble motion and mass transfer in non-Newtonian fluids: Part 1. single bubble in power-law and Bingham fluids. *AICHE J.*, 24:1063–1070, 1978. 32, 72

[BMJ03] B.D. De Besses, A. Magnin, and P. Jay. Viscoplastic flow around a cylinder in an infinite medium. *J. Non-Newtonian Fluid Mech.*, 115:27, 2003. 5, 31, 39, 56, 72

[BSL98] R.B. Bird, W.E. Stewart, and E.N. Lightfoot. *Transport Phenomena.* Wiley, 2 edition, 1998. 4

[BTAB85] A.N. Beris, J.A. Tsamopoulos, R.C. Armstrong, and R.A. Brown. Creeping motion of a sphere through a Bingham plastic. *J. Fluid Mech.*, 158:219–244, 1985. 5, 31, 35

[BW85] H.A. Barnes and K. Walters. The yield stress myth? *Rheol. Acta.*, 24:323–326, 1985. 5

[Chh93] R.P. Chhabra. *Bubbles, Drops and Particles in Non-Newtonian Fluids.* CRC Press: Boca Raton, FL, 1993. 30, 72, 78

[CHMO96] Y.C. Chang, T.Y. Hou, B. Merriman, and S. Osher. A level set formulation of eulerian interface capturing methods for incompressible fluid flow. *J. Comput. Phys.*, 124:449, 1996. 33, 34, 35

[DF04] N. Dubash and I.A. Frigaard. Conditions for static bubbles in visco-plastic fluids. *Phys. Fluids*, 16:4319–4330, 2004. 6, 32

[DSR89] R.H. Davis, J.A. Schonberg, and J.M. Rallison. The lubrication force between two viscous drops. *Phys. Fluids A*, 1:77–81, 1989. 77

[FN05] I.A. Frigaard and C. Nouar. On the usage of viscosity regularization methods for visco-pastic fluid flow computation. *J. Non-Newtonian Fluid Mech.*, 127:1–26, 2005. 5, 35, 49

[GLT81] R. Glowinski, J.L. Lons, and R. Tremolieres. *Numerical analysis of variational inequalities*, volume 8. North Holland Publishing Company, Amsterdam, 1981. 5

[GP67] R. Glowinski and O. Pironneau. Finite element methods for navier-stokes equations. *Annu. Rev. Fluid Mech.*, 24:1992, 167. 23, 36

[GPT84] D.K. Gartlng and N. Phan-Thien. A numerical solution of a plastic fluid in a parallel-plate plastometer. *J. Non-Newtonian Fluid Mech.*, 15:347–360, 1984. 5

[GTD$^+$97] P.A. Gauglitz, G. Terrones, M.M. Denn, S.J. Muller, and W.R. Rossen. Mechanics of bubbles in sludges and slurries. Proposal for envirnmental management science program project no. 60451, Pacific Nothwest National Laboratory, Richland, WA, 1997. 1, 29, 76

[HHWJ04] M.R. Horsley, R.R. Horsley, K.C. Wilson, and R.L. Jones. Non-Newtonian effects on fall velocities of pair of vertically alligned spheres. *J. Non-Newtonian Fluid Mech.*, 124:147–152, 2004. 31

[HMY69] T. Hirose and M. Moo-Young. Bubble drag and mass transfer in non-Newtonian fluids: creeping flow with power-law fluids. *J Chem Engg Japan*, 47:265, 1969. 72

[HN01] R.R. Huilgol and Q.D. Nguyen. Variational principles and variational inequalities for the unsteady flow of a yield stress. *Int. J. of Non-Linear Mech.*, 36:49, 2001. 6

[HSCC98] M. Hariharaputhiran, R.S. Subramanium, G.A. Campbell, and R.P. Chhabra. The settling of spheres in a viscoplastic fluid. *J. Non-Newtonian Fluid Mech.*, 79:87–97, 1998. 7, 31, 139

[Hui98] R.R. Huilgol. Variational principles and variational inequality for a yield stress fluid in the presence of slip. *J. Non-Newtonian Fluid Mech.*, 75:231, 1998. 6

[Hui02] R.R. Huilgol. Variational inequalities in the flows of yield stress fluids including inertia: Theory and applications. *Phys. Fluids*, 14:1269, 2002. 6

[IRD01] J. Kuchner IV, M.A. Rother, and R.H. Davis. Buoyancy-driven interactions of viscous drops with deforming interfaces. *J. Fluid Mech.*, 446:253–269, 2001. 78

[Jef22] G.B. Jeffery. The rotation of two circular cylinders in a viscous fluid. *Proceeding of Royal Society of London. Series A, Containing papers of a Mathematical and Physical character*, 101(709):169–174, 1922. 33

[JM92] J-T. Jeong and H.K. Moffat. Free surface cusps associated with flow at low Reynolds number. *J. Fluid Mech.*, 241:1–22, 1992. 99

[JM01] L. Jossic and A. Magnin. Drag and stability of objects in a yield stress fluid. *AICHE J.*, 47(12):2666–72, 2001. 31

[JMP02] P. Jay, A. Magnin, and J-M. Piau. Numerical simulation of viscoplastic flows through an axissymmetric contraction. *Journals of Fluid Engineering*, 124:700–705, 2002. 6

[JNRR91] D.D. Joseph, J. Nelson, M. Renardy, and Y. Renardy. Two-dimensional cusped interfaces. *J. Fluid Mech.*, 223:383–409, 1991. 99

[KA95] W. Kob and H.C. Anderson. Testing mode-coupling theory for a supercooled binary Lennard-Jones mixture i: The van Hove correlation function. 51:4626–4641, 1995. 6

[Kal05] D.M. Kalyon. Apparent slip and viscoplasticity of concentrated suspensions. *J. Rheol.*, 49:621–640, 2005. 6, 31

[KHA84] M. Kojima, E.J. Hinch, and A. Acrivos. The formation and expansion of a toroid drop moving in a viscous fluid. *Phys. Fluids*, 27:19–32, 1984. 102

[KL89] C.J. Koh and L.J. Leal. The stability of drop shapes for translation at zero Reynolds number through a quiescent fluid. *Phys. Fluids*, 1:1309–1313, 1989. 102

[KS83] S.F. Kistler and L.E. Scriven. *Computational analysis of polymer processing*, chapter Coating flows, pages 243–299. Applied Science, 1983. 22

[KSBH97] P.C. Kapur, P.J. Scales, D.V. Boger, and T.W. Healy. Yield stress of suspensions loaded with size distributed particles. *AICHE J.*, 43:1171–1179, 1997. 139

[KU] Y. Kawase and J.J. Ulbrecht. The effect of surfactant on terminal velocity of and mass transfer from a fluid sphere in a non-Newtonian fluid. 72

[LD84] G. G. Lipscomb and M. M. Denn. Flow of Bingham fluids in complex geometries. *J. Non-Newtonian Fluid Mech.*, 14:337–346, 1984. 4, 78

[Lea92] L.G. Leal. *Laminar Flow and Convective Transport Processes.* Butterworth-Heinemann Series in Chemical Engineering, 1992. 21, 33, 67, 72

[Lea04] L.G. Leal. Flow induced coalescence of drops in a viscous fluid. *Phys. Fluids*, 16:1833–1851, 2004. 77, 89

[LL86] S.H. Lee and L.G. Leal. Low-Reynolds-number flow past cylindrical bodies of arbitrary cross-sectional shape. *J. Fluid Mech.*, 164:401–427, 1986. 33

[LMD02] B.T. Liu, S.J. Muller, and M.M. Denn. Convergence of a regularization method for creeping flow of a Bingham material about a rigid sphere. *J. Non-Newtonian Fluid Mech.*, 102:179–191, 2002. 31, 56

[LMD03] B.T. Liu, S.J. Muller, and M.M. Denn. Interactions of two rigid spheres translating collinearly in creeping flow in a Bingham material. *J. Non-Newtonian Fluid Mech.*, 113:49–67, 2003. 5, 31, 86

[LR00] J. Li and Y.Y. Renardy. Shear-induced rupturing of a viscous drop in a Bingham liquid. *J. Non-Newtonian Fluid Mech.*, 95:235–251, 2000. 32

[Mar69] G. Marrucci. A theory of coalescence. *Chem. Eng. Sci.*, 24:975, 1969. 89

[Mit04] E. Mitsoulis. On creeping flow of a viscoplastic fluid past a circular cylinder: wall effects. *Chem. Eng. Sci.*, 59:789–800, 2004. 5, 31, 49, 56, 57, 60

[MJM06] O. Merkak, L. Jossic, and A. Magnin. Spheres and interactions between spheres moving at very low velocities in a yield stress fluid. *J. Non-Newtonian Fluid Mech.*, 133:99–108, 2006. 30, 31, 111

[MOS92] W. Mulder, S. Osher, and J.A. Sethian. Computing interfaces in compressible gas dynamics. *J. Comput. Phys.*, 100:209–228, 1992. 22

[MS93] M. Manga and H.A. Stone. Bouyancy-driven interactions between two deformale viscous drops. *J. Fluid Mech.*, 256:647–683, 1993. 78, 89, 117

[MS95] M. Manga and H.A. Stone. Collective hydrodynamics of deformable drops and bubbles in dilute Reynolds number suspensions. *J. Fluid Mech.*, 300:231, 1995. 129

[mum] *Multifrontal Massively Parallel Solver, User Guide.* 19

[OF63] S. Osher and R.P. Fedkiw. Level set methods: An overview and some recent results. *J. Comput. Phys.*, 169:2001, 463. 22

[Old47a] J. Oldroyd. A rational formulation of the equations of plastic flow for a Bingham solid. *Proc. Cambridge Philosophical Soc.*, 43:100–105, 1947. 4

[Old47b] J. Oldroyd. Two dimensional plastic flow of a Bingham solid: A plastic boundary layer theory for slow motion. *Proc. Cambridge Philosophical Soc.*, 43:383–395, 1947. 4

[OS88] S. Osher and J.A. Sethian. Fronts propagating with curvature-dependant speed: Algorithms based on Hamilton-Jacobi formulations. *J. Comput. Phys.*, 83:12, 1988. 22

[OT85] E.J. O'Donovan and R.I. Tanner. Numerical study of the Bingham squeeze film problem. *J. Non-Newtonian Fluid Mech.*, 15:75, 1985. 5

[Poz90] C. Pozrikidis. The instability of a moving viscous drop. *J. Fluid Mech.*, 210:1–21, 1990. 102

[Poz98] C. Pozrikidis. *Numerical Computation in Science and Engineering.* Oxford University Press, New York, 1998. 18, 19

[Pra54] W. Prager. On slow visco-plastic flow. In *Studies in Mathematics and Mechanics.* Academic, New York, 1954. Presented to Richard Von-Mises by Friends, colleagues and pupils. 6

[Pra61] W. Prager. *Introduction to Mechanics of Continua.* Ginn, 1961. 4

[PS01] S.B. Pillaipakkam and P. Singh. A level-set method for computing solutions to viscoelastic two-phase flow. *J. Comput. Phys.*, 174:552–578, 2001. 22, 23, 35

[PSLN06] A. Potapov, R. Spivak, O. M. Lavrenteva, and A. Nir. Motion and deformation of drops in Bingham fluid. *Ind. Eng. Chem. Res.*, 45:6985–6995, 2006. 32, 74, 78, 92

[Red84] J.N. Reddy. *An introduction to the finite element method.* McGraw-Hill, 1984. 10, 14, 15, 19, 35

[Rei60] M. Reiner. *Deformation, strain and flow- An elementary introduction to rheology.* Interscience Publishers, Inc., New York, 1960. 1, 4

[RG94] J.N. Reddy and D.K. Gartling. *The finite element method in heat tranfer and fluid dynamics.* CRC Press, Inc., 1994. 10

[RZD97] M.A. Rother, A.Z. Zinchenko, and R.H. Davis. Buoyancy-driven coalescence of slightly deformable drops. *J. Fluid Mech.*, 346:117, 1997. 77

[SB00] S. Stein and H. Buggisch. Rise of pulsating bubbles in fluids with yield stress. *Z. Angew. Math. Mech.*, 80:827–834, 2000. 32, 74

[Set96] J.A. Sethian. *Level Set Methods.* Cambridge University Press, Cambridge, 1996. 22

[SS03] J.A. Sethian and P. Smereka. Level set methods for fluid interfaces. *Annu. Rev. Fluid Mech.*, 35:347–372, 2003. 22

[SSO94] M. Sussman, P. Smereka, and S. Osher. A level set approach for computing solutions to incompressible two-phase flow. *J. Comput. Phys.*, 114:146–159, 1994. 22, 26, 33, 34

[ST01] D.N. Smyrnaios and J.A. Tsamapoulos. Squueze flow of Bingham plastic. *J. Non-Newtonian Fluid Mech.*, 100:165–190, 2001. 5

[SW95] R.D. Spaans and M.C. Williams. Letter to the editor: At last, a true liquid phase yield stress. *J. Rheol.*, 39:241–426, 1995. 5

[SZ99] R. Scardovelli and S. Zaleski. Direct numerical simulation of free-surface and interfacial flow. *Annu. Rev. Fluid Mech.*, 31:567, 1999. 22

[Tan93] R.I. Tanner. Stokes paradox for power-law fluid around a cylinder. *J. Non-Newtonian Fluid Mech.*, 50:217–224, 1993. 33, 51, 58, 83

[TCdB07] H. Tabuteau, P. Coussot, and J. R. de Bruyn. Drag force on a sphere in steady motion through a yield stress fluid. *J. Rheol.*, 51:125–137, 2007. 30

[TF91] M. Tabata and S. Fujima. An upwind finite element scheme for high Reynolds number flow. *Int. J. Numer. Methods Fluids*, 12:305, 1991. 23, 36

[TMHI90] T. Tsukada, H. Mikami, M. Hozawa, and N. Imaishi. Theoretical and experimental studies of the deformation of bubbles moving in quiescent Newtonian and non-Newtonian liquids. *J Chem Engg Japan*, 23:193–198, 1990. 72

[TTMM02] F. Takemura, S. Takagi, J. Magnaudet, and Y. Matsumoto. Drag and lift forces on a bubble rising near a vertical wall in a viscous liquid. *J. Fluid Mech.*, 461:277–300, 2002. 111

[VBB04] F. Varnik, L. Bocquet, and J.-L. Barrat. A study of static yield stress in a binary Lennard-Jones glass. *J. of Chem Physics*, 120:2788–2801, 2004. 6

[VBBB03] F. Varnik, L. Bocquet, J.-L. Barrat, and L. Berthier. Shear localization in a model glass. *Phys. Rev. Lett.*, 90:095702, 2003. 6

[Wil93] S.D.R. Wilson. Squeezing flow of a Bingham material. *J. Non-Newtonian Fluid Mech.*, 47:211–219, 1993. 5

[YAI71] N. Yoshioka, K. Adachi, and H. Ishimura. On creeping flow of a viscoplastic fluid past a sphere. *Kagaku Kogaku*, 10:1144, 1971. 6, 31

[ZAC96] K.J. Zwick, S.P. Ayyaswami, and I.M. Cohen. Variational analysis of the sqeezing flow of a yield stress fluid. *J. Non-Newtonian Fluid Mech.*, 63:179, 1996. 6

[Zie77] O.C. Zienkiewicz. *The finite element method*. Mc-Graw-Hill, UK, 3 edition, 1977. 9

[ZLAC05] X. Zheng, J. Lowengrub, A. Anderson, and V. Cristini. Adaptive unstructured volume remeshing- ii: Application to two- and three-dimentional level-set simulations of multiphase flow. *J. Comput. Phys.*, 208:626–650, 2005. 89

[ZM02] Th. Zisis and E. Mitsoulis. Viscoplastic flow around a clyinder kept between parallel plates. *J. Non-Newtonian Fluid Mech.*, 105:1–20, 2002. 31